Aus dem Institut für Klinische Radiologie der
Ludwig-Maximilians-Universität München

Direktor: Prof. Dr. med. Dr. h.c. Maximilian Reiser, FACR, FRCR

Optimization and implementation of gold-nanoparticles for medical imaging

Dissertation
zum Erwerb des Doktorgrades der Naturwissenschaften
an der Medizinischen Fakultät
der Ludwig-Maximilians-Universität München

vorgelegt von

Marie Müllner

aus

Dresden

2014

Gedruckt mit Genehmigung der Medizinischen Fakultät der Ludwig-Maximilians-Universität München

Betreuer: Priv.-Doz. Dr. rer. nat. Olaf Dietrich

Zweitgutachter: Prof. Dr. Gunnar Brix

Dekan: Prof. Dr. med. Dr. h.c. Maximilian Reiser, FACR, FRCR

Tag der mündlichen Prüfung: 06.05.2015

Author contact information
Marie Müllner
Helmholtz Zentrum München
German Research Center for Environmental Health
Reseach Unit Medical Radiation Physics and Diagnostics
Ingolstädter Landstraße 1
85764 Neuherberg
Germany
E-mail: marie_muellner@yahoo.de

Contents

List of Figures

List of Tables

List of abbreviations and acronyms

BSA	bovine serum albumin
C	contrast
CNR	contrast-to-noise ratio
CT	computed comography
DEF	dose enhancement factor
DMSO	dimethyl sulfoxide
EGFR	epidermal growth factor
gold-BSA	gold-nanoparticles coated with BSA
gold-cmHsp70.1	gold-nanoparticles conjugated to monoclonal antibody cmHsp70.1
Hsp	heat shock protein
HU	Hounsfield unit
ICP-OES	inductively coupled plasma optical emission spectrometry
PBS	phosphate buffered saline
PCA	principal component analysis
PC	principal component
PE	plating efficiency
PEG	polyethylene glycol
PMMA	polymethyl methacrylate
ROI	region of interest
SDNR	signal-difference-to-noise ratio
SF	survival fraction
SNR	signal-to-noise ratio
TEM	transmission electron microscopy
w%	weight% - mass of gold [g] per mass of tissue [g]×100%

Chapter 1

Introduction

Computed tomography (CT) is a common and widespread diagnostic tool in medical imaging. The benefits are the good availability, a high diagnostic efficiency and the comparatively low costs. But until now molecular imaging cannot be performed with computed tomography. The main reason for this is the lack of targeted and molecularly specific contrast agents [89]. Especially for cancer diagnosis and therapy monitoring, CT is of high importance as it provides valuable anatomical information regarding tumor location, size and spread. Several materials have been suggested as new contrast agents for computed tomography. Materials containing elements such as bismuth [65, 90], lanthanoids [86] and gold with a K-edge at high energies are very promising for improving medical imaging. The advantage of these materials is their high atomic number (high-Z), which leads to a higher contrast at equal mass density. This effect is beneficial, since on the one hand it provides an increased contrast-to-noise ratio at a certain dose or on the other hand the dose can be reduced without detriment for the contrast-to-noise ratio [84].
Newly developed spectral CTs with a photon-counting and energy-selective detector provide the possibility to obtain additional information about an object's absorption properties, the footprint of which can be found in the energy spectrum of the detected photons. These new CT systems are capable of yielding valuable insight into the elemental composition of the tissue and open up the way for new CT contrast agents by detecting element-specific K-edge patterns. In a conventional energy-integrating detector, photons are weighted according to their energy (i.e. low-energy photons are weighted less); for spectral CT, a weighting factor of one is assigned to each photon.
The goal of this thesis is to analyze the potential of gold-nanoparticles as a CT contrast agent to improve medical spectral CT imaging. Challenging questions in medical application of gold-nanoparticles concern the required gold concentration and the specific targeting of malignant tissue.
The presented work is subdivided into three subtasks. For the first subtask, Monte Carlo simulations with the software tool EGSnrc are performed to model medical spectral CT imaging with gold in humans. The simulation results are then analyzed and different

material-decomposition algorithms are applied to enable a specific detection of gold. For the evaluation of the images the signal-to-noise ratio, the contrast-to-noise ratio and the contrast is calculated. The minimum concentration of gold required to provide sufficient contrast in spectral CT *in-vivo* can be estimated with these simulations. In the second subtask, the dose enhancement effect in the vicinity of gold is examined with EGSnrc simulations to better assess potential side effects of gold-nanoparticles. Different X-ray tube voltages and different gold concentrations are implemented to determine the impact on the dose enhancement effect. In the last subtask, cell culture experiments with tumor cells and gold-nanoparticles are performed. The gold-nanoparticles are functionalized with a tumor-specific antibody enabling the realization of targeted nanoparticle-based tumor imaging. The results of the different experiments help to address the question if the designated concentration of gold can be targeted to malignant cells.

This thesis is organized as follows: After the introduction there is a section concerning the theoretical background (Chapter 2), followed by an overview of the methodology and techniques used (Chapter 3). In the results section all outcomes are presented, analyzed and discussed (Chapter 4). The conclusions are drawn in Chapter 5. Applied algorithms and additional investigations are provided in the annex.

Chapter 2

Theoretical background

This chapter summarizes the background and the current state of the art of the main topics covered by this thesis: computed tomography (section 2.1), gold-nanoparticles (section 2.2) and heat shock proteins (section 2.3).

2.1 X-rays and computed tomography

Computed tomography (CT) is an imaging technique, which is based on X-ray attenuation. As opposed to X-ray projection data, CT provides superposition-free tomographic data, generated by rotating the X-ray tube and the detector around the patient. In the following sections, first the X-ray generation (X-ray tube) and detection are described, the interaction of photons with matter and the K-edge effect are summarized, and then the basic principals of CT and the differences between conventional CT and spectral CT are outlined.

2.1.1 X-ray generation and detection

The main parts of an X-ray tube are the cathode (usually made of tungsten), the anode and a glass cylinder with high vacuum. The applied voltage U_a between the heated cathode (to overcome the binding energy of the electrons) and the anode leads to an acceleration of the thermionic emitted electrons towards the anode. The X-ray spectrum (Fig. 2.1) consists of the continuous bremsstrahlung and a superimposed characteristic line spectrum. When the electrons hit the anode they interact with orbital electrons and the atomic nucleus and are decelerated. This deceleration produces electromagnetic waves with a continuous distribution of energies, the continuous bremsstrahlung. The interaction of incoming electrons with inner shell electrons of the anode material lead to the characteristic line spectrum. The characteristic line spectrum is specific for the material of the cathode. The maximum energy of the spectrum is determined by the acceleration voltage U_a and is attained if the entire energy of an electron is transferred to

a single photon $eU_a = E_{\max}$. The anode current specifies the intensity of the spectrum. Only about 1% of the energy is converted to X-rays, the remaining energy generates heat [21].

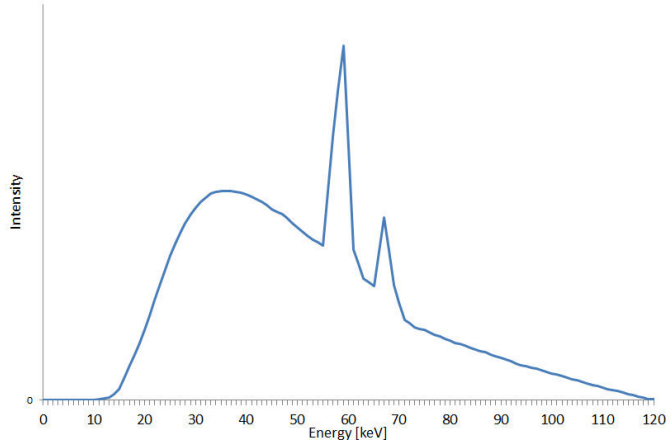

Figure 2.1: Polychromatic X-ray spectrum (tube voltage 120 kV, tungsten anode) distributed over 6 energy bins. This spectrum was obtained with the calculator by the Institute of Physics and Engineering in Medicine (IPEM) [35] and was used for the Monte Carlo simulations.

After penetrating an object, X-rays are not detected directly, but most frequently nowadays by scintillator detectors, consisting of a scintillator medium and a photon detector. Inside the scintillator medium, the impinging photons are converted to light, which is then detected by the photon detector and converted to an electric signal [21]. Such an energy-integrating detector converts the number of incident photons to a single intensity value. This contributes to the problem that CT is not always able to distinguish between different materials. For example, calcified cortical bone and tissue with a high amount of iodine-based contrast agent may have similar attenuation values. A possible solution for this problem would be the use of energy-resolving detectors [9,109], compare section 2.1.4.

2.1.2 Interaction of photons with matter

X-rays have the ability to highly penetrate tissue. While passing through tissue, X-rays undergo an exponential reduction of radiation intensity, i.e., of the number of photons. Absorption and scattering processes are the reason for this attenuation.
The intensity of X-rays $I(s, E)$, with energy E passing a distance s through an object with linear attenuation coefficient $\mu(E, x)$ is given by Lambert-Beer's law

$$I(s, E) = I_0(E) \exp\left(-\int_0^s \mu(E, x)dx\right). \tag{2.1}$$

The space dependence of the linear attenuation coefficient is described by x.

2.1.2.1 Photoelectric effect and Compton scattering

While penetrating matter, photons may interact with the nucleus or the electrons of the material. These interactions with matter either lead to a complete absorption of the photon (its energy is transferred to electrons or positrons) or the photon is scattered and part of its energy is transferred to an electron. These secondary electrons usually have a short path length and deposit their energy in the material.
Several factors influence the attenuation of photons. The atomic number of the element, (or the effective atomic number for chemical compounds), the concentrations of the different components of mixtures and the density have a big influence on the attenuation. For photons with an energy in the diagnostic range, the total linear attenuation comprises mainly two different physical effects, the Compton scattering (photon interacts with a loosely bound electron) and the photoelectric effect (photon interacts with a tightly bound electron) (Figure 2.2). The total linear attenuation can be written as a linear combination of these two effects (Eq. 2.2) [97]

$$\mu_{\text{total}}(E,x) = \mu_{\text{photo}}(E,x) + \mu_{\text{Compton}}(E,x). \tag{2.2}$$

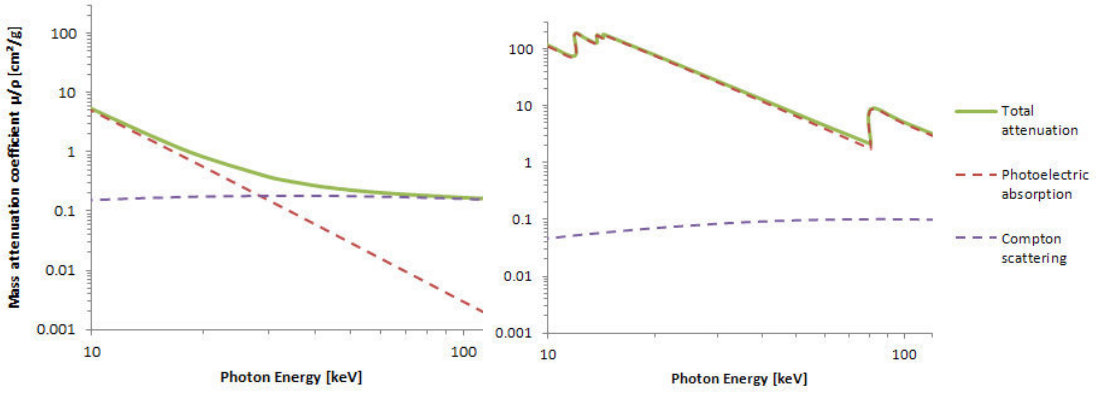

Figure 2.2: Mass attenuation coefficients[2] of liver tissue (left) and pure gold (right). The energy dependent mass attenuation coefficients were calculated with XCOM [55].

The probability of a specific interaction with a single atom is defined by its cross section σ. The linear attenuation coefficient is defined by [21]

$$\begin{aligned} \mu_{\text{total}} &= n\,\sigma_{\text{total}} \\ \sigma_{\text{total}} &= \sigma_{\text{photo}} + \sigma_{\text{Compton}} \end{aligned} \tag{2.3}$$

where n is the number of target atoms per unit volume. The linear attenuation coefficient

[2]The mass attenuation coefficient is defined by μ/ρ, where ρ is the density of the material.

for the photoelectric effect and Compton scattering can be approximated by [7]

$$\mu_{\text{photo}}(E,x) = C_{\text{photo}}(x)\frac{1}{E^3} \tag{2.4}$$

$$\mu_{\text{Compton}}(E,x) = C_{\text{Compton}}(x) f_{\text{KN}}\left(\frac{E}{E_e}\right) \tag{2.5}$$

where $f_{\text{KN}}(E/E_e)$ is the Klein-Nishina-function [66], E_e is the rest mass energy of the electron ($E_e \approx 511\,\text{keV}$) and r_e is the classical electron radius

$$f_{\text{KN}}(\alpha) = 2\pi r_e^2 \frac{1+\alpha}{\alpha^2}\left[\frac{2(1+\alpha)}{1+2\alpha} - \frac{\ln(1+2\alpha)}{\alpha}\right] + \frac{\ln(1+2\alpha)}{2\alpha} - \frac{1+3\alpha}{(1+2\alpha)^2}. \tag{2.6}$$

The position-depending coefficients $C_{\text{photo}}(x)$ and $C_{\text{Compton}}(x)$ are defined as [7]

$$C_{\text{photo}}(x) \propto \rho(x) Z(x)^3 \tag{2.7}$$

$$C_{\text{Compton}}(x) \propto \rho(x) \tag{2.8}$$

with the mass density $\rho(x)$ and the atomic number $Z(x)$. Compton scattering is independent of the atomic number Z, whereas the photoelectric absorption is proportional to Z^3. The mass attenuation coefficient μ/ρ for mixtures and compounds is defined by [3]

$$\left(\frac{\mu(E,x)}{\rho(x)}\right)_{\text{total}} = \sum_i w_i(x)\left(\frac{\mu(E)}{\rho}\right)_i \tag{2.9}$$

w_i denotes the weight fraction and $(\mu(E)/\rho)_i$ is the mass attenuation coefficient of material i. Rearranging this equation and substitution of equation 2.2 yields the following

$$\begin{aligned}
\mu_{\text{total}}(E,x) &= \sum_i \rho_{\text{total}}(x) w_i(x)\left(\frac{\mu(E)}{\rho}\right)_i \\
&= \sum_i \widetilde{w}_i(x)\left(\frac{\mu(E)}{\rho}\right)_i \\
&= \sum_i \widetilde{w}_i(x)\left(\frac{\mu_{\text{photo}}(E) + \mu_{\text{Compton}}(E)}{\rho}\right)_i \\
\text{with } \widetilde{w}_i(x) &= \rho_{\text{total}}(x) w_i(x)
\end{aligned} \tag{2.10}$$

Since the energy dependence of either the photoelectric absorption or the Compton scattering is the same for all elements of a mixture or compound, Eq. 2.10 remains valid independent of the elemental composition as long as no absorption edges occur. For CT examinations where elements (contrast agents) with a high atomic number (and absorption edges) are present, Eq. 2.10 needs to be modified [97, 100].

2.1.2.2 K-edge effect

For materials with a high atomic number, K-edge discontinuities of the mass attenuation coefficient have a big influence on the attenuation. The K-edge effect describes a sudden increase of the attenuation coefficient (Figure 2.3), if the photon energy is equal or just above the binding energy of the K-shell electrons. The energy at which the K-edge effect occurs, is specific for each material and can be used to identify and quantify high-atomic-number contrast agents in a tissue. To use the K-edge discontinuity for medical imaging, one needs to be aware of photon starvation as a result of beam hardening in the low-energy part of the X-ray spectrum, which can result in the imperceptibility of the K-edge effect [21].

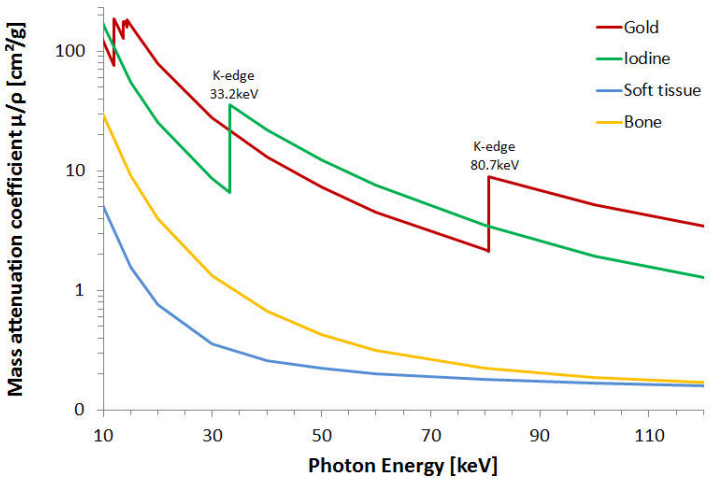

Figure 2.3: Mass attenuation coefficients of gold, iodine, bone and soft tissue. The energy dependent mass attenuation coefficients were calculated with XCOM [55].

2.1.3 Computed tomography

Computed tomography was developed during the 1960s and 1970s by Sir Godfrey Hounsfield, who received the Nobel Prize in Medicine for his invention.
CT imaging is an X-ray technology, where the X-ray tube and the detector rotate around the patient. The measured attenuation values from one angular position define one projection. The scan data of all projections form the raw data set, which is also called a sinogram. The raw data set represents the Radon transformation of the scanned object structure. To reconstruct cross-sectional images, the inverse Radon transformation needs to be calculated, which can be done, e.g. with a filtered back projection or other more elaborate reconstruction techniques. The reconstructed CT images provide the spatial distribution of the linear attenuation coefficients μ. For medical imaging (e.g. mammography, projection radiography, CT) the X-ray tube voltage is typically in the range of 25 to 150 kV. The main advantage of CT images as compared to other imaging techniques

is the high spatial and temporal resolution. In contrast to conventional X-ray projection images, reconstructed CT images provide sectional views, which are free from superimposition [21].
The linear attenuation values μ in each voxel of the reconstructed CT image are converted to Hounsfield Units (HU), to obtain values which are approximately independent of the used spectrum, [21]

$$\mathrm{HU} = \frac{\mu - \mu_{\mathrm{water}}}{\mu_{\mathrm{water}}} 1000. \tag{2.11}$$

The HU value of water is equal to 0 and air has the HU value of -1000. The Hounsfield scale used in medical imaging ranges from -1024 to +3071, but the human visual system cannot distinguish between 4096 gray values. To overcome this visualization problem, a process called "windowing" is applied. Voxels with values below a certain threshold are displayed as black and voxel values above another threshold are displayed as white. Voxel values within this window are then mapped to appropriate gray-scale intervals [21].

2.1.4 Conventional CT and spectral CT

A disadvantage of conventional CT systems is that the commonly used energy-integrating detectors do not provide any information about the polychromatic energy spectrum of the detected photons. This disadvantage can be potentially overcome by newly developed so-called spectral CT systems (e.g. by Philips Healthcare Deutschland GmbH, Hamburg[3], Fig. 2.4). This new CT system has a photon-counting and energy-selective detector. In a conventional energy-integrating detector, photons are weighted according to their energy (therefore low-energy photons are weighted less). In contrast to conventional CT, a photon-counting detector assigns a weighting factor equal to one to all incoming photons. Energy-depending weighting schemes can be applied to increase the contrast (and/or the contrast-to-noise ratio). This could be especially interesting for soft tissue contrast, which is higher for low-energy photons. Furthermore, the energy spectrum of the X-ray tube can be divided into sub-energy-ranges, so-called energy bins. An energy-selective detector provides the possibility to assign the incoming photons, depending on their energy, to different energy bins. The energy-selective detector developed by Philips has 6 energy bins with freely selectable energy thresholds. This new detector technology provides the possibility to differentiate between tissues based on their different energy-depending attenuations and is by this capable of yielding valuable insight into the elemental composition of the tissue. A further potential of spectral CT devices is the possibility to detect element-specific K-edge patters, opening up the way for new high-atomic number CT contrast agents. The system is able to detect K-edge patterns of several high-atomic-number contrast agents enabling the simultaneous use of more than one contrast agent [40]. It can furthermore reduce the X-ray radiation dose, as no contrast free reference examination is necessary,

[3]Philips medical systems is involved in the m^4 cluster, in which framework this study was conducted.

since virtual non-contrast images can be calculated based on the information in the different energy bins. This information can also be used for a better material characterization, which is particularly useful for kidney stone differentiation, lesion and plaque characterization. Furthermore cupping artifacts can be reduced. Cupping artifacts, also called beam-hardening artifacts, are a result of the non-linear relation between projection data and the attenuation coefficients. While passing through tissue, photons with low energy are strongly attenuated in contrast to photons with higher energy. The polychromatic X-ray beam thus becomes harder[4] while passing through tissue [21]. Furthermore, electronic noise can be reduced and even molecular imaging might be possible with spectral CT [40, 68, 101, 109].

The small-animal spectral CT by Philips Healthcare has a single-line, energy-sensitive detector (Gamma Medica-Ideas, Northridge, CA, USA) with a 3-mm-thick cadmium telluride sensor. This photon-counting detector is able to separate the incoming photons according to their energy into six energy-bins. The energy thresholds between the individual bins can be freely set. The field-of-view is 6 to 23 cm and the spatial resolution is 100 to 250 µm. The voltage of the X-ray tube is 40 to 130 kV and the rotation speed is 1/3 s [78].

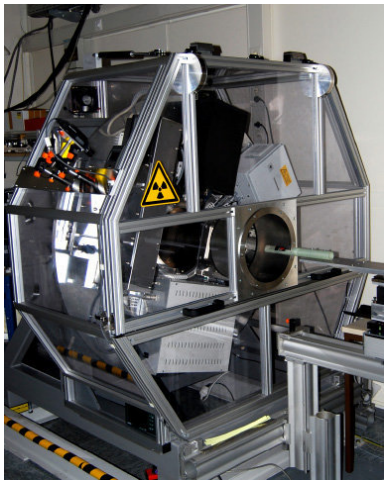

Figure 2.4: Philips prototype small-animal spectral CT [109].

The formula describing the intensity of X-rays after penetrating an object (Eq. 2.1) can be modified, to obtain the integrated intensity in bin i of a spectral CT:

$$I_i(s) = \int_{E_{i-1}}^{E_i} I_{i0} \exp\left(-\int_0^s \mu(E,x)dx\right) dE \quad \text{for} \quad i = 1, ..., K \tag{2.12}$$

$$I_{i0} = \int_{E_{i-1}}^{E_i} I_0(E)dE$$

[4] Beam hardening describes the removal of low-energy photons from the X-ray beam and by this increases the average energy of the beam.

where K is the number of energy bins. E_i are the energy-thresholds of the bins and I_{i0} is the polychromatic X-ray photon fluence in bin i.
Eq. 2.12 can be rewritten

$$\ln\left(\frac{I_{i0}}{I_i(s)}\right) = \int_{E_{i-1}}^{E_i}\int_0^s \mu(E,x)dxdE. \tag{2.13}$$

The main drawback of a photon-counting detector is the long scanning time, which makes it impossible to use this new technique for clinical applications at the moment. Furthermore, the Philips Healthcare prototype can only be used for small animals and phantoms [109]. The long scanning time is due to the reduction of the CT rotation speed and the X-ray tube current, which is necessary to ensure a low count rate and a short dead time. The high count rates are especially a problem for the unattenuated primary beam (beam which does not penetrate tissue); filters could be used to eliminate that problem. Smaller detector pixels could help to overcome the high count rates, but Compton-crosstalk, K-escape radiation and charge sharing effects need to be considered [97]; in addition the noise in each energy bin is increased, as a consequence of the decreased number of photons per bin [46].

2.2 Gold-nanoparticles

Nanotechnology opens up a wide field for scientific research. It is therefore not surprising, that there has been a continuously rapid growth in nano-science during the last years. Nano-technology is used in many different research areas and relies on the interaction of several scientific fields, including chemistry, biology, physics, informatics and medicine.

2.2.1 Nanoparticles in medicine

In medicine, nanoparticles have found numerous applications including drug delivery, therapy and diagnostics. Nanoparticles are very promising in *in-vivo* cancer imaging and therapy. They can be used as minimal-invasive diagnostic tools and at the same time as drug delivery systems. Functional groups, such as antibodies, imaging labels and therapeutic drugs, can be conjugated to nanoparticles. This multifunctional characteristic of nanoparticles provides the possibility to combine targeted-therapy and molecular imaging, also called theranostics (*thera*py+diag*nostics*). Nano-technology is a promising approach for personalized oncology [13, 22, 48]. However, a number of conditions for applying nanoparticles as diagnostic and therapeutic tools must be taken into consideration. Particular attention is given to the short and long term toxicity, the biodistribution, the nonspecific uptake, routes of elimination, routes of delivery and bioavailability of the nanoparticles [48]. It is important to realize that the properties of nanoparticles often differ substantially from the properties of macro materials. Since nanoparticles are much

smaller than human cells, they can interact with biomolecules on the surface and inside the cell [22]. Taking all that into consideration, nanoparticles for the intravascular application should have the following properties: The nanoparticles should be easily dispersable and stable. Nanoparticles should have a long circulation time, which implies no uptake by the reticuloendothelial system. Nevertheless; there should be programmed clearance mechanisms, which guarantee a safe excretion. They should have a high sensitivity and specificity for the target, and hardly any unspecific binding should occur [48].

2.2.2 Gold-nanoparticles: Physical properties, uptake and toxicology

A specific class of nanoparticles with potential applications in medicine are gold-nanoparticles. Considering their relatively simple synthesis with defined size, shape and surface chemical compositions, make gold-nanoparticles attractive candidates for medical application. Furthermore, they can be easily coupled with biological targeting molecules (e.g. tumor-specific antibodies), enabling targeted tumor imaging.
Gold-nanoparticles appear red, blue, green or brown depending on their size and shape. Interactions of conduction band electrons with the incident light lead to these different colors, this effect is called localized surface plasmon resonance [91]. The diameter of gold-nanoparticles is typically in the range of 2 to 100 nm [22]. To enhance the (tumor) targeting efficacy gold-nanoparticles can be functionalized with different chemical compounds such as bovine serum albumin (BSA) [27], PEG[5] [31, 70, 119], high-density lipoprotein (HDL) [34], anti-EGFR[6] antibody [93], trastuzumab[7] [23, 50], 2-deoxy-D-glucose [12, 72], gadolinium chelate [6], ^{18}FDG-anti-MTDH[8] [116] and radioactive iodine-labeled, cyclic RGD-PEG[9] [64].
One common method to synthesize gold-nanoparticles is described by Turkevich [115] and Frens [41]. For this method, chloroauric acid ($HAuCl_4$) solution is brought to boil, sodium citrate solution ($Na_3C_6H_5O_7$) is added and then gold-nanoparticles will form. Sodium citrate ions serve as reducing agent and as coating and stabilizing agent of the gold-nanoparticles. The citrate anions attach to the gold-nanoparticle surface leading to an electrostatic repulsion and by this prevent agglomeration of the gold-nanoparticles. The diameter of gold-nanoparticles can be adjusted by changing the citrate/gold ratio.
The mechanism of gold-nanoparticle uptake and cytotoxic effects depend on various factors, such as surface properties (e.g. charge), coating or functionalization, shape, size, concentration and incubation time [4, 25, 29, 63, 122]. The physiochemical properties of functionalized and coated gold-nanoparticles correspond to the properties of the adsorbed protein layer [122]. This protein layer can reduce the internalization of gold-nanoparticles

[5] polyethylene glycol
[6] epidermal growth factor receptor
[7] Her2 specific monoclonal antibody, trade name Herceptin
[8] [^{18}F]2-fluoro-2-deoxy-D-glucose and anti-metadherin antibody
[9] RGD-arginine-glycine-aspartic acid

by immune cells, which would lead to a rapid clearance of the gold-nanoparticles from the bloodstream. The uptake mechanism of gold-nanoparticles has not been fully explained yet. Direct penetration, receptor-mediated endocytosis and macropinocytosis are possible uptake mechanisms leading to gold-nanoparticles, that are localized in the cell in vesicles or vacuoles [4, 26, 63, 122].
Several studies investigated the toxic effects of gold-nanoparticles *in vitro* and *in vivo*. The applied amounts of gold-nanoparticles, the size and coating/functionalization of gold-nanoparticles differed a lot. Hainfeld et al. [51] estimate the median lethal dose (LD50) at 3.2 mg gold/g (for 1.9 nm gold-nanoparticles). Khlebtsov et al. [63] specified a concentration limit of 10^{12} gold-nanoparticles/ml (approximately 0.02 mg/g (0.002w%)) for gold-nanoparticles with a diameter of 10 nm, below that, no cytotoxic effects should occur.
Several studies with 50 nm gold-nanoparticles indicated no toxic effects [24, 26][10]. They had a smaller organ distribution than smaller gold-nanoparticles [36].
For this thesis, gold-nanoparticles with a diameter of 50 nm and 15 nm were chosen.

2.2.3 Gold-nanoparticles as CT contrast agents

The application of contrast agents in medical imaging is a common procedure to improve the contrast and highlight different structures in the body. Nowadays iodine-based materials are the only contrast agents, which are clinically used for intravascular contrast-enhanced computed tomography[11]. Iodine-based contrast agents are generally well tolerated [118]. A benefit of iodine-based contrast agents is their high solubility in water and their relatively high mass attenuation coefficient [84]. The main drawback of iodine is its short blood half-life, which is less than 10 minutes [48]. Furthermore, side effects, such as thyroid or renal dysfunction or anaphylactoid symptoms, may occur. Literature data concerning side effects vary from 1:10000 to 1:100000 [118]. Unfortunately, conjugates of iodine and targeting moieties or antibodies has failed to deliver detectable concentrations to the desired location, preventing its use for molecular imaging [51]. To overcome these problems, gold-nanoparticles have been suggested as new contrast agents for computed tomography. A new contrast agent should fulfill the following requirements [18]:

1) The contrast agent leads to an increase in the localized signal.

2) Little or no undesirable side effects to the patient occur.

3) It leads to a high specific uptake by the targeted tissue and

4) a low background uptake.

[10] The applied gold-nanoparticle concentration was not specified in [26]. Mice were injected with 8 mg gold-nanoparticles per kg body weight per week (approximately 8×10^{-4}w%) in [24].
[11] Another commonly applied X-ray contrast agent is barium sulfate, which is only used for the alimentary tract.

To item 1) several groups have shown that gold-nanoparticles are a promising new CT contrast agent. The localized signal was over 5-times higher, compared to the tissue without gold-nanoparticles [89, 93]. It was also shown that coated/functionalized gold-nanoparticles enable longer imaging times [51]. Another beneficial aspect is the possibility to detect small tumors with a diameter of 0.4-1 cm, which could lead to better prognoses [50, 51, 93]. It was furthermore shown that the contrast enhancement is independent of size and shape of the nanoparticles. Only the concentration of the gold in the tissue affects the attenuation of the X-rays [57].
To item 2) gold-nanoparticles have shown to be nontoxic in the concentration applied here.
To items 3) and 4) a high specific uptake of gold-nanoparticles can be achieved by functionalization of the gold-nanoparticles with specific antibodies, such as 2-deoxy-D-glucose labeled gold-nanoparticles [12, 72], by trastuzumab (Her2 specific monoclonal antibody, trade name Herceptin) labeled gold-nanoparticles [50], high-density lipoprotein (HDL) gold-nanoparticles [34] and by anti-EGFR antibody labeled gold-nanoparticles [93].
Several investigations with conventional CT, dual-energy CT and spectral CT were already performed with gold-based contrast agents. Hainfeld et al. [51] were one of the first using gold-nanoparticles as contrast agent. X-ray imaging of mice was performed 2 minutes after intravenous injection of 0.2 ml gold-nanoparticle solution (concentration 270 mg/ml). The amount of gold in the tumor was determined by graphite furnace atomic absorption spectrometry. 15 minutes after injection the tumor contained 2.268 mg/g gold (4.3% of the injected dose, approximately 0.23w%[12]). However, the gold concentration rapidly decreased in the first hour. In the X-ray image, the blood vessels could be clearly distinguished due to the higher absorption of gold and the increased vascularity in the tumor. One should remember that for the precise identification of gold-based contrast agent in a conventional CT an additional contrast-free scan is required, which increases the X-ray dose applied to the patient.
In 2011 Hainfeld published new results with gold as micro-CT contrast agent in mice [50]. The gold-nanoparticles (15 nm) were conjugated to trastuzumab. The tumors showed a mean uptake of 8.3% of the injected dose (conversion into w% yields 0.05w% up to 0.18w% for the applied doses). On the micro-CT images, the tumors were identifiable by their radiodense peripheries. Boote et al. [18] investigated gold-nanoparticles as a CT contrast agent in juvenile swine. The results are not clearcut. They stated that a few hundred µg gold per g wet tissue were sufficient to achieve a good contrast, but in the presented figures and tables higher values are given. For example, it was stated that the gold amount in the liver was 380 µg/g, but own recalculations of the amount of gold in the liver with the values given in Table 1 result in 3.94 mg/g. The presented results should therefore be interpreted with caution.
Ducote et al. [38] and Clark et al. [96] used gold for dual-energy CT imaging. To obtain

[12]The term w% stands for weight% and means mass of gold [g] per mass of tissue [g]×100%.

a SNR of 5 in the projection data of the dual-energy CT, the required amount of gold was determined to be 58.5 mg gold per ml (approximately 5.85w%) [38]. For the measurements done by Roessl et al. [96], similar gold concentrations (0.2 mol/L and 0.25 mol/L, approximately 4 to 5w% gold) were used; this amount of gold was clearly recognizable in the dual-energy CT. Another investigation in dual-energy micro-CT showed that the detectability limit of gold ranged from 4 mg/ml down to 1 mg/ml (approximately 0.4 down to 0.1w%) for different filter algorithms. The phantom had a diameter of 3 cm. The detectability limit of gold in an *in-vivo* mouse experiment was 1.5 mg/ml (approximately 0.15w%) [33].
As described in section 2.1.4 the K-edge discontinuity of high-atomic number materials can be used to improve medical imaging. However, photon starvation in the low-energy part of the X-ray spectrum, can lead to the imperceptibility of the K-edge effect. Considering this, gold would be better suited for K-edge imaging than iodine, as the K-edge of iodine is in the low-energy part of the X-ray spectrum (33.2 keV), while the K-edge of gold is at 80.7 keV, which lies well inside the X-ray energy spectrum relevant for medical imaging and is only little influenced by photon starvation.
Several factors should be taken into consideration for the application of gold-nanoparticles K-edge imaging. The capability to detect K-edge patterns depends strongly on the concentration of gold in tissue. As the gold concentration decreases, the step size of the K-edge gets smaller (Figure 2.5).

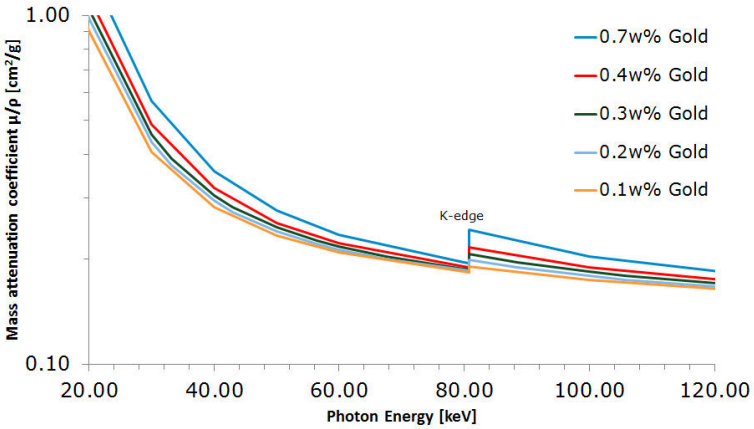

Figure 2.5: Impact of the concentration of gold in liver tissue on the size of the K-edge. The energy dependent mass attenuation coefficients were calculated with XCOM [55].

In case of an energy-selective detector, the bin thresholds have also a significant impact on the ability to detect K-edge patterns. To use the K-edge discontinuity in the average mass attenuation curve, the average mass attenuation coefficient in the bin below the K-edge needs to be smaller than the average mass attenuation coefficient in the bin above the K-edge. In Figure 2.6, the average mass attenuation coefficient in the bin below the K-edge

of gold (A) is higher than the mass attenuation coefficient in the bin above the K-edge (B). Reducing the bin size of the bin below the K-edge can overcome this problem. As already mentioned above, one also needs to take into account that the number of photons per bin decreases with decreasing bin size, inducing higher noise in that bin.

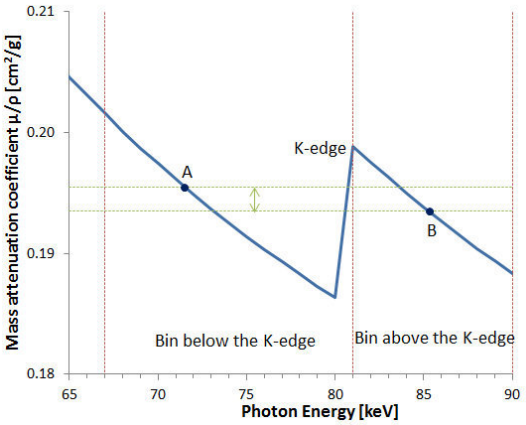

Figure 2.6: Mass attenuation curve for 0.2w% gold in liver tissue (blue curve). The dashed red lines mark the bin thresholds for the bin below and above the K-edge of gold. The points A and B mark the energy, where the attenuation is equal to the average attenuation in the two bins. The energy dependent mass attenuation coefficients were calculated with XCOM [55].

As the tissue concentration of gold decreases, the bin size, for which the above mentioned criteria holds, becomes smaller. Figure 2.7 shows the possible bin sizes below and above the K-edge with respect to the concentration of gold in the tissue. The mass attenuation coefficient below the K-edge of gold is smaller than the coefficient above the K-edge only in the uncolored region, i.e. above the shown surface. The purpose of this figure is to illustrate that the possible bin sizes rapidly decrease with a decreasing gold concentration.

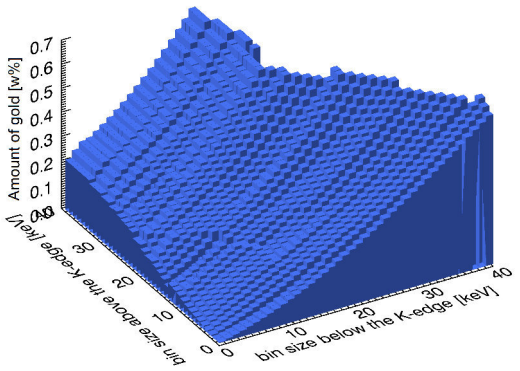

Figure 2.7: Relationship between gold concentration and bin size. The energy-dependent mass attenuation coefficients for different gold concentrations and different bin sizes were calculated with XCOM [55], without taking account of image noise.

Several examinations were performed with spectral-CT and gold as a contrast agent [15,47, 105]. Cormode et al. [34] performed spectral CT measurements in combination with gold-HDL nanoparticles enabling a specific targeting of atherosclerosis. In a concentration series with gold-HDL (concentrations from 0 to 100 mM, i.e., approximately 0.39 to 1.97w%), iodine and calcium phosphate powder, the gold containing regions in the phantom could be clearly identified. They furthermore performed *in-vivo* mouse experiments. Mice were injected with 500 mg gold per kg body weight. Gold-HDL accumulated in atherosclerotic plaques and could be clearly detected in the images.

2.2.4 Dose enhancement in the presence of gold

Ionizing radiation is attenuated while traveling through tissue and radiation energy is absorbed by the tissue. The dose enhancement effect of gold (or other high-atomic-number materials) is a purely physical effect, which depends on the concentration of gold and the photon energy, i.e. the used X-ray spectrum. A substance which leads to a localized dose enhancement is called a radiosensitizer. The dose enhancement factor can be defined as the ratio of absorbed dose in the tissue with a radiosensitizer divided by the absorbed dose without this radiosensitizer. The absorbed dose in the tissue is defined as the absorbed energy divided by the mass of the absorbing material.
The basic principle, which leads to the dose enhancement effect of gold is the higher mass attenuation coefficient/cross section compared to biological tissues. This effect leads to an increased absorption followed by secondary electron production when the incoming photons interact with gold-nanoparticles. These secondary electrons can reach the DNA and lead to single and double strand breaks. The radiolysis of the cellular water produces hydrogen radicals and hydroxyl radicals. These radicals can further interact with biological molecules and are responsible for the indirect ionization effects [71, 123]. The produced secondary electrons have a short penetration range in tissue (e.g. 2.711 µm for 50 kV [71]). As a result of this short penetration range, the dose enhancement effect strongly depends on the location of gold-nanoparticles in the cell. Possible side effects on healthy cells when using gold-nanoparticles as X-ray contrast agent should therefore be examined.
The dose enhancing effect of high-atomic-number materials has been known for many years. Matsudaira et al. showed the dose enhancement effect of iodine already in 1980 [76]. The idea to use gold as radiosensitizer was proposed by Regulla et al. [92]. The predicted dose enhancement factor close to a gold foil ranged from 55 (120 kV) up to 114 (60 kV). The influence of different beam energies, the concentration of gold and the size of gold-nanoparticles on the dose enhancement effect has been investigated with different Monte Carlo simulations [30, 37, 59, 69–71, 75, 77, 114]. *In-vivo* and *in-vitro* experiments have also been carried out [23, 29, 49, 52, 70]. The simulations and the *in-vivo* and *in-vitro* studies showed that beam energies in the keV range lead to a higher dose enhancement than MeV beam energies [29, 30, 59, 69, 71, 77]. The reason for this seems to be the decreased

interaction probability of high energy photons with the gold-nanoparticles. The size of the gold-nanoparticles has a minor influence on the dose enhancement. The self-absorbed energy by the gold-nanoparticles is very small compared to the deposited total energy. The crucial parameter is the amount of gold inside the cells [29, 69, 71].
The dose enhancement effect in the environment of a single gold-nanoparticle was also investigated with Monte Carlo simulations [59, 71]. Simulations with NOREC[13] demonstrated a microscopic dose enhancement factor for a 50 kV spectrum of approximately 130 at 0.1 µm away from a gold-nanoparticle and approximately 14 at 10 µm away from a gold-nanoparticle. For distances larger than 13 µm, the dose enhancement effect vanished (this corresponds to the maximum range of secondary electrons) [59]. Leung et al. [71] performed GEANT4[14] simulations. They simulated single gold-nanoparticles with a diameter of 2, 50 and 100 nm. The results demonstrated an interaction enhancement ratio[15] up to 2000 for a 50 kV beam. The observed maximum range of the secondary electrons was 13 µm for the 50 kV spectrum (independent of the nanoparticle size). For 50 nm gold-nanoparticles and the 50 kV spectrum the mean effective range of the electrons was 2.711±0.003 µm.
Further simulations were performed with tissue mixtures containing a specific gold amount instead of single gold-nanoparticles. The results of these simulations are summarized in Table 2.1.

Table 2.1: Summary of dose enhancement factors (DEF) in the literature.

Simulation code	spectrum	DEF	gold amount	Reference
DOSXYZnrc	140 kV	2.114	7 mg/g (≈ 0.7w%)	[30]
DOSXYZnrc	140 kV	3.811	18 mg/g (≈ 1.8w%)	[30]
DOSXYZnrc	140 kV	5.601	30 mg/g (≈ 3w%)	[30]
GEANT4	150 kV	1.7	10 mg/g (≈ 1w%)	[77]
Penelope	600 kV	1.304	5 mg/g (≈ 0.5w%)	[75]
Penelope	600 kV	1.597	10 mg/g (≈ 1w%)	[75]

Calculations based on Penelope simulations[16] (with a 300 kV source) predicted that the required amount of gold for doubling the prescribed dose is 15.4 up to 20.2 mg gold per gram (approximately 1.5 up to 2.0w%) [69]. Detappe et al. [37] and Berbeco et al. [16] performed analytical calculations to investigate the dose enhancement factor of gold in blood vessels with a 6 MV spectrum and 30 mg gold per ml (approximately 3w%). The predicted dose enhancement factors were 2.1 and 1.7.
Alqathami et al. [5] developed a novel multicompartment phantom radiochromic radia-

[13] Monte Carlo code for simulating electron tracks in liquid water.
[14] Monte Carlo simulation package to simulate the passage of particles through matter
[15] The interaction enhancement ratio is calculated by taking the ratio of the total number of produced secondary electrons within the gold-nanoparticle and within water [71].
[16] Monte Carlo simulation of electron and photon transport.

tion dosimeter. The phantom contained a small compartment with a concentration of 0.5 mM (approximately 0.01w%) gold-nanoparticles (diameter 50 nm). The obtained dose enhancement factors were 1.77 for a 100 kV spectrum and 1.11 for a 6 MV spectrum.
Chithrani et al. [29] showed that gold-nanoparticles with a size of 50 nm provided the highest dose enhancement compared to other sizes; this effect is due to the higher uptake of these gold-nanoparticles into the cell.

2.3 Heat shock proteins

After introducing the physical aspects of CT and gold-nanoparticles as possible agents for imaging and therapy, the next sections will concentrate on possibilities of a specific binding of the gold-nanoparticles to the target cells. For this thesis, Hsp70 in combination with the monoclonal antibody cmHsp70.1 is of special interest as it might serve as a tumor-specific target and ligand, that can be used for the functionalization of gold-nanoparticles. Thus, the following section will give a short overview on heat shock proteins.
In 1962 the young scientist Ferruccio Ritossa described the puffing of the chromosomes[17] of Drosophila after heat exposure. A prominent journal editor initially rejected this discovery, because "it was irrelevant to the scientific community". The products of the genes, associated with the puffing of the chromosomes, were called heat shock proteins, as they were produced after heat exposure [94]. It was shown later that many different chemical and physical cellular stress factors, like virus transformation, hypoxia and arsenite lead to an increased synthesis of Hsps, for this reason heat shock proteins are also called stress proteins [81]. Hsps seem to be present in every organism (plants, animals, archaebacteria, eubacteria) [73]. They form a large group of physiologically essential, phylogenetically conserved proteins, which can be divided into discrete families according to their molecular weight: Hsp100, Hsp90, Hsp70, Hsp60 and small Hsps (also called Hsp20) [80, 102]. Hsps perform several functions in the body. They play a pivotal role as molecular chaperones[18], and are important in cancer and virus immunogenicity [53, 111], apoptosis [102], stimulation of macrophages [14], antigen processing and presentation [103, 117].

2.3.1 Localization of heat shock proteins in-vivo

Hsps are classically found intracellular, where they perform their pivotal role as intracellular chaperones and prevent unfolded proteins from aggregation during cellular differentiation. Transport of proteins across membranes, protein repair and protein degradation are further functions of Hsps. In order to protect cells from lethal damage, the synthesis of Hsps is increased in normal and in tumor cells after environmental stress [73]. Welch et

[17] Puffing of chromosomes describes specific gene activity.
[18] Chaperones are proteins. They play a key roll in the folding or assembly of newly synthesized proteins. After this process is finished the chaperones do not occur in these structures anymore and are available for folding or assembly processes of other proteins.

al. [120] discovered that Hsps are located in the cytoplasm, Golgi apparatus, endoplasmic reticulum, nuclei or the nucleoli.
Hsps can also be present in the extracellular milieu, where they are important for the stimulation of the immune system. They especially affect the activity of natural killer cells [19, 42]. It was shown that Hsps in the serum are associated with stress conditions, such as inflammation, bacterial and viral infections and oncological diseases [80]. The transport mechanisms to the plasma membrane, the membrane anchorage, and the export of the Hsps are not fully identified. Increased amounts of Hsp70 and Hsp90 in the serum of cancer patients and in the medium of tumor cell lines, might be due to tumor necrosis and apoptosis, but also an active release from viable tumor cells is possible [80]. Asea et al. [11] could demonstrate that extracellular Hsps act as cytokines, influencing human monocytes, which leads to a pro-inflammatory immune response.
The transport of the Hsps to the cell membrane and the membrane anchorage is not completely clear yet. It is assumed that viable tumor cells secret the extracellular Hsps by an active release. The Hsps on the cell membrane are also very important for the stimulation of the immune system [80]. Hsps on the cell membrane might bind peptides, which could lead to an immune response [53].

2.3.2 Heat shock protein 70 and the monoclonal antibody cmHsp70.1

Heat shock protein 70 (Hsp70)[19] is the major stress-inducible member of the Hsp family. As already described above, the function of Hsp70 depends on its localization. Intracellular Hsp70 mainly performs chaperone functions. In tumors, the basal Hsp70 level is increased and will be further increased after environmental stress such as nutrient deficiency, hypoxia, heavy metals, irradiation, and/or chemotherapeutic agents [82]. In cancer cells, Hsp70 can lead to a suppression of various anticancer mechanisms and to tumor rejection by the immune system [103]. On the other hand, extracellular Hsp70 can bind to antigen-presenting cells (monocytes/macrophages, dendritic cells). This leads to a non-specific stimulation of the innate immune system, initiated by secretion of pro-inflammatory cytokines (e.g. IL-1β, IL-6, TNF-α) [11].
The membrane-bound Hsp70 seems to be highly tumor-specific, making it a promising target structure for cancer therapeutics, diagnostic and/or prognostic markers [44, 103]. The work of Gehrmann et al. [43] indicates that membrane-bound Hsp70 acts as a protector against radiation/chemotherapy-induced apoptosis and as a target structure for natural killer cell-mediated cytolysis. It is not clear yet, what causes the difference of the Hsp70 expression on the cell membrane of normal and tumor cells. Gehrmann et al. [44] assumed that differences in the composition of the membrane lipids are a causative factor. Investigations lead to the presumption that the expression of Hsp70 on the membrane of tumor

[19] Old nomenclatures for Hsp70 are Hsp72, Hsp70i, Hsp70-1 and HspA. In order to resolve this multiple designations a new nomenclature for the Hsps was introduced, according to this the new term for Hsp70 is HspA1A [61]. Still the old nomenclature is most common and will therefore be used for this thesis.

cells is a negative prognostic marker for the overall survival of tumor patients [85, 110]. These results make Hsp70 a very promising target for cancer therapy.

Several groups have investigated the occurrence of Hsp70 on the membrane of tumor cells. Ferrarini et al. [39] was one of the first, who described the occurrence of Hsp70 on the plasma membrane of the GLC1 cell line (microcitoma). It was shown that Hsp70 is expressed on the cell membrane of HTLV-I infected rabbit cell lines [32], various sarcoma cells and larynx carcinoma cells [81]. Furthermore, Hsp70 is expressed on the cell membrane of colorectal, gastric, lung, neuronal, pancreas carcinomas, liver metastases (primary tumor: colorectal cancer) and leukemic blasts (cells generated from tumor biopsy material) [53,85]. Multhoff et al. [80] screened more than 1000 different tumor biopsies (lung, colon, gastric, pancreatic, mammary cancer), blasts of hematological diseases (acute myeloid leukemia, acute lymphoblastic leukemia, chronic myeloid leukemia, chronic lymphoid leukemia) and the corresponding healthy tissues for the surface expression of Hsp70. None of the normal tissues expressed Hsp70 on the membrane surface, but 50 to 70% of the tumor tissue were Hsp70 membrane positive.

Antibodies are proteins, which can detect and bind to a specific target (a so-called antigen). For this thesis, the monoclonal antibody cmHsp70.1 was used. It was shown that this antibody conjugates to the tumor-specific membrane-bound Hsp70. Other commercially available mouse anti-Hsp70 antibodies fail to conjugate to the membrane-bound Hsp70 of viable tumor cells [82]. Stangl et al. [108] demonstrated the internalization of the monoclonal antibody cmHsp70.1 into tumor cells.

Chapter 3

Methods

3.1 Spectral CT imaging with gold-nanoparticles - Monte Carlo simulations

To investigate the effect of gold as a new CT contrast agent, Monte Carlo simulations with EGSnrc were performed [62]. EGS is an abbreviation for Electron-Gamma-Shower. The code is owned by the National Research Council (nrc) of Canada. EGSnrc is free of charge for research and other non-commercial purposes.
EGSnrc simulates the coupled transport of electrons and photons with energies ranging from 1 keV to 10 GeV. Transport of charged particles is simulated with the condensed history technique. Cross sections for the photoelectric effect, Rayleigh scattering and pair production are in agreement with the XCOM/NIST database. For the imaging simulations, the cutoff energy for photons was 1 keV and for electrons 60 keV. The particle's energy is locally deposited, if it is below the cutoff energy. For a detailed description of EGSnrc the reader is referred to [62].
EGSnrc has a flexible user-interface, in which the geometry of the X-ray detector and the source is specified. A few changes in these subroutines, written by Helmut Schlattl, were necessary for the simulation of the spectral CT (i.e. the photon-counting detector). The changes are described in detail in the following sections.

3.1.1 Phantom setup, simulations and general evaluation

3.1.1.1 Phantom setup

Simple voxel phantom
As part of this dissertation, a simple cylindrical voxel phantom was implemented. The purpose of this voxel phantom was to determine the minimum gold concentration required to provide sufficient contrast in spectral CT *in-vivo* and to investigate the influence of different sizes of regions of interest (ROI).
The diameter of the phantom was 30 cm and each voxel had a size of $1.765 \times 1.765 \times 4.84\,\mathrm{mm}^3$.

The voxel phantom consisted of simulated liver parenchyma ($\rho = 1.06\,\mathrm{g/cm^3}$) and five sets of 4 ROIs, referred to as metastases. The metastases had a size of $1.4{\times}1.4\,\mathrm{cm^2}$, $1.05{\times}1.05\,\mathrm{cm^2}$, $0.7{\times}0.7\,\mathrm{cm^2}$ and $0.35{\times}0.35\,\mathrm{cm^2}$. It was assumed that the elemental composition of the metastases is the same as the liver parenchyma, but the density was decreased to $\rho = 1.02\,\mathrm{g/cm^3}$, since metastases are usually visible as hypodense lesions in CT. For each set of 4 ROIs, a different concentration of gold was added to the metastases. The gold-nanoparticles were not explicitly modeled in these simulations, instead a homogeneous distribution of gold in the tissue was implemented. This approach can be justified with the assumption of a rather homogeneous distribution of the gold-nanoparticles and the detector resolution. The elemental composition and the densities are summarized in Table 3.1 and the voxel phantom is shown in Figure 3.1(a).

Table 3.1: Chemical composition of different tissues.

	Liver [56]	Metastasis with and without gold					
		0w%	0.7w%	0.4w%	0.3w%	0.2w%	0.1w%
$\rho\ [\frac{\mathrm{g}}{\mathrm{cm^3}}]$	1.06	1.02	1.154	1.0931	1.0748	1.0566	1.0383
H [w%]	10.2	10.2	10.13	10.16	10.17	10.18	10.19
C [w%]	13.9	13.9	13.80	13.84	13.86	13.87	13.89
N [w%]	3.0	3.0	2.98	2.99	2.99	2.99	3.00
O [w%]	71.6	71.6	71.10	71.31	71.39	71.46	71.53
Na [w%]	0.2	0.2	0.2	0.2	0.2	0.2	0.2
P [w%]	0.3	0.3	0.3	0.3	0.3	0.3	0.3
S [w%]	0.3	0.3	0.3	0.3	0.3	0.3	0.3
Cl [w%]	0.2	0.2	0.2	0.2	0.2	0.2	0.2
K [w%]	0.3	0.3	0.3	0.3	0.3	0.3	0.3
Au [w%]	0	0	0.7	0.4	0.3	0.2	0.1

Human voxel phantom

The human voxel phantom was based on CT data of a real female [112]. The dimensions of one voxel were $1.765{\times}1.765{\times}4.84\,\mathrm{mm^3}$. The size of the whole phantom was 244 voxels (430.66 mm) in x-direction, 142 voxels (250.63 mm) in y-direction and 346 voxels (1674.64 mm) in z-direction. The chemical composition of the organs was based on the ICRU report 44 [17].

To investigate the effect of gold as a contrast agent in small tumors or metastases in the liver, three ROIs with a size of $1.24{\times}1.24\,\mathrm{cm^2}$, $0.88{\times}0.88\,\mathrm{cm^2}$ and $0.35{\times}0.35\,\mathrm{cm^2}$ were implemented in the voxel phantom as part of this thesis. The CT slice which was used for the simulations is shown in Figure 3.1(b). The elemental composition and the densities of the ROIs were the same as in (Table 3.1).

The applied dose was estimated for the human voxel phantom. The variable *EDEP* in EGSnrc provides the deposited energy during a particular step and can be summed up to get the total deposited energy. The simulations here are only performed for one slice.

The slice thickness at the detector is 1.6 mm, giving a slice thickness of 0.877 mm at the isocenter. The scan length for a liver-spleen scan is assumed to be 18.4 cm. The total number of rotations for that scan length is 210 (scan length divided by slice thickness at the isocenter). The mass of the whole phantom is 58.92 kg. The whole body dose[20] can then be calculated as the product of the deposited energy in one slice and the number of rotations divided by the mass of the whole phantom. This result is then multiplied with a weighting factor to get the effective dose. The weighting factor for this scan is approximately 1.865 (Helmut Schlattl, private communication).

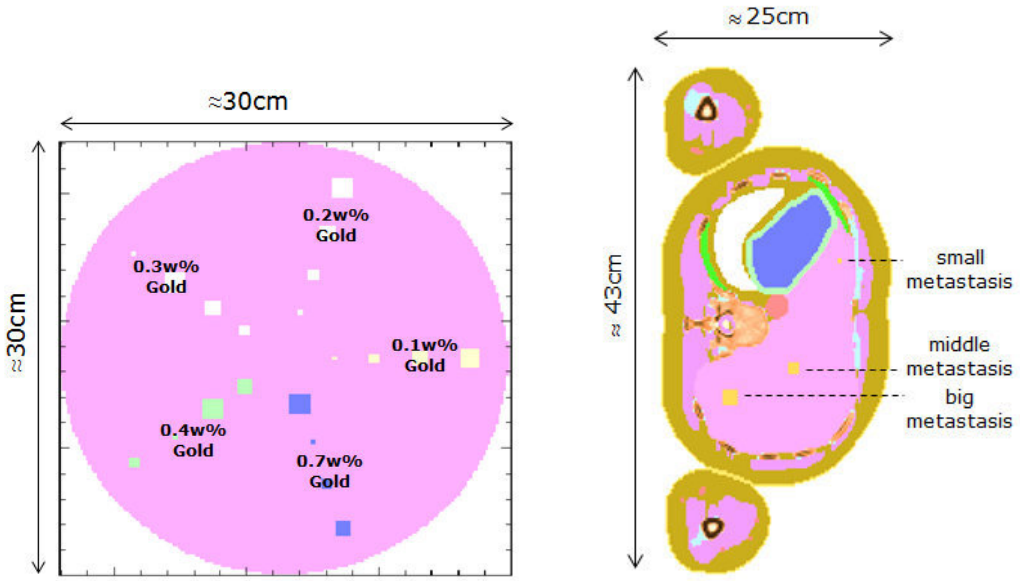

(a) Simple voxel phantom used for the Monte Carlo simulations.

(b) Slice of the human voxel phantom used for the Monte Carlo simulations (slice number 250, height from the ground 1.21 m).

Figure 3.1: The two voxel phantoms used for the Monte Carlo simulations.

3.1.1.2 Simulation setup

All simulations were performed on a high performance computing - high availability - cluster (IBM x3950 X5, 2×Intel Xeon 8C X7560 130W 2.26GHz/24MB, 32GB RAM).

Detector

For the simulations an ideal photon-counting detector was implemented, i.e. all incident photons were detected, the count rate was unlimited and the energy resolution was perfect. Scattered photons were stored in a separate array and were not used for the evaluation, i.e.

[20]The whole body dose is defined as the fraction of the total amount of ionizing radiation absorbed by the body and the body's mass.

the raw data sets did not contain signals from scattered photons. The original detector implementation was modified, by adding a further array dimension (with size 97), which is used to store the number of incoming photons depending on their energy. Each element of the new array dimension stores the number of photons with energies in the interval [x keV,(x+1) keV) ($x \in 25, 26, ..., 120$), referred to as 1-keV-bins. All incoming photons with an energy below 25 keV were stored in one element of the array [0 keV,25 keV).
For all the simulations, the focus-detector distance (FDD) in the simulations was 104 cm and the focus-object distance (FOD) was 57 cm. 1160 views were performed and the number of histories per view was 10^9. For the simple voxel phantom, the detector had 580 detector elements, each with a size of 1.5 mm. For the human voxel phantom, the detector had 640 detector elements, each with a size of 1.6 mm. The slice thickness was 1.6 mm.

Spectrum
The spectrum used for the imaging simulations had a peak energy of 120 keV and a mean energy of 64.5 keV. X-rays were filtered with 1.2 mm titanium and 1.5 mm aluminum. The anode material was tungsten. To calculate the spectrum, the calculator by the Institute of Physics and Engineering in Medicine (IPEM) [35] was used. The spectrum is shown in Figure 2.1.

CT image reconstruction and filtering
All CT images were reconstructed with the OPED algorithm (orthogonal polynomial expansion on disc) [121]. Each pixel in the reconstructed images had a size of $0.84 \times 0.84\,\text{mm}^2$ and the reconstruction size was 512×512 pixel. If explicitly stated a bilateral filter algorithm [113] was used to filter the reconstructed images. Bilateral filtering merges range and domain filtering. Both filters calculate weighted averaged image values. The range filter applies weights, that decrease with decreasing similarity of the regarded image values. Domain filtering uses weights, that decline with increasing distance. The CT image reconstruction and the image processing algorithms were performed on an Intel 64-bit, 3.2GHz, Core 2 Duo cluster.

3.1.1.3 Image analysis and image quality quantities

CT image quality deals with two different approaches, the spatial resolution also called high-contrast resolution and the contrast detectability also called low-contrast resolution. Spatial resolution can be defined as the capability to resolve small items, which are very close together. The modulation transfer function (MTF) is the common method to characterize the spatial resolution. Many factors in the image acquisition process can impair the spatial resolution, e.g. the focal spot size, image reconstruction, detector characteristics [98].
The contrast detectability is of major interest for this thesis. Contrast detectability de-

fines the capability of a system to discriminate items with similar densities. Three factors mainly influence the detectability of an object with respect to its size. The first one is the level of contrast, i.e. the difference in density between the object and the background. Image noise is the second factor and the third factor is the window setting, which is applied to display the image [98].
To judge and compare the quality of the reconstructed and processed images, the signal-to-noise ratio (SNR), the contrast-to-noise ratio (CNR) and the contrast (C) were calculated in the image domain. These quality measurements give an indication which image processing algorithm described below is most suitable for the detection of gold. One should keep in mind that the objects shape, size and sharpness of edges do not affect these quality measurements. The perceptibility of objects in different images can differ despite of similar quality measurements.
The mean energy $\overline{E_i}$ of bin i was approximated by

$$\overline{E_i} = \frac{\int_{E_i} E N_0(E) dE}{\int_{E_i} N_0(E) dE} \tag{3.1}$$

where N_0 is the photon fluence in photons/keV for the X-ray spectrum described above. These values were used as input information for XCOM [55], to calculate the energy dependent average mass attenuation coefficients for each bin. The weight percentage of all elemental components is shown in Table 3.1. The mean energy and the average mass attenuation coefficients for each bin are required input parameters for some of the material-decomposition algorithms.
For the simple voxel phantom only the biggest metastases for each gold concentration were selected as ROIs, each ROI had a size of 20×20 pixels. The ROIs for the human voxel phantom consisted of all three metastases. The three ROIs had sizes of 11×11, 7×7 and 4×4 pixels. To be able to compare all results, the images were normalized to $[0, 1]$ before the evaluation. The SNR, CNR and the contrast were calculated for each individual ROI and then the mean was calculated. The ROIs and the corresponding background regions are shown in Figure 3.2.
The signal-to-noise ratio is defined as the ratio of the mean value in the region of interest $\overline{\mu}_{\mathrm{ROI}}$ and the standard deviation $\sqrt{\sigma^2_{\mathrm{ROI}}}$ [104]

$$\mathrm{SNR} = \frac{\overline{\mu}_{\mathrm{ROI}}}{\sqrt{\sigma^2_{\mathrm{ROI}}}}. \tag{3.2}$$

The SNR does not give any information about the perceptibility of an object. This is represented by the contrast-to-noise ratio (CNR), which takes into account the signal and noise features of the reconstructed images.
The CNR is defined as the attenuation difference between the ROI $\overline{\mu}_{\mathrm{ROI}}$ and the back-

ground $\overline{\mu}_{\mathrm{B}}$ divided by the noise, [104].

$$\mathrm{CNR} = \frac{|\overline{\mu}_{\mathrm{ROI}} - \overline{\mu}_{\mathrm{B}}|}{\sqrt{\sigma^2_{\mathrm{ROI}} + \sigma^2_{\mathrm{B}}}} \tag{3.3}$$

where σ^2_{ROI}, σ^2_{B} are the variances respectively.
The effective CNR ($\mathrm{CNR}_{\mathrm{eff}}$) is defined as the CNR multiplied by the square root of the number of pixels (N) in the ROI. According to the Rose criterion [79] the effective CNR in CT images should be greater than 5 to be able to differentiate between the background and the metastases.

$$\mathrm{CNR}_{\mathrm{eff}} = \sqrt{N}\mathrm{CNR} \tag{3.4}$$

The contrast (C) is defined as [105]

$$\mathrm{C} = \frac{|\overline{\mu}_{\mathrm{ROI}} - \overline{\mu}_{\mathrm{B}}|}{\overline{\mu}_{\mathrm{ROI}} + \overline{\mu}_{\mathrm{B}}}. \tag{3.5}$$

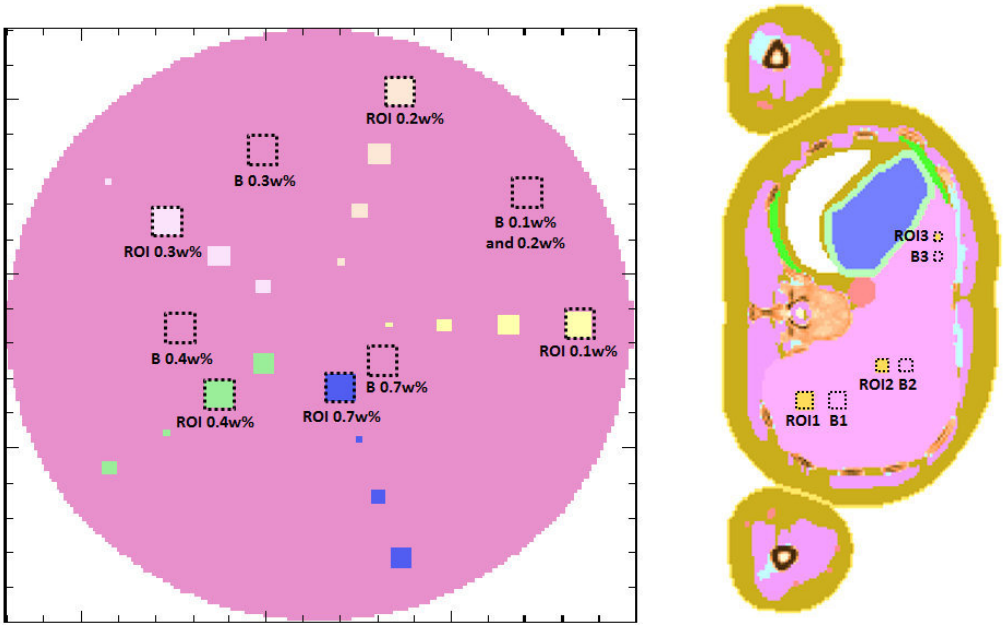

Figure 3.2: ROIs for the two voxel phantoms and the corresponding background (B) regions. In the simple voxel phantom for the ROI with 0.2w% and 0.1w% gold the same background region is used.

3.1.2 Energy-integrating and Photon-counting detectors

For the first examinations, a photon-counting and an energy-integrating detector (conventional X-ray detector) without energy resolution were simulated and the reconstructed images were compared. Photon-counting detectors weight all impinging photons with

a weighting factor equal to one, whereas energy-integrating detectors apply an energy-depending weighting factor to the each photon. The used weighting function was $1/E^3$, as this weighting function provides the highest signal-to-noise ratio [45]. The photon-counting and energy-integrating detectors were calculated as

$$\text{photon-counting} = \sum_{E=25\,\text{keV}}^{119\,\text{keV}} \text{1-keV-bin}_E \tag{3.6}$$

$$\text{energy-integrating} = \frac{\text{1-keV-bin}_{25\,\text{keV}}}{(23.3\,\text{keV})^3} \sum_{E=26\,\text{keV}}^{119\,\text{keV}} \frac{\text{1-keV-bin}_E}{E^3} \quad . \tag{3.7}$$

The 1-keV-bin$_E$ is the array, which contains the number of photons with energies in the interval $[E,E + 1\,\text{keV})$. All photons with an energy in the range of $[0\,\text{keV},25\,\text{keV})$ were stored in one bin, the mean energy of this bin was 23.3 keV.
Photon-counting detectors have advantages over energy-integrating detectors, e.g. rejection of electronics noise, low noise imaging and smaller cupping artifacts [106].
The cupping artifacts in the reconstructed images were quantified by the the image value at the edge and the center of the phantom.

$$\text{cupping} = \frac{\mu_{\text{edge}} - \mu_{\text{center}}}{\mu_{\text{edge}}} \cdot 100\% \tag{3.8}$$

The results are furthermore used as comparison to the performance of the energy-resolved photon-counting detector.

3.1.3 Optimization of detector bin thresholds

Roessl et al. [95] have shown that for optimal material detection one bin threshold should be at the K-edge of the high-Z material. The bins just below this threshold and just above this threshold are very important for the efficient detection of the high-Z material. As described before the incoming photons were stored in 1-keV-bins corresponding to the photon energy. To show the effect of different bin sizes above and below the K-edge of gold (80.7 keV), the 1-keV-bins were summed up and the CT images were then reconstructed with OPED. The bins above the K-edge ranged from [81,82) keV up to [81,120] keV and the bins below the K-edge ranged from [80,81) up to [40,81) in steps of 1 keV. The reconstructed images were then analyzed with the assessment criteria described above.

The SDNR criterion

To investigate the optimal width of the two energy bins just below and above the K-edge of gold, the signal-difference-to-noise ratio (SDNR) criterion was used [54].

$$\text{SDNR} = \frac{\overline{\mu}_{\text{CTabove}} - \overline{\mu}_{\text{CTbelow}}}{\sqrt{\sigma^2_{\text{CTabove}} + \sigma^2_{\text{CTbelow}}}} \tag{3.9}$$

with $\overline{\mu}_{\text{CTabove}}$ and $\overline{\mu}_{\text{CTbelow}}$ being the linear attenuation coefficients in the ROIs in the reconstructed CT images in the bin above and below the K-edge and $\sigma^2_{\text{CTabove}}$ and $\sigma^2_{\text{CTbelow}}$ describe the corresponding variance. In order to use the sudden increase in the linear attenuation coefficient of gold[21], Eq. 3.9 needs to be maximized under the constraint

$$\overline{\mu}_{\text{XCOMabove}} > \overline{\mu}_{\text{XCOMbelow}} \tag{3.10}$$

$\overline{\mu}_{\text{XCOMabove}}$ and $\overline{\mu}_{\text{XCOMbelow}}$ are the theoretical linear attenuation coefficients in the bin below and above the K-edge of gold calculated with XCOM. This constraint ensures that the theoretical linear attenuation coefficient in the bin below the K-edge of gold is bigger than in the bin above the K-edge of gold.

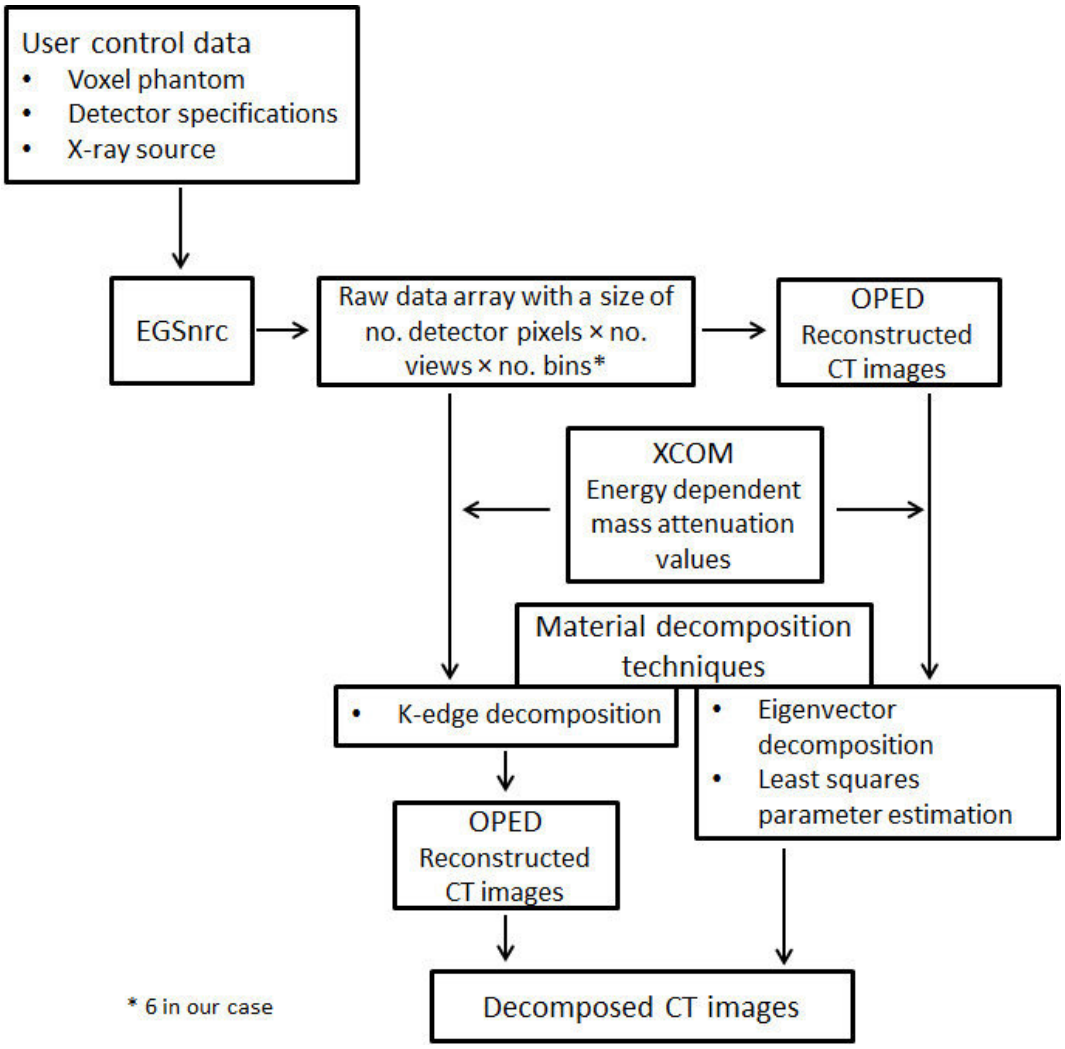

Figure 3.3: Structure of the performed steps and the used additional information.

[21] This sudden increase, inside the relevant diagnostic energy range, is unique for high-Z materials and does not occur in biological tissues.

3.1.4 Material-decomposition techniques

In the following sections the implemented material-decomposition techniques will be described. The main aim of all these algorithms is to enhance the images and improve the detectability and ideally the quantification of gold by a human observer.
The evaluated algorithms are an eigenvector decomposition, the K-edge decomposition and a least-squares parameter estimation. Only the K-edge decomposition algorithm is applied to the raw data sets, all other techniques utilize the reconstructed CT images. All algorithms are applied to the bin data pixel by pixel, i.e. are working on a vector of length K (K - number of energy bins).
The sequence of the steps is illustrated in Fig. 3.3.

3.1.4.1 Eigenvector decomposition

The idea for the eigenvector decomposition algorithm for energy resolved CT images is based on the principal component analysis (PCA) (also known as Karhunen-Loéve theorem). PCA is a method in multivariate statistical analysis. The basic principle of the method is the transformation of the multivariate data set with respect to the covariance matrix [58]. The main purpose of this algorithm is the noise reduction in the reconstructed energy dependent images. The algorithm is applied along the energy axis and not in the spatial dimensions, therefore no loss in spatial resolution or blurring occurs. A similar approach was introduced by Gonzales and Lalush [46, 47].
The X-ray projection data of the $K = 6$ energy bins were reconstructed with OPED. For the eigenvector decomposition, the reconstructed images and the mass attenuation ($\mu(E)/\rho$) values in each energy bin of M known materials are required. The mass attenuation values were calculated for each bin with XCOM [55] and are summarized in Table 3.2.
Each energy dependent linear attenuation vector $\mu(E,x) \in \mathbb{R}^K$ can be described with a basis $V = [v_1, ..., v_K] \in \mathbb{R}^{K\times K}$ (all basis vectors $v_i \in \mathbb{R}^K$ are linearly independent) and $z(x) \in \mathbb{R}^K$

$$\mu(E,x) = \sum_{i=1}^{K} v_i z_i(x) = V z(x) \qquad . \tag{3.11}$$

x describes the spatial dependence. This linear attenuation vector $\mu(E,x)$ can now be approximated by using a subset of the basis vectors v_i with $i = 1, ..., K'$ and $K' < K$

$$\widetilde{\mu}(E,x) = \sum_{i=1}^{K'} v_i z_i(x) = \widetilde{V}\widetilde{z}(x) \qquad . \tag{3.12}$$

According to the principal component analysis the error $\mu(E,x) - \widetilde{\mu}(E,x)$ is minimal, if the basis V consists of the eigenvectors of the covariance (or correlation) matrix of $\mu(E,x)$ [58]. The primary idea of the algorithm is now to implement the covariance matrix based on

the mass-attenuation curves of the P known materials instead of estimating it from the reconstructed images. It is assumed that the attenuation curve at each pixel contains a mixture of these basis functions (Equation 2.9). For this thesis the mass-attenuation curves of gold, hard bone mixture, and liver tissue were used (Table 3.2),

$$\begin{aligned} \mu(E,x) &= \sum_{i=1}^{P} \rho_{\text{total}}(x) w_i(x) \left(\frac{\mu(E)}{\rho}\right)_i = \rho_{\text{total}}(x) M w(x) \\ \text{Cov}(\mu(E,x)) &= M \text{Cov}(\rho_{\text{total}}(x) w(x)) M^T \end{aligned} \tag{3.13}$$

with $M \in \mathbb{R}^{K \times P}$ being the matrix containing the mass-attenuation curves of the P known materials and M^T is the transposed matrix.

Table 3.2: Mass attenuation vectors used as input for the eigenvector decomposition.

	Bin 1	Bin 2	Bin 3	Bin 4	Bin 5	Bin 6
	non-optimized bin thresholds					
mean Energy [keV]	30.9	43.3	63.2	84.8	98.5	113.0
$(\mu/\rho)_{\text{gold}}$ [cm^2/g]	25.470	10.490	3.9630	7.8490	5.3600	3.7850
$(\mu/\rho)_{\text{bone}}$ [cm^2/g]	0.9313	0.5245	0.3256	0.2573	0.1994	0.1766
$(\mu/\rho)_{\text{liver}}$ [cm^2/g]	0.3302	0.2526	0.2112	0.1944	0.1762	0.1664
	optimized bin thresholds					
mean Energy [keV]	39.9	54.1	66.5	77.5	83.0	97.1
$(\mu/\rho)_{\text{gold}}$ [cm^2/g]	13.070	5.9140	3.4790	2.3650	8.2920	5.5590
$(\mu/\rho)_{\text{bone}}$ [cm^2/g]	0.6125	0.3479	0.2623	0.2232	0.2100	0.1865
$(\mu/\rho)_{\text{liver}}$ [cm^2/g]	0.2698	0.2162	0.1957	0.1844	0.1800	0.1709

For this thesis the following estimation of the covariance matrix $\text{Cov}(\rho_{\text{total}}(x)w(x))$ was used

$$= \text{Cov} \begin{pmatrix} \overbrace{\begin{matrix} 0.0032 \\ \cdots \\ 1.0716 \end{matrix}}^{n_1} & \overbrace{\begin{matrix} 0.0 \\ \cdots \\ 0.0 \end{matrix}}^{n_2} & \overbrace{\begin{matrix} 0.0 \\ \cdots \\ 1.06 \end{matrix}}^{n_3} & \overbrace{\begin{matrix} 0.0 \\ \cdots \\ 0.0 \end{matrix}}^{n_4} \\ \cdots & \cdots & \cdots & \cdots \end{pmatrix} \tag{3.14}$$

$$= \begin{pmatrix} 2.29 \times 10^{-6} & -2.45 \times 10^{-6} & 5.30 \times 10^{-6} \\ -2.45 \times 10^{-6} & 0.49 & -0.11 \\ 5.30 \times 10^{-6} & -0.11 & 0.24 \end{pmatrix} = \text{Cov}(\rho_{\text{total}}(x)w(x)) \tag{3.15}$$

To obtain this covariance matrix the number of pixels containing gold ($n_1 = 582$), bone ($n_2 = 50190$), the remaining pixels in the phantom ($n_3 = 79792$) and air ($n_4 = 131580$) were approximated. The columns in the matrix 3.14 are the product of the total density multiplied by the weight fraction. For the first n_1 columns this is equal to $1.0748 \cdot$

$[0.003, 0.0, 0.997]$ (i.e. 0.3w% gold and 99.7w% liver tissue). For the next n_2 columns it is equal to $1.782 \cdot [0.0, 1.0, 0.0]$, for the next n_3 columns it is equal to $1.06 \cdot [0.0, 0.0, 1.0]$ and for the last n_4 columns refer to the pixels containing only air and therefore $w(x) = [0.0, 0.0, 0.0]$.
According to the principal component analysis the covariance matrix in Equation 3.13 can be written as

$$M\mathrm{Cov}(\rho_{\mathrm{total}}(x)w(x))M^T = V\Lambda V^T \tag{3.16}$$

V contains the orthonormal eigenvectors of the covariance matrix and Λ the corresponding eigenvalues. The eigenvalues and the corresponding eigenvectors are arranged in decreasing order (with respect to the absolute value of the eigenvalues). So the first eigenvector is related to the direction with maximal variance and the last eigenvector to the direction with minimal variance. As already described above the linear attenuation vector $\mu(E, x)$ can now be estimated by using only a subset of the eigenvectors (Equation 3.12). With equation 3.11 and 3.12 it follows, that the noise suppressed images $\widetilde{\mu}(E, x)$ can be obtained as follows

$$\begin{aligned} z(x) &= V^T\mu(E,x) \\ \widetilde{z}(x) &= \widetilde{V}^T\mu(E,x) \\ \widetilde{\mu}(E,x) &= \widetilde{V}\widetilde{V}^T\mu(E,x) \quad . \end{aligned} \tag{3.17}$$

With some further transformations, the concentration $\widetilde{w}(x) = \rho_{\mathrm{total}}(x)w(x) \in \mathbb{R}^3$ of gold, bone and liver (multiplied by the total density) can be calculated. The total density can be approximated as $\rho_{\mathrm{total}}(x) = \sum_{i=1}^{3} \widetilde{w}_i(x)$.

$$\begin{aligned} \overbrace{\widetilde{\mu}(E,x)}^{6\times1} &= \overbrace{\widetilde{V}}^{6\times3}\ \overbrace{\widetilde{V}^T}^{3\times6}\ \overbrace{\mu(E,x)}^{6\times1} \stackrel{!}{=} \rho_{\mathrm{total}}(x)\overbrace{M}^{6\times3}\overbrace{w(x)}^{3\times1} \\ \widetilde{V}^T\widetilde{\mu}(E,x) &= \widetilde{V}^T\mu(E,x) = \rho_{\mathrm{total}}(x)\widetilde{V}^T M w(x) \\ (\widetilde{V}^T M)^{-1}\widetilde{V}^T\widetilde{\mu}(E,x) &= (\widetilde{V}^T M)^{-1}\widetilde{V}^T\mu(E,x) = \rho_{\mathrm{total}}(x)w(x) \end{aligned} \tag{3.18}$$

The matrix $\widetilde{V}^T M$ is invertible. With the eigenvector decomposition also so called basis images $B(x) \in \mathbb{R}^K$ can be calculated as the scalar product

$$B(x) = V^T\mu(E,x) \tag{3.19}$$

The first basis image contains the information due to the maximal variance, the second basis image the information due to the second highest variance and so on. PCA is often used to reduce dimensionality, without a serious information loss. The first basis image should therefore be similar to a CT image of a conventional CT detector (i.e. without energy resolution). The basis images are shown in the annex.

3.1.4.2 K-edge decomposition algorithm

One of the first approaches to use the spectral information was the K-edge decomposition technique, also called K-edge imaging, which was first described in 1976 by Alvarez and Macovski [7, 74]. This method uses the energy-dependent attenuation information in each energy bin to convert it into two components, the photoelectric effect and the Compton scattering. The basic idea of the algorithm is described below.
The raw data sets from each energy bin are used as input data for the algorithm and the algorithm is applied to each pixel.
For CT examinations where elements (contrast agents) with a high-atomic-number are present, a modification of Eq. 2.2 is necessary [97, 100]. According to Equation 2.10 the total attenuation of a mixture can be presented as a sum of the individual elements. Instead of using all individual elements, the total attenuation can be split up into the low-atomic-number elements (i.e. the biological tissues) and the high-atomic-number element. For the low-atomic-number elements Eq. 2.10 holds, yielding the following equation:

$$\begin{aligned}
\mu_{\text{total}}(E,x) &= \widetilde{w}_{\text{lowZ}}(x)\left(\frac{\mu(E,x)}{\rho(x)}\right)_{\text{lowZ}} + \widetilde{w}_{\text{highZ}}(x)\left(\frac{\mu(E,x)}{\rho(x)}\right)_{\text{highZ}} \\
\mu_{\text{total}}(E,x) &= \widetilde{w}_{\text{lowZ}}(x)\left(\frac{\mu_{\text{photo}}(E,x)+\mu_{\text{Compton}}(E,x)}{\rho(x)}\right)_{\text{lowZ}} \\
&\quad + \widetilde{w}_{\text{highZ}}(x)\left(\frac{\mu(E,x)}{\rho(x)}\right)_{\text{highZ}}
\end{aligned} \tag{3.20}$$

Substituting Eqs. 2.4 and 2.5 into 3.20 leads to [22]

$$\mu(E,x) = \widetilde{C}_{\text{photo}}(x)\frac{1}{E^3} + \widetilde{C}_{\text{Compton}}(x) f_{\text{KN}}\left(\frac{E}{E_e}\right) + \widetilde{w}_{\text{highZ}}(x)\left(\frac{\mu(E)}{\rho}\right)_{\text{highZ}}. \tag{3.21}$$

with

$$\widetilde{C}_{\text{photo}}(x) = \left(\frac{\widetilde{w}(x)}{\rho(x)}\right)_{\text{lowZ}} C_{\text{photo}}(x) = \rho_{\text{total}}\left(\frac{w(x)}{\rho(x)}\right)_{\text{lowZ}} C_{\text{photo}}(x) \tag{3.22}$$

$$\widetilde{C}_{\text{Compton}}(x) = \left(\frac{\widetilde{w}(x)}{\rho(x)}\right)_{\text{lowZ}} 2\pi r_e^2 C_{\text{Compton}}(x) = \rho_{\text{total}}\left(\frac{w(x)}{\rho(x)}\right)_{\text{lowZ}} 2\pi r_e^2 C_{\text{Compton}}(x) \tag{3.23}$$

In order to increase numerical stability the factor $2\pi r_e^2$ was eliminated from f_{KN}. $1/E^3$, $f_{\text{KN}}(E/E_e)$ and $(\mu(E)/\rho)_{\text{highZ}}$ should be linearly independent (i.e. form a basis in $\mathbb{R}^K$), in order to provide a clear separation of the three effects. The linear independence of these three vectors can be easily checked (e.g. with Wolfram Mathematica). It might be beneficial to multiply each vector with a constant factor to increase the numerical tolerance.

[22] The constant term $2\pi r_e^2$ in the Klein-Nishina-function f_{KN} (Equation 2.6) is shifted to $\widetilde{C}_{\text{Compton}}(x)$.

Integrating Eq. 3.21 leads to

$$\begin{aligned}\int_0^s \mu(E,x)dx &= \int_0^s \widetilde{C}_{\text{photo}}(x)\frac{1}{E^3} + \widetilde{C}_{\text{Compton}}(x) f_{\text{KN}}\left(\frac{E}{E_e}\right) + \rho_{\text{highZ}}(x)\left(\frac{\mu(E)}{\rho}\right)_{\text{highZ}} dx \\ &= A_{\text{photo}}\frac{1}{E^3} + A_{\text{Compton}} f_{\text{KN}}\left(\frac{E}{E_e}\right) + A_{\text{highZ}} f_{\text{highZ}}(E) \qquad (3.24)\end{aligned}$$

with

$$\begin{aligned}A_{\text{photo}} &= \int_0^s \widetilde{C}_{\text{photo}}(x)dx \\ A_{\text{Compton}} &= \int_0^s \widetilde{C}_{\text{Compton}}(x)dx \\ A_{\text{highZ}} &= \int_0^s \widetilde{w}_{\text{highZ}}(x)dx = \delta_{\text{highZ}}\end{aligned}$$

$f_{\text{highZ}}(E)$ is the mass attenuation coefficient, which includes Compton scattering, the photoelectric effect and hence the K-edge contributions of the high-atomic-number element (for this thesis the mass attenuation coefficient of gold). $\rho_{\text{highZ}}(x)$ is the local density [g/cm^3] and δ_{highZ} represents the area density [g/cm^2] of the high-atomic-number material. Substitution of Eq. 3.24 in 2.12 results in

$$I_i(A_k) = I_{i0}\int_{E_{i-1}}^{E_i} \exp\left(-\sum_{k=1}^{K} A_k f_k\right) dE \qquad (3.25a)$$

$$\ln\left(\frac{I_{i0}}{I_i(A_k)}\right) = \int_{E_{i-1}}^{E_i} \sum_{k=1}^{3} A_k f_k dE \qquad (3.25b)$$

$$\text{with } A_k = \begin{cases} A_{\text{photo}} & k=1 \\ A_{\text{Compton}} & k=2 \\ A_{\text{highZ}} & k=3 \end{cases} \text{ and } f_k = \begin{cases} \frac{1}{E^3} & k=1 \\ f_{\text{KN}} & k=2 \\ f_{\text{highZ}} & k=3. \end{cases}$$

To solve Eq. 3.25a for the unknown coefficients A_k at least three energy bins are needed. If the measurements provide data of more than three energy bins the system is over-determined, so generally no solution exists. To be still able to solve the system a maximum-likelihood approach is used to find the coefficients A_k. Equation 3.25a describes the expected number of incident photons $I_i(A_k)$ for each bin i. The number of actually detected photons per bin is denoted as m_i. It is assumed that the detected photons form a set of independent Poisson random variables. The likelihood function for each component k is then

$$P(m_1,...,m_K|I_1(A_k),...,I_K(A_k)) = \prod_{i=1}^{K} \frac{[I_i(A_k)]^{m_i}}{m_i!}\exp(-I_i(A_k)) \qquad . \qquad (3.26)$$

To calculate the unknown coefficients A_k equation 3.26 needs to be maximized, but instead it is recommended to minimize the negative log-likelihood function $\mathcal{L}$:

$$\begin{aligned}\mathcal{L}(m_1,...,m_K|A_k) &= \sum_{i=1}^{K}[I_i(A_k) + \ln m_i! - m_i \ln I_i(A_k)] \\ &\approx \sum_{i=1}^{K}[I_i(A_k) - m_i \ln I_i(A_k)] \ \rightarrow \min \qquad . \end{aligned} \tag{3.27}$$

The I_i are calculated according to Eq. 3.25a. Terms which are not relevant for the minimization problem are neglected in the last approximation. Solving the minimization problem reveals the coefficients A_k. The solution of the maximum-likelihood approach are three raw data sets, which represent the fractional contribution to the total attenuation of the photoelectric effect, Compton scattering and the high-Z material.
Due to the identity

$$A_{\text{highZ}} = \int_0^s \widetilde{w}_{\text{highZ}}(x)dx = \delta_{\text{highZ}}$$

the reconstructed image of the high-Z material ($\widetilde{w}_{\text{highZ}}(x)$) contains the weight fraction of the high-Z material multiplied by the total density (in units of mass per volume). The unit of the reconstructed photoelectric effect image is keV^3/cm and the Compton scattering image unit is cm^{-1} [23].
Compton scattering is independent of the atomic number Z of the material (according to Equation 2.8). The soft tissues (i.e. small-atomic-number) are most prominent in the Compton images. Since the photoelectric absorption is proportional to Z^3 (Equation 2.7), the photoelectric image will mainly provide information about materials with a high-atomic-number (except the contrast agent, since that information is in the third image), e.g. bones.
A more detailed description of the algorithm can be found in [7, 74, 97, 100]. The IDL source code of the algorithm and further analysis of the K-edge decomposition are set out in the Annex. To solve the minimization problem the *constrained_min* procedure was used, which uses the generalized reduced gradient method.

3.1.4.3 Least-squares parameter estimation

Density image decomposition

The idea for the least-squares parameter estimation method is based on the work by Le and Molloi [68]. The underlying method of the algorithm is the least-squares fitting method working on the OPED-reconstructed projection data of the six energy bins. As for the eigenvector decomposition algorithm, the mass attenuation values $(\mu(E)/\rho)$ in each energy

[23] The raw data sets A_k were used for the reconstruction. It is also possible to reconstruct $A_k f_k$, with f_k calculated at the mean energy of the used spectrum. All three reconstructed images would then have the same unit cm$^-$1

bin and of P different materials of interest are required input data. For this thesis the mass attenuation values of hard bone mixture, liver and gold are used (Table 3.2).
Assuming that the mass attenuation vector $(\mu(E,x)/\rho(x))_{\text{total}} \in \mathbb{R}^K$ in each pixel is a sum of these three materials, leads to the following formulas

$$\left(\frac{\mu(E,x)}{\rho(x)}\right)_{\text{total}} = w_{\text{liver}}(x)\left(\frac{\mu(E)}{\rho}\right)_{\text{liver}} + w_{\text{bone}}(x)\left(\frac{\mu(E)}{\rho}\right)_{\text{bone}} + w_{\text{gold}}(x)\left(\frac{\mu(E)}{\rho}\right)_{\text{gold}}$$

$$\begin{aligned} \mu_{\text{total}}(E,x) &= \sum_{i=1}^{3} \widetilde{w}_i(x)\left(\frac{\mu(E)}{\rho}\right)_i \\ \widetilde{w}_i(x) &= \rho_{\text{total}}(x) w_i(x) \\ \text{with } 1 &= \sum_{i=1}^{3} w_i(x) \\ \text{with } i &= \{\text{liver, bone, gold}\} \end{aligned} \tag{3.28}$$

with w_i being the concentration (i.e. fraction by weight) of material i. The mass attenuation vectors $(\mu(E)/\rho)_i$ in each bin are calculated with XCOM [55] and the linear attenuation values $\mu_{\text{total}}(E,x)$ are obtained from the reconstructed images. The idea is now to minimize the distance between the linear attenuation values and the given mass attenuation coefficients over all bins:

$$\sum_K \left(\mu_{\text{total}}(E,x) - \sum_{i=1}^{3} \widetilde{w}_i(x)\left(\frac{\mu(E)}{\rho}\right)_i\right)^2 \rightarrow \min_{\widetilde{w}_i(x)} \quad \text{with } \widetilde{w}_i(x) \geq 0 \quad . \tag{3.29}$$

The algorithm calculates material density images $\widetilde{w}_i(x)$ for all three materials. To get the concentration $w_i(x)$, the density images need to be divided by $\rho_{\text{total}}(x)$, which can simply be calculated as $\rho_{\text{total}}(x) = \sum_{i=1}^{3} \widetilde{w}_i(x)$. The least-squares parameter estimation therefore provides the possible to determine the concentration of gold, and not only the weight fraction multiplied by the total density as the K-edge decomposition algorithm.
The IDL source code of the least-squares parameter estimation is set out in the Annex. To solve the minimization problem the *constrained_min* procedure was used, which uses the generalized reduced gradient method.

Density filter

The basic idea of this algorithm was introduced by Kalender et al. [60]. This algorithm is called the density filter, as it can only be applied to material density images, obtained by the least-squares parameter estimation algorithm described above. The algorithm is applied to each pixel individually.
The algorithm was originally intended for two material density images, which were cal-

culated from dual-energy CT measurements. However the least-squares parameter estimation generates three material density images $\widetilde{w}_i(x)$, with $i = \{\text{liver, bone, gold}\}$. In contrast to the other algorithms, the linear attenuation values $(\mu(E_{\text{mean}})/\rho)_i \in \mathbb{R}$ at the mean energy of the used X-ray spectrum are required as input. The attenuation at the mean energy of the used X-ray spectrum ($\mu_{\text{mean}}(x) \in \mathbb{R}$) can then be expressed as a sum of the density images

$$\mu_{\text{mean}}(x) = \sum_{i=1}^{3} \widetilde{w}_i(x) \left(\frac{\mu(E_{\text{mean}})}{\rho}\right)_i \quad . \tag{3.30}$$

The original algorithm can be easily adapted to three material density images (generated with the least-squares parameter estimation algorithm), if the pixel value in one image is zero or close to zero. A threshold of $t = 10^{-8}$ was used for thesis, yielding $\widetilde{w}_{i_3}(x) < t$ and $\widetilde{w}_{i_{1/2}}(x) > t$. The third term in equation 3.30 can then be neglected. The algorithm is only applied to pixels where that criterion holds, the remaining pixel values in the density images are not changed.
The first step is now to calculate high-pass filtered versions of the two density images $\widetilde{w}_{i_1}(x)$ and $\widetilde{w}_{i_2}(x)$.

$$\Delta\widetilde{w}_{i_{1/2}}(x) = \widetilde{w}_{i_{1/2}}(x) - \widehat{\widetilde{w}}_{i_{1/2}}(x) \tag{3.31}$$

$\widehat{\widetilde{w}}_{i_{1/2}}(x)$ is the median over an $n \times n$ mask (for this thesis $n = 7$). Kalender et al. [60] have demonstrated that $\Delta\widetilde{w}_{i_1}(x)$ and $\Delta\widetilde{w}_{i_2}(x)$ must have opposite sign, if they are induced by noise. The goal of the algorithm is now to calculate filtered density images $\widetilde{w}'_{i_1}(x)$ and $\widetilde{w}'_{i_2}(x)$, which should minimize pixel deviations weighted by the corresponding mass attenuation values $(\mu(E_{\text{mean}})/\rho)_{i_{1/2}}$.

$$\left[\left(\frac{\mu(E_{\text{mean}})}{\rho}\right)_{i_1} (\widetilde{w}'_{i_1}(x) - \widehat{\widetilde{w}}_{i_1}(x))\right]^2 + \left[\left(\frac{\mu(E_{\text{mean}})}{\rho}\right)_{i_2} (\widetilde{w}'_{i_2}(x) - \widehat{\widetilde{w}}_{i_2}(x))\right]^2 \rightarrow \min \tag{3.32}$$

Under the constraint that the mean linear attenuation value $\mu_{\text{mean}}(x)$ as described in Equation 3.30 should not change in the filtered images, the following condition is obtained.

$$\begin{aligned}\left(\frac{\mu(E_{\text{mean}})}{\rho}\right)_{i_1} \widetilde{w}_{i_1}(x) + \left(\frac{\mu(E_{\text{mean}})}{\rho}\right)_{i_2} \widetilde{w}_{i_2}(x) \stackrel{!}{=} \\ \left(\frac{\mu(E_{\text{mean}})}{\rho}\right)_{i_1} \widetilde{w}'_{i_1}(x) + \left(\frac{\mu(E_{\text{mean}})}{\rho}\right)_{i_2} \widetilde{w}'_{i_2}(x)\end{aligned} \tag{3.33}$$

Rearranging equation 3.33 for $\widetilde{w}_{i_1}(x)$ respectively $\widetilde{w}_{i_2}(x)$, substituting in equation 3.32 and differentiating with respect to $\widetilde{w}_{i_2}(x)$ respectively $\widetilde{w}_{i_1}(x)$ gives

$$\widetilde{w}'_{i_1}(x) = \widetilde{w}_{i_1}(x) - C(x) / \left(\frac{\mu(E_{\text{mean}})}{\rho} \right)_{i_1} \tag{3.34a}$$

$$\widetilde{w}'_{i_2}(x) = \widetilde{w}_{i_2}(x) + C(x) / \left(\frac{\mu(E_{\text{mean}})}{\rho} \right)_{i_2} \tag{3.34b}$$

with the correction term

$$C(x) = \frac{1}{2} \left[\left(\frac{\mu(E_{\text{mean}})}{\rho} \right)_{i_1} \Delta\widetilde{w}_{i_1}(x) - \left(\frac{\mu(E_{\text{mean}})}{\rho} \right)_{i_2} \Delta\widetilde{w}_{i_2}(x) \right] \tag{3.35}$$

To minimize edge artifacts, which arise when sharp density transitions are present in the images, the correction term C will be adjusted [60]. To do that it is presumed that a standard CT image can also be generated with a spectral CT, just by summing up the number of photons in each bin and then reconstructing that image $\mu_{\text{ref}}(x)$. The advantage of the standard CT image is the lower noise level. If that assumption is not valid then equation 3.30 can be used to calculate $\mu_{\text{ref}}(x)$. Now a high-pass filtered version $\Delta\mu_{\text{ref}}(x)$ of $\mu_{\text{ref}}(x)$ is calculated

$$\Delta\mu_{\text{ref}}(x) = \mu_{\text{ref}}(x) - \widehat{\mu}_{\text{ref}}(x) \tag{3.36}$$

with $\widehat{\mu}_{\text{ref}}(x)$ being again the median over an $n \times n$ mask. Filter strength is adapted by introducing a parameter ϵ to modify the correction term $C(x)$

$$C'(x) = (1 - \epsilon^2) C(x) \tag{3.37}$$

with

$$\epsilon(x) = \min \begin{cases} |\Delta\mu_{\text{ref}}(x)/\eta| \\ 1 \end{cases} \tag{3.38}$$

The parameter η should be much bigger than the pixel noise in the monoenergetic image, for this work η is set to 0.05. In comparatively homogeneous regions the pixel noise corresponds to $\Delta\mu_{\text{ref}}(x)$, and $\epsilon(x)$ approaches zero. In areas with sharp density transitions $\Delta\mu_{\text{ref}}(x)$ increases and therefore $\epsilon(x)$ increases. The filtered density images can than be calculated according to equations 3.39a and 3.39b:

$$\widetilde{w}''_{i_1}(x) = \widetilde{w}_{i_1}(x) - C'(x) / \left(\frac{\mu(E_{\text{mean}})}{\rho} \right)_{i_1} \tag{3.39a}$$

$$\widetilde{w}''_{i_2}(x) = \widetilde{w}_{i_2}(x) + C'(x) / \left(\frac{\mu(E_{\text{mean}})}{\rho} \right)_{i_2} \quad . \tag{3.39b}$$

For image areas, which are almost homogeneous, $\epsilon(x)$ approaches zero and equations 3.39a and 3.39b converge to equations 3.34a and 3.34b.

The IDL source code of the density filter is set out in the Annex.

3.2 Dose enhancement effects - Monte Carlo simulations

The second subtask of this thesis deals with the dose enhancement effects in the vicinity of gold-nanoparticles. This effect should be considered when using gold-nanoparticles as X-ray contrast agent, as it could lead to adverse effects. However, the dose enhancement effect could also be of particular interest for the application of gold-nanoparticles in radiotherapy.

3.2.1 Phantom setup

For the dose enhancement simulations a new voxel phantom was set up. The voxel phantom simulated a cell culture flask, typically used for the cell irradiation experiments (Figure 3.4). The voxel phantom had a size of $2.4 \times 5.1185 \times 5.1185\,cm^3$ ($800 \times 29 \times 29$ voxel). Each voxel had a size of $0.03 \times 1.765 \times 1.765\,mm^3$ (Figure 3.4). For the material of the flask, PMMA (polymethyl methacrylate) was used and the cell monolayer was represented by liver tissue with different concentrations of gold (0w%, 0.1w%, 0.2w%, 0.3w% and 0.4w%); the composition was the same as for the imaging simulations (Table 3.1). The gold-nanoparticles were not explicitly modeled in these simulations, instead a homogeneous distribution of gold in the tissue was modeled. The material composition of PMMA is 8.05w% hydrogen, 59.98w% carbon and 31.96w% oxygen, the density is $1.19\,g/cm^3$ and the volume is $14692\,mm^3$. The simulated cell monolayer had a thickness of $30\,\mu m$ and a volume of $70.653\,mm^3$. For simplicity, cell culture medium was replaced by water in the simulations, the volume was $48115\,mm^3$.

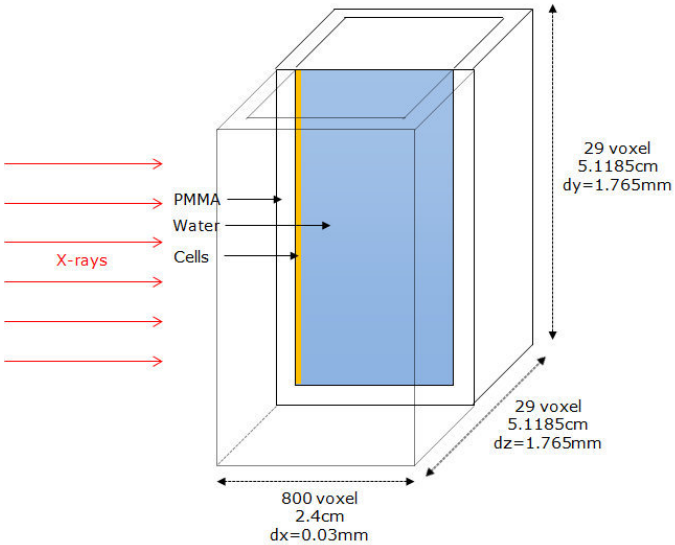

Figure 3.4: Voxel phantom of the cell culture flask used for the dose enhancement Monte Carlo simulations.

3.2.2 Spectra

The spectra used for the simulations were generated with SpekCalc [87, 88]. The required inputs were:

- energy bin width: 0.5 keV
- anode take off angle θ: 20 degree
- air thickness: 470 mm
- beryllium thickness: 0.8 mm
- aluminum thickness: 3.9 mm

The energy bin defines the interval between the calculated intensity values of the X-ray spectrum. The anode take off angle defines the angle under which X-rays are emitted. For the simulations five different polyenergetic X-ray spectra with a peak energy of 60, 80, 100, 120 and 140 kV were used (Figure 3.5).

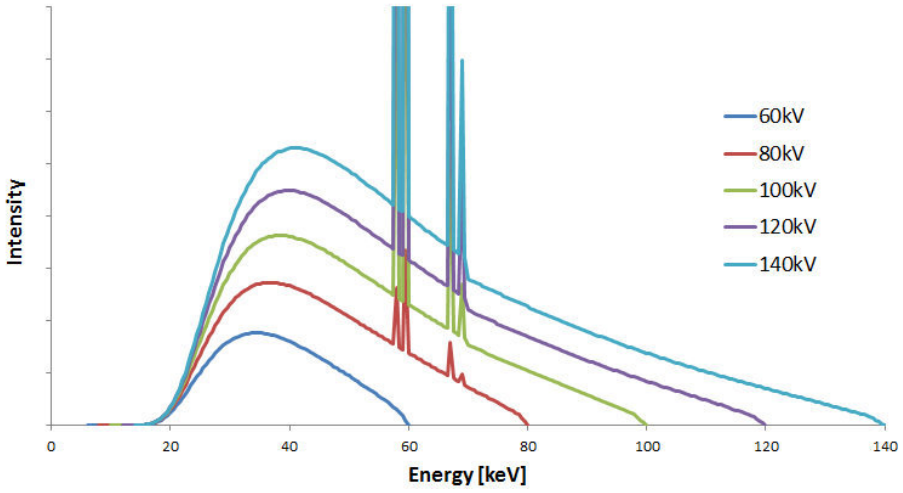

Figure 3.5: X-ray Spectra used for the dose enhancement simulations.

3.2.3 Simulation setup

Dose enhancement simulations were also performed with EGSnrc. The following code adjustments were required. To use the single-step mode in EGSnrc the *skindepth_for_bca* parameter is set to 10^{20} and *bca_algorithm* was set to 0. For each simulation 10^9 histories were used. The cutoff energy for photons and electrons was 1 keV. One simulation for each X-ray spectrum and each gold concentration was performed.

3.2.4 Evaluation

The EGSnrc user code was modified such that the output included the number and energy of produced secondary Compton, photo- and Auger-electrons and the deposited energy in each material. With these results the secondary electron spectra for all X-ray spectra and the different materials were determined.
The dose in each material can be calculated as the deposited energy in each material divided by its mass. The dose enhancement factor was defined as the ratio of absorbed dose in the tissue with gold divided by the absorbed dose without gold:

$$\text{DEF} = \frac{\text{absorbed dose with gold}}{\text{absorbed dose without gold}} \quad . \tag{3.40}$$

3.3 Internalization of gold-nanoparticles into cells - biological experiments

The main goal of these experiments was to address the question, whether the predicted concentration of gold can be specifically targeted to malignant cells. For this purpose, biological experiments with Hsp70 membrane positive cells, the cmHsp70.1 antibody and gold-nanoparticles were performed. The intended conjugation of the gold-nanoparticles and the antibody cmHsp70.1 is illustrated in Figure 3.6.

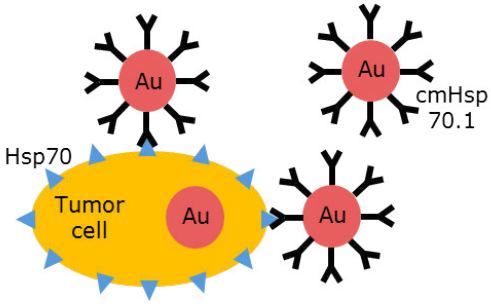

Figure 3.6: Illustration of the conjugation and binding of the gold-cmHsp70.1.

Specification of the used materials

4T1 cells

For this thesis, the tumorigenic 4T1 mouse mammary gland tumor cell line was used [8]. The 4T1 cells were kindly donated to use by the group of Prof. G. Multhoff, Klinik für Strahlentherapie, Klinikum rechts der Isar, Technische Universität München. After injection into BALB/c mice, 4T1 cells spontaneously produce highly metastatic tumors. The tumor metastasizes into the lung, liver, lymph nodes and the brain. 4T1 cells express Hsp70 on the cell membrane (personal conversation with Prof. G. Multhoff).

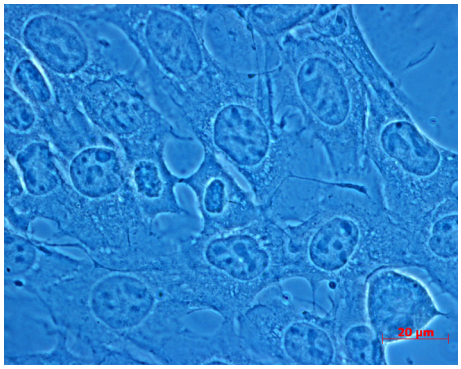

Figure 3.7: Light microscopy of 4T1 cells. The scale bar is equivalent to 20 µm.

Cultivation:
The 4T1 cells were maintained in Roswell Park Memorial Institute (RPMI) 1640 medium supplemented with 10% volume/volume (v/v) fetal calf serum (FCS), 2 mMol L-glutamine, 50 Units/ml penicillin, 50 µg/ml streptomycin, and 1 mMol sodium pyruvate at 37°C in 5% v/v CO_2, 95% humidity. Cells were maintained in the exponential growth phase by regular cell passage twice a week. They were seeded in T-75 culture flasks at constant cell densities of 2.1×10^6 cells in 20 ml conditioned medium. An optical microscope image of the cells is shown in Figure 3.7.

Subcultivation:
Remaining medium was removed and cells were washed with 10 ml phosphate buffered saline (PBS). Then the adherent growing cells were detached with 3 ml Trypsin-Ethylenediaminetetraacetic acid (Trypsin-EDTA) and were incubated for 2 min. Afterwards, 7 ml medium was added and cells were counted and subcultured into new T-75 culture flasks. Further medium was added to make up the volume to 15 ml.

Freezing:
Cells were detached from the culture flask and counted. Cells were then centrifuged at $300 \times g$ for 5 min. The supernatant was discarded without disturbing the cell pellet. Cells were then resuspended in cold freezing medium (40% medium, 50% FCS, 10% dimethyl sulfoxide (DMSO)), such that the concentration was 1×10^6 cells/ml. Aliquots of 2 ml were pipetted into cryo tubes, which were placed in a deep freeze vial filled with isopropanol and frozen at -80°C. After one day the cells were removed from the deep freeze vial and further stored at -80°C.

Thawing:
The cryo tube, containing the frozen cells, was put into a 37°C water bath until only a small piece of ice was left. Cells were then pipetted into a centrifuge tube and 10 ml medium was added dropwise (approximately 5 ml/min). Then further 10 ml medium was added and the suspension was transferred into a T-75 cell culture flask. After incubation of the cells at 37°C for 2 hours medium was removed and 15 ml fresh medium was added.

Counting:
Cell counting was performed with the FastRead-102 counting chambers (Immune Systems Ltd.); each counting chamber had ten 4×4 grids. Cell suspension was dropped near the counting chamber and capillary action drew the suspension into the chamber. Cells in three 4×4 grids were counted and the concentration was then calculated according to

$$\text{Cells/ml} = \frac{\text{total number of counted cells}}{\text{number of complete } 4 \times 4 \text{ grids counted}} \times 10^4$$

Gold-nanoparticles
Due to their characteristic optical and physical properties, gold-nanoparticles are widely used.
The gold solution, used for this thesis, was obtained from BBI Solutions (Cardiff, UK). According to BBI Solutions, their gold-nanoparticles have a superior stability, a standardized size and uniform spherical shape (>95% spherical, <5% uneven shapes). Gold-nanoparticles were suspended in water and had a red color (Figure 3.8).
50 nm gold-nanoparticles:
The particle mean diameter was 50.7 nm (coefficient of variation <8%). The concentration of the gold-nanoparticles was 1.0×10^{12} nanoparticles/ml and they had a mass of 4.77×10^{-5} g gold/ml [1]. One gold-nanoparticle consists of approximately 3.86×10^6 gold atoms and has a weight of 1.26×10^{-15} g.
15 nm gold-nanoparticles:
The particle mean diameter was 14.6 nm (coefficient of variation <8%). The concentration of the gold-nanoparticles was 4.5×10^{10} nanoparticles/ml and they had a mass of 5.68×10^{-5} g gold/ml [1]. One gold-nanoparticle consists of approximately 1.04×10^5 gold atoms and has a weight of 3.41×10^{-17} g.
The official website of BBI Solutions did not provide any information about their gold-nanoparticle synthesis and the used stabilizers.

Figure 3.8: Gold solution from BBI Solutions (image from www.bbisolutions.com).

The monoclonal antibody cmHsp70.1
Multimmune GmbH (Munich, Germany) generated the cmHsp70.1 antibody. It is an

IgG1 mouse monoclonal antibody, which specifically detects cell membrane-bound Hsp70 on viable tumor cells. Western blot, flow cytometry, and dot blot analysis revealed that this particular antibody does not cross with Hsc70 (Heat shock cognate protein 70). Hsc70 is the constitutive form, which performs physiological cellular processes, whereas Hsp70 is the stress-inducible form. Hsc70 and Hsp70 are highly homologous (84% sequence homology) [80].

3.3.1 Optimization of antibody concentration for gold-antibody conjugation

For the conjugation of the cmHsp70.1 antibody to the gold-nanoparticles, a titration series was performed to determine the minimum amount of antibody needed to stabilize the gold-nanoparticles (i.e., prevent aggregation). Addition of a sufficient amount of protein (e.g. antibodies) to the gold-solution induces a complete displacement of the citrate anions. Electrostatic and hydrophobic interaction between gold-nanoparticles and antibodies lead to a passive adsorption of the antibody to the gold-nanoparticles and by this stabilizes the gold-nanoparticles (steric stabilization). If the amount of applied protein is too small, citrate anions still coat the gold-nanoparticles. Addition of sodium chloride (NaCl) solution will then interfere with the citrate anions and the gold-nanoparticles are not stable anymore and agglomerate. This reaction induces a color change from red to blue [91].

Table 3.3: Concentrations for the titration series

Amount of gold solution	Amount of antibody	Amount of purified water	Concentration of the antibody
1 ml	0 µl	150 µl	0 µg/ml
1 ml	10 µl	140 µl	1 µg/ml
1 ml	20 µl	130 µl	2 µg/ml
1 ml	30 µl	120 µl	3 µg/ml
1 ml	40 µl	110 µl	4 µg/ml
1 ml	50 µl	100 µl	5 µg/ml
1 ml	60 µl	90 µl	6 µg/ml
1 ml	70 µl	80 µl	7 µg/ml
1 ml	80 µl	70 µl	8 µg/ml
1 ml	90 µl	60 µl	9 µg/ml
1 ml	100 µl	50 µl	10 µg/ml
1 ml	110 µl	40 µl	11 µg/ml
1 ml	120 µl	30 µl	12 µg/ml
1 ml	130 µl	20 µl	13 µg/ml
1 ml	140 µl	10 µl	14 µg/ml
1 ml	150 µl	0 µl	15 µg/ml

The titration series involves the following steps [2]. First the gold solution was adjusted to

approximately pH 9 (with NaOH or HCl). 16 clean plastic tubes were prepared and 1 ml of the gold solution was added to each tube. Afterwards the monoclonal antibody cmHsp70.1 (concentration 0.1 µg/µl) was added to each tube in a series from 0 to 150 µl and each tube was filled up to 1.15 ml with purified water (Table 3.3). After gently shaking each tube for 5 minutes, 100 µl 10% NaCl was added to each tube and shaken again for 1 minute. The tube that showed no color change from red to blue after the addition of NaCl contained the minimum amount of antibody, needed to stabilize the gold-nanoparticles. The titration series was performed for the gold-nanoparticles with a diameter of 15 and 50 nm.

3.3.2 Conjugation of gold-nanoparticles and antibody

The conjugation of the antibody cmHsp70.1 to gold-nanoparticles enables specific targeting of tumor cells. The conjugation was performed according to the protocol, which was provided by BBI Solutions [2]. With this method, antibodies conjugate to the nanoparticles surface simply by electrostatic interactions (noncovalent binding). It would be beneficial to perform the conjugation at a pH value close to the isoelectric point[24] of the antibody. Unfortunately, the isoelectric point of cmHsp70.1 was not known. After a personal conversation with group members of Prof. G. Multhoff the pH value for the conjugation was adjusted to 7.2 (with NaOH or HCl).

Three clean plastic tubes were prepared and 1 ml of the gold solution (15 and 50 nm) was put in each tube. The minimal amount of antibody, determined by the titration series, plus an additional amount of 10% was added to the gold solution. After rapidly shaking the solution for 10 minutes, 10% BSA (adjusted to pH 7.2) was added to each tube, so that the total concentration of BSA is 0.25%, 0.5% and 1%. The solution was shaken for 10 minutes. BSA covered remaining uncoated gold-nanoparticle surface areas and acted as a so called secondary stabilizer. To remove the remaining non-adsorbed antibody and BSA the tubes were centrifuged at 4°C, at $3000\times g$ for 60 minutes (50 nm gold-nanoparticles) or at $15000\times g$ for 60 minutes (15 nm gold-nanoparticles). The supernatant (containing the non-adsorbed antibody and BSA) was removed and resuspended with 1 ml 0.25% BSA (adjusted to pH 7.2). In the following sections the cmHsp70.1 antibody conjugated to gold-nanoparticles is referred to as gold-cmHsp70.1. The conjugation was performed for the gold-nanoparticles with a diameter of 15 and 50 nm.

In order to demonstrate the effect of the antibody, gold-nanoparticles were coated only with BSA as a reference. The method was exactly the same as described above, only the addition of the antibody was left out. Gold-nanoparticles coated with BSA are referred to as gold-BSA in the following sections.

To verify the conjugation of the monoclonal antibody cmHsp70.1 and the gold-nanoparticles a dot blot was performed. A dot blot is a method for the detection, analysis, and identifi-

[24] The isoelectric point denotes the pH of a protein where the positive and negative charges are equal, the protein has therefore no electrical net charge.

cation of proteins. For this technique, protein samples "dots" are directly applied onto a membrane. For the specific detection of that protein dot an antibody against that protein is added. This antibody can then be visualized with different techniques.
The dot blot was performed with the gold-nanoparticles with a diameter of 50 nm. Six pieces of the dot blot Hybond Hybond polyvinylidene difluoride (PVDF) membrane were activated as described above. On three pieces 2 µl of the Hsp70 protein and on the other three pieces 2 µl of the Hsc70 protein were applied and left to air dry. Blocking of the membrane was done by placing the membrane into PBS + 1% BSA for half an hour. The blocking solution was removed and each membrane piece was put into a small petri dish, containing 3 ml PBS + 1%, 0.5% or 0.25% BSA and 60 µl gold-cmHsp70.1. Different amounts of BSA were used to find out if that influences the conjugation. The membrane pieces were carefully wheeled for 2h and were then allowed to air dry. The method is illustrated in Figure 3.9.

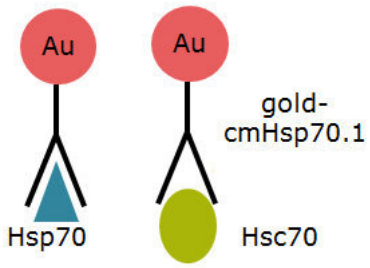

Figure 3.9: Illustration of the dot blot with the cmHsp70.1 antibody.

3.3.3 Verification of gold-antibody conjugation with UV-visible spectroscopy

UV-visible spectroscopy uses electromagnetic waves within the wavelength range of ultraviolet (UV) and visible light. For the method, electromagnetic waves of a specific wavelength penetrate the sample, get absorbed and the non-absorbed part is then detected. The location of the maximum transmittance and the intensity are characteristic properties of the sample.
If the conjugation of gold-nanoparticles and cmHsp70.1 respectively BSA was successful, the location of the maximum transmittance for the gold solution, gold-BSA and gold-cmHsp70.1 should be different. The absorption of the different gold-solutions depends on different factors such as geometry, size and the protein layer on the surface of the nanoparticles. The protein layer for this thesis was BSA or the antibody cmHsp70.1, this protein layer leads to a change of the refraction index and therefore to a change in the absorption. This change can be used as an indicator for the conjugation of the gold-nanoparticles and

a protein.
For the UV-visible spectroscopy, absorption spectra were measured using a Cary 1 Bio UV-Visible (Varian, Palo Alto, USA), scanning spectrophotometer, operated at a spectral resolution of 1 nm. The UV-visible spectrophotometer provides wavelength in the range of 250 to 900 nm with a spectral bandwidth of 0.1 to 3 nm. Each sample was measured three times and the mean absorbance was then calculated.
Gold-BSA and gold-cmHsp70.1 were prepared as described above, but the supernatant was removed after the centrifugation and the gold-nanoparticles were resuspended in millipore water instead of 0.25% BSA. The UV-visible spectroscopy was only performed for the gold-nanoparticles with a diameter of 50 nm.

3.3.4 Determination of the amount of gold per cell with ICP-OES

With inductively coupled plasma optical emission spectrometry (ICP-OES), also called inductively coupled plasma atomic emission spectroscopy (ICP-AES), trace metals can be detected. For this technique, an inductively coupled plasma is used to generate excited atoms. With the intensity of the element specific optical emission, the concentration of the trace metal in the sample can be calculated.
The amount of gold-nanoparticles in the cell or attached to the cell membrane was determined with this technique.
4T1 cells were seeded in T-75 flasks until they were about 80% confluent. Medium was removed and 7 ml fresh medium was added. Cells were then incubated with 2.24 ml gold-BSA or 2.24 ml gold-cmHsp70.1 for 6, 12 and 24 hours. After the incubation with gold-BSA/gold-cmHsp70.1 medium was removed and the cells were washed three times with PBS to remove unbound gold-nanoparticles. Cells were detached (as described above) and counted. The cell suspension was then transferred to silica glass tubes and centrifuged at $300\times g$ for 10 min, and the supernatant was removed.
The further sample preparation for the ICP-OES measurements was done by the group of Prof. Dr. Bernhard Michalke (Research Unit Analytical BioGeoChemistry, Helmholtz Zentrum München). To each tube, 1 ml aqua regia was added and a pressure digestion at 170°C was performed. Then water ad 10 ml was added. Each sample was measured at two different wavelengths with the ICP-OES. The limit of detection was approximately 2-3 µg/L in the undiluted samples, i.e. approximately 30 µg/L for the diluted samples. The ICP-OES measurements were performed for the gold-nanoparticles with a diameter of 15 and 50 nm.

3.3.5 Investigation of the spatial distribution of gold-nanoparticles in the cell with TEM

The gold-cmHsp70.1 should bind to the 4T1 cell membrane and might lead to an internalization of the gold-nanoparticles into the cell. To analyze the actual location of the

gold-nanoparticles (50 nm) transmission electron microscopy (TEM) was used.
4T1 cells were seeded in a 6-well plate and were incubated over night. Old medium was removed and 3 ml fresh medium and 0.48 ml gold-BSA (7.2×10^9 gold-nanoparticles per ml medium) was added to three wells and 3 ml fresh medium and 0.48 ml gold-cmHsp70.1 (7.2×10^9 gold-nanoparticles per ml medium) was added to the remaining three wells. Each of the 3 wells with gold-BSA/gold-cmHsp70.1 was incubated for 2, 4 and 6 hours respectively. After that time, medium was removed and cells were washed with 1 ml PBS three times. Then cells were detached, transferred to embedding capsules and centrifuged for 5 minutes at $500\times g$. The supernatant was removed and the capsules were filled with fixation solution (2.5% glutaraldehyde in 0.1M sodium cacodylate).
Further preparation steps required to obtain the TEM images were performed by the Institute of Pathology at the Helmholtz Zentrum Munich (Prof. Dr. A. Walch and Dr. M. Aichler). No further information about the sample preparation was provided.

Chapter 4

Results and Discussion

4.1 Spectral CT imaging with gold-nanoparticles - Monte Carlo simulations

The major goal of this study is to determine the minimum concentration of gold required to provide sufficient contrast in spectral CT imaging in humans. To reach this goal, Monte Carlo simulations with EGSnrc were performed.
A few preliminary considerations and investigations of photon-counting and energy-integrating detectors (without energy resolution) are presented at the beginning of this chapter. In order to solve the key problem, the influence of the energy thresholds on the detectability of gold was analyzed. In a next step the performance of the delineated algorithms were evaluated with respect to the SNR, CNR and the contrast.

4.1.1 Simulations and radiation dose

To be able to compare all simulations, the number of histories, i.e., the administered dose, for all simulations was the same. The whole body dose is calculated for the human voxel phantom. For the simulations the deposited energy in one slice is approximately 1.95 mJ[25]. The whole-body dose for a liver-spleen scan (scan length approximately 18.4 cm, yielding 210 slices) is then 7.0 mGy and the effective dose 13.0 mSv. This effective dose is comparable to a real liver-spleen scan [107]. The presented images and the calculated SNRs and CNRs in the following sections should therefore be similar to clinical CT images.
The computing time on the high performance computing - high availability - cluster is approximately four weeks (with 32 processors in parallel) for one simulation with 1160 views and 10^9 histories per view.
Hainfeld et al. [50] already tried to predict the concentration of gold required to provide sufficient contrast in spectral CT imaging in humans. Those calculations will be further analyzed in order to better assess the presented results in this thesis. With the assump-

[25]The deposited energy was simulated by Helmut Schlattl.

tion that CT scanners can detect lesions with a difference of at least 8 Hounsfield units (HU), Hainfeld et al. calculated the required concentration of gold to be 0.05w%. For their calculations they used a simplified formula and they started from the assumption of a 140 kV CT spectrum (mean energy 70 keV). This calculation is repeated with an extended formula for the 120 kV spectrum (mean energy 64.5 keV). At the mean energy the linear attenuation coefficient μ of gold is 72.59 cm^{-1}, of water 0.1994 cm^{-1}, of the liver 0.2102 cm^{-1} and of the metastasis 0.2023 cm^{-1}. The HU change can then be calculated with the following formula. The metastasis with gold is referred to as ROI.

$$\begin{aligned} \Delta\mathrm{HU} &= \mathrm{HU}_{\mathrm{ROI}} - \mathrm{HU}_{\mathrm{liver}} \\ \Delta\mathrm{HU} &= 1000\,\frac{\mu_{\mathrm{ROI}} - \mu_{\mathrm{liver}}}{\mu_{\mathrm{water}}} \end{aligned} \tag{4.1}$$

The linear attenuation coefficient of the metastasis with gold is calculated as follows. w is the fractional weight of gold.

$$\begin{aligned} \mu_{\mathrm{ROI}} &= \left(w \left(\frac{\mu}{\rho}\right)_{\mathrm{gold}} + (1-w)\left(\frac{\mu}{\rho}\right)_{\mathrm{metastasis}} \right) \rho_{\mathrm{ROI}} \\ \rho_{\mathrm{ROI}} &= w\rho_{\mathrm{gold}} + (1-w)\rho_{\mathrm{metastasis}} \\ \mu_{\mathrm{ROI}} &= aw^2 + bw + \mu_{\mathrm{metastasis}} \\ \text{with } a &= \mu_{\mathrm{metastasis}} + \mu_{\mathrm{gold}} - \left(\frac{\mu}{\rho}\right)_{\mathrm{gold}} \rho_{\mathrm{metastasis}} - \left(\frac{\mu}{\rho}\right)_{\mathrm{metastasis}} \rho_{\mathrm{gold}} \\ b &= \left(\frac{\mu}{\rho}\right)_{\mathrm{metastasis}} \rho_{\mathrm{gold}} + \left(\frac{\mu}{\rho}\right)_{\mathrm{gold}} \rho_{\mathrm{metastasis}} - 2\mu_{\mathrm{metastasis}} \end{aligned} \tag{4.2}$$

Plugging Eq. 4.2 into Eq. 4.1 and solving for the fractional weight w gives

$$\begin{aligned} w_{1/2} &= \frac{-b \pm \sqrt{b^2 - 4ac}}{2a} \\ \text{with } c &= \mu_{\mathrm{metastasis}} - \mu_{\mathrm{liver}} - \frac{\Delta\mathrm{HU}\mu_{\mathrm{water}}}{1000} \end{aligned} \tag{4.3}$$

Using the linear attenuation coefficients above and the densities given in Table 3.1 and demanding ΔHU is equal to 8, the fractional weight of gold is then $w = 0.13w\%$. The same calculation with the 140 kV spectrum of Hainfeld and ΔHU=8 gives $w = 0.14w\%$, which is almost three times the predicted concentration of Hainfeld.

4.1.2 Energy-integrating and photon-counting detectors

The first result should elucidate the performance differences of a conventional CT with a photon-counting or an energy-integrating detector. No beam shaping filter (Bowtie filter) was used to correct for cupping artifacts.

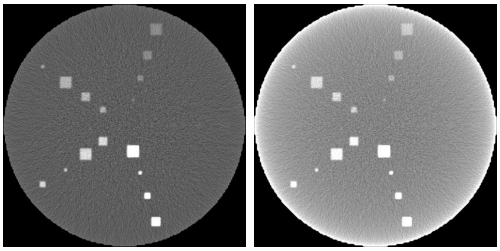

(a) photon-counting (b) energy-integrating

Figure 4.1: Summed image of the simple voxel phantom for a photon-counting and an energy-integrating detector (images are equally scaled and windowed).

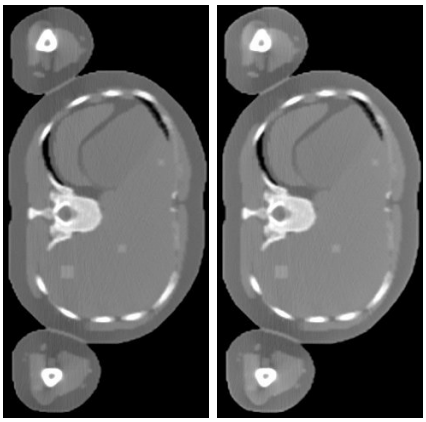

(a) photon-counting (b) energy-integrating

Figure 4.2: Summed images of the human voxel phantom with 0.3w% gold for a photon-counting and an energy-integrating detector (images are equally scaled and windowed).

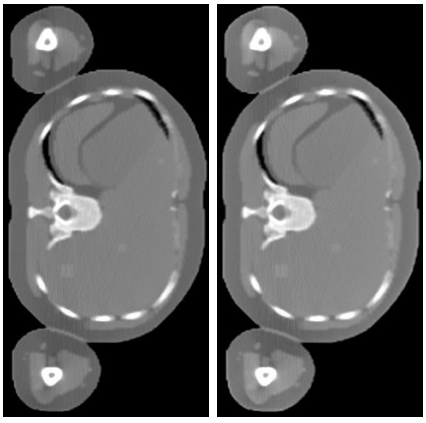

(a) photon-counting (b) energy-integrating

Figure 4.3: Summed images of the human voxel phantom with 0.2w% gold for a photon-counting and an energy-integrating detector (images are equally scaled and windowed).

The cupping artifacts in the simple voxel phantom are smaller for the photon-counting detector than for the energy-integrating detector (Figure 4.1). Calculating the percentage of cupping (Eq. 3.8) for the photon-counting detector gives 0.16% and for the energy-integrating detector 3.14%. All metastases with 0.7 down to 0.2w% gold are identifiable for both detector types. The metastases with 0.1w% gold are not visible at all. The first results indicate that at least 0.2w% gold are required to provide sufficient contrast in spectral CT imaging in humans.
The cupping artifacts in the human voxel phantom are not as pronounced as in the simple voxel phantom (Figure 4.2 and 4.3). All metastases with 0.3w% and 0.2w% gold are recognizable for both detector types.
The SNR, the (effective) CNR and the contrast were analyzed only for the biggest metastasis in the simple voxel phantom. For the human voxel phantom, the mean of all three metastases was calculated. The image quality quantities slightly favor different detectors for various combinations of phantom and gold concentration (Tables 4.1 and 4.2). However, the absence of a clear trend with gold concentration and the small differences between the two detector models do not allow the conclusion that one of the detectors is beneficial. Further investigations could be done to determine optimal weighting factors for each bin, as already described in the literature [101, 104]. As presented above all metastases with 0.2w% up to 0.7w% gold are clearly visible in all phantoms, but the metastases with 0.1w% gold are not detectable. As already mentioned in section 3.1.1.3, the effective CNR must be higher than 5 (Rose criterion). The effective CNR for the metastases with 0.1w% gold is approximately 5, but the standard deviation is very high, leading to the conclusion that the required minimum concentration of gold is approximately 0.2w%, which is close to the calculated value in section 4.1.1. The standard deviation in the liver of the human voxel phantom is 0.42 HU for the photon-counting detector and 0.67 HU for the energy-integrating detector. With these standard deviations the demanded difference of ΔHU=8, in section 4.1.1, appears to be reasonable. Micro-CT investigations by Clark et al. [33] revealed a detectability limit of approximately 0.15w% gold which is in accordance with the presented results in this thesis and the calculations in section 4.1.1.

Table 4.1: Performance results for the photon-counting and the energy-integrating detector for the simple voxel phantom.

	photon-counting				energy-integrating			
	SNR	CNR	CNR_{eff}	C	SNR	CNR	CNR_{eff}	C
0.7w% gold	26.7±1.0	5.32±0.97	106±19.7	0.115±0.021	27.7±1.0	5.33±0.99	107±19.7	0.111±0.020
0.4w% gold	60.7±1.0	5.77±1.01	115±20.2	0.0595±0.010	64.0±1.0	5.83±1.02	117±20.3	0.0571±0.010
0.3w% gold	90.2±1.0	5.43±1.06	109±21.2	0.0420±0.008	95.4±1.0	5.48±1.05	110±21.1	0.0402±0.008
0.2w% gold	116±1.0	3.73±1.04	74.7±20.9	0.0232±0.006	113±1.0	3.41±0.97	68.1±19.3	0.0218±0.006
0.1w% gold	106±1.0	0.275±0.64	5.51±12.8	0.00180±0.004	106±1.0	0.229±0.59	4.59±11.8	0.00152±0.004

Table 4.2: Performance results for the photon-counting and the energy-integrating detector for the human voxel phantom.

	photon-counting				energy-integrating			
	SNR	CNR	CNR_{eff}	C	SNR	CNR	CNR_{eff}	C
0.3w% gold	89.3±1.0	5.02±1.07	46.1±10.0	0.0374±0.008	91.3±1.0	5.05±1.07	46.3±10.0	0.0366±0.008
0.2w% gold	90.8±1.0	2.55±1.03	22.7±9.69	0.0184±0.007	93.0±1.0	2.57±1.04	22.9±9.71	0.0181±0.008

4.1.3 Optimization of detector bin thresholds

Prior to the detailed analysis of the spectral simulation results, a closer look at the relationship between the gold concentration and the bin sizes of the bin below and above the K-edge of gold is taken. The bin size below the K-edge ranged from [40,81) keV to [79,81) keV and the bin size above the K-edge from [81,83) keV to [81,120] keV.
The number of detected photons increases with increasing bin size resulting in a higher signal and reduced noise. Above the K-edge of gold, the mass attenuation values of gold decline faster than the mass attenuation values of the liver. Below the K-edge the mass attenuation values of gold increase faster than the mass attenuation values of the liver (Figure 4.4). The highest differences between the mass attenuation values of gold and liver are slightly above the K-edge and at low energies. This fact will influence the (effective) CNR and the contrast.

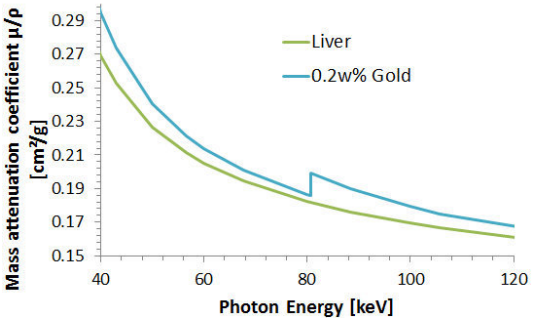

Figure 4.4: Mass attenuation curves for liver tissue and 0.2w% gold.

Simple voxel phantom

The SNR, the (effective) CNR and the contrast were analyzed only for the biggest metastasis in the simple voxel phantom.
The SNR below the K-edge increases with increasing bin size as one might expect. The SNR is lower for higher gold concentrations. The reason for this is the higher attenuation for increasing concentrations of gold, i.e., less photons are able to penetrate the object leading to lower count rates in the detector. Due to the K-edge effect the attenuation is higher in the bins above the K-edge yielding a smaller SNR (Figure 4.5). In contrast to the SNR, the effective CNR is higher for higher gold concentrations (Figure 4.6). The effective CNR increases with increasing bin size. Above the K-edge of gold the effective CNR increases rapidly for small bin sizes, but above a certain bin size, which depends on the concentration of gold, the effective CNR remains almost constant. An increase in the effective CNR is due to an increased contrast or to decreased noise (decreased variance) or both. As the bin size increases the noise decreases, but the contrast first increases up to a maximum and then decreases again (Figure 4.7). This leads to the almost constant effective CNR. For the ROI with 0.1w% gold the effective CNR below the K-edge of gold is smaller than 5, above the K-edge the effective CNR is approximately 10, however the

standard deviation is high. These results indicate that a concentration of 0.1w% gold is not detectable.

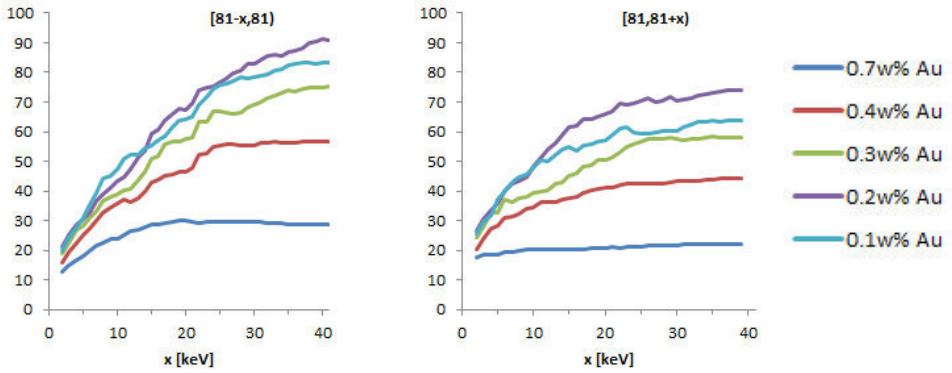

Figure 4.5: SNR in the simple voxel phantom below (left) and above (right) the K-edge for different bin sizes.

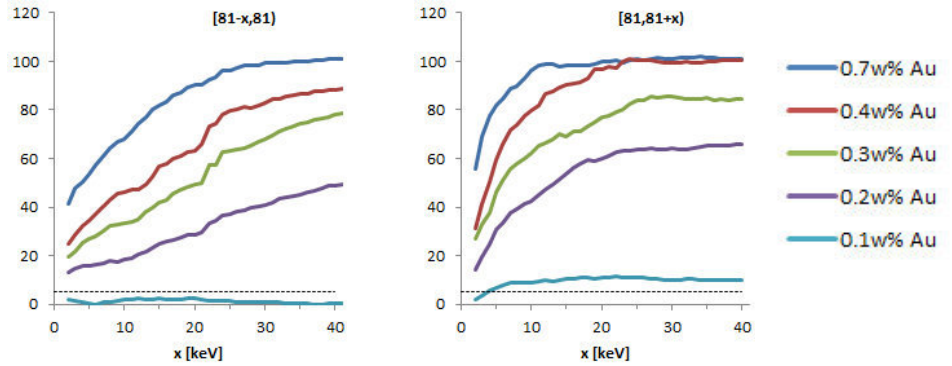

Figure 4.6: Effective CNR in the simple voxel phantom below (left) and above (right) the K-edge for different bin sizes. The dotted line represents an effective CNR of 5.

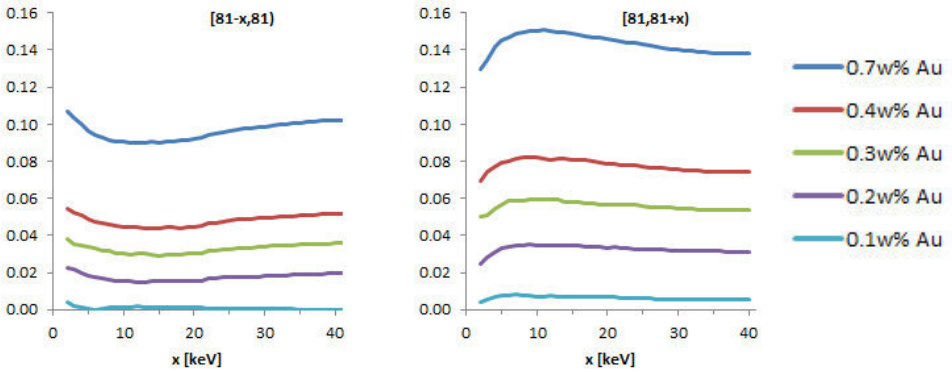

Figure 4.7: Contrast in the simple voxel phantom below (left) and above (right) the K-edge for different bin sizes.

The contrast is higher for higher gold concentrations (Figure 4.7). To derive a maximum benefit from the K-edge effect, the difference between the contrast below and above the K-edge of gold should be maximal. Below the K-edge the contrast shows a minimum for bins [70,81) keV (0.7w%), [68,81) keV (0.4w%), [66,81) keV (0.3w%), [69,81) keV (0.2w%) and [75,81) keV (0.1w%). The contrast above the K-edge shows a maximum for bins [81,91) keV (0.7w%), [81,89) keV (0.4w%), [81,91) keV (0.3w%), [81,89) keV (0.2w%) and [81,87) keV (0.1w%).
These results already indicate that smaller bin sizes seem to be beneficial.

Human voxel phantom

The same evaluations as for the simple voxel phantom were performed for the human voxel phantom with 0.3 and 0.2w% gold. The SNR, the effective CNR and the contrast were calculated as the mean of all three metastases.

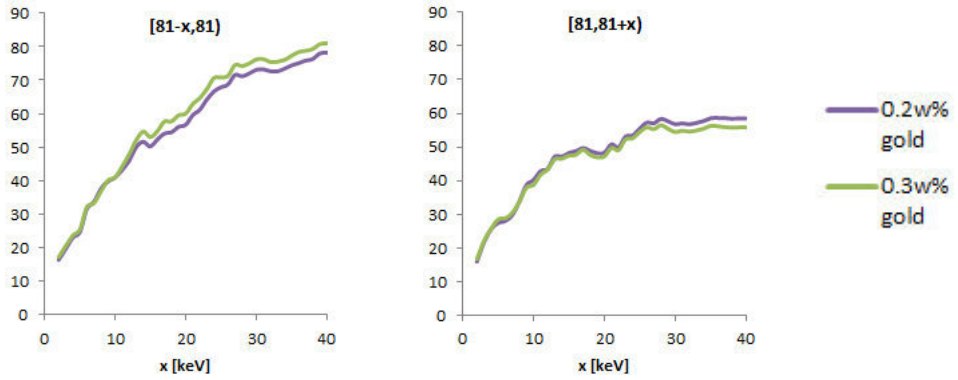

Figure 4.8: SNR in the human voxel phantom below (left) and above (right) the K-edge for different bin sizes.

As already observed in the simple voxel phantom, the SNR increases with increasing bin size for 0.3 and 0.2w% gold. The higher attenuation due to the K-edge of gold is represented by the smaller SNR above the K-edge (Figure 4.8). The SNR below the K-edge of gold is slightly higher for 0.3w% gold and above the K-edge of gold the SNR is slightly higher for the 0.2w% gold. The effective CNR in the human voxel phantom with 0.2w% gold is smaller than for the human voxel phantom with 0.3w% gold. In the human voxel phantom with 0.3w% gold the effective CNR is always higher than 5, whereas for the 0.2w% gold the effective CNR is smaller than 5 for bins [76,81), ... , [80,81), indicating that gold is not visible for those small bins. The values of the effective CNR closely match the values in the simple voxel phantom (Figure 4.9). The contrast values in the human voxel phantom are similar to the simple voxel phantom (Figure 4.10). In the human voxel phantom with 0.2w% and 0.3w% gold the contrast below the K-edge shows a minimum for bin [71,81) keV and above the K-edge the maximum is at bin [81,89) keV (Figure 4.10).

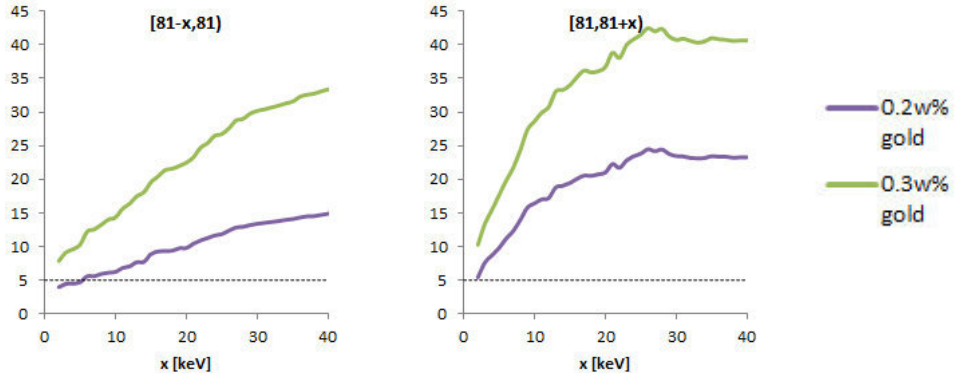

Figure 4.9: Effective CNR in the human voxel phantom below (left) and above (right) the K-edge for different bin sizes. The dotted line represents an effective CNR of 5.

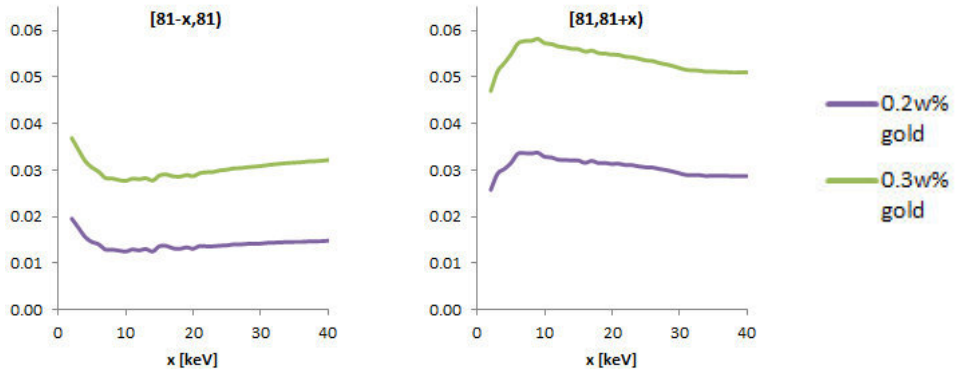

Figure 4.10: Contrast in the human voxel phantom below (left) and above (right) the K-edge for different bin sizes.

The SDNR criterion

In a next step the optimal bin thresholds for the bin below and above the K-edge of gold were calculated with respect to the maximum signal-difference-to-noise ratio (SDNR) (Eq. 3.9). The curve progression of the SDNR for the simple voxel phantom and for the human voxel phantom are shown in Figure 4.11. The results are summarized in Table 4.3 for the simple voxel phantom and Table 4.4 for the human voxel phantom.

In theory, the difference between the linear attenuation values in the bin above and below the K-edge increases with decreasing bin sizes, but noise also increases with decreasing bin sizes. The SDNR represents a compromise between a high difference and relatively small noise. Furthermore the constraint $\overline{\mu}_{\text{XCOMabove}} > \overline{\mu}_{\text{XCOMbelow}}$ must be fulfilled. As already shown in section 2.2.3 (Figure 2.5 and 2.7) the bin sizes for which that criteria holds rapidly decrease with decreasing concentrations of gold.

For the following investigations, the bin thresholds below the K-edge were set to [75,81) keV

and the bin thresholds above the K-edge were set to [81,86) keV, based on the results summarized in Table 4.4.

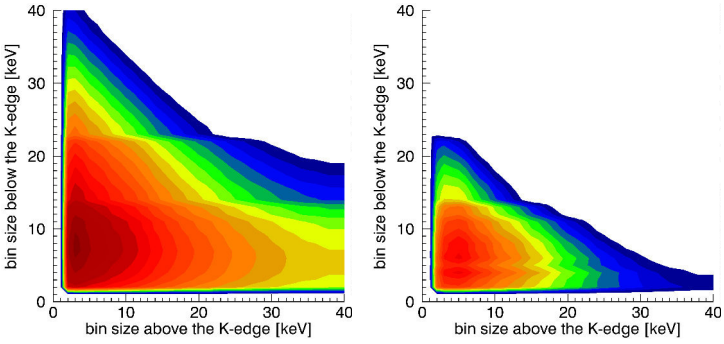

(a) Simple voxel phantom 0.7w% gold (b) Human voxel phantom 0.3w% gold

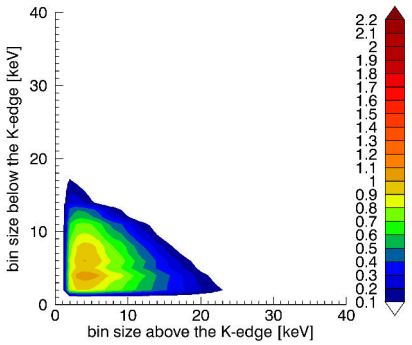

(c) Human voxel phantom 0.2w% gold

Figure 4.11: Curve progression of the SDNR.

Table 4.3: Comparison of the maximum SDNR for the simple voxel phantom.

	0.7w% Gold	0.4w% Gold	0.3w% Gold	0.2w% Gold	0.1w% Gold
below K-edge	[74,81) keV	[73,81) keV	[77,81) keV	[77,81) keV	[78,81) keV
above K-edge	[81,84) keV	[81,86) keV	[81,86) keV	[81,85) keV	[81,83) keV
maximum SDNR	2.230	1.758	1.478	0.9868	0.3969

Table 4.4: Comparison of the maximum SDNR for the human voxel phantom.

	0.3w% gold	0.2w%gold
below K-edge	[75,81) keV	[75,81) keV
above K-edge	[81,86) keV	[81,85) keV
maximum SDNR	1.295	1.297

The intensity of the X-ray spectrum above 86 keV is low, that means only a small number of photons is generated. In order to produce as little noise as possible in this bin, the bin

thresholds were set to [86,120] keV. For the remaining three bins, the intensity

$$I_i(E_{i-1}, E_i) = \int_{E_{i-1}}^{E_i} I_0(E) \exp(-\mu_{\text{Bone}}(E)x_1 - \mu_{\text{Liver}}(E)x_2)dE \qquad \text{for } i = 1, 2, 3 \quad (4.4)$$

was calculated for different bin thresholds E_{i-1}, E_i. It was assumed that X-rays are passing through 5 cm of bone (x_1) and 25 cm of liver tissue (x_2). The total distance of 30 cm is approximately the mean diameter of the human voxel phantom. The linear attenuation coefficients $\mu_{\text{Bone}}(E)$ and $\mu_{\text{Liver}}(E)$ were calculated with XCOM. The goal was to have a high difference in these intensities for each of the three bins. The first bin was set to [25,47) keV, as I_1(25 keV,47 keV) is almost equal to zero, if the upper threshold, E_1, is below 47 keV (Figure 4.12(a)). For the second bin the lower threshold E_1 is 47 keV and for the third bin the upper threshold E_3 is 75 keV. The intensity function for the second bin I_2(47 keV,E_2) and for the third bin I_3(E_2,75 keV) is shown in Figure 4.12(b). In order to have a maximal difference between all three intensities, E_2 was chosen such that

$$\begin{aligned} I_3(E_2, 75\text{keV}) - I_2(47\text{keV}, E_2) &\approx I_2(47\text{keV}, E_2) - I_1(25\text{keV}, 47\text{keV}) \\ \text{i.e. } \frac{I_3(E_2, 75\text{keV}) + I_1(25\text{keV}, 47\text{keV})}{2} &\approx I_2(47\text{keV}, E_2) \end{aligned} \quad (4.5)$$

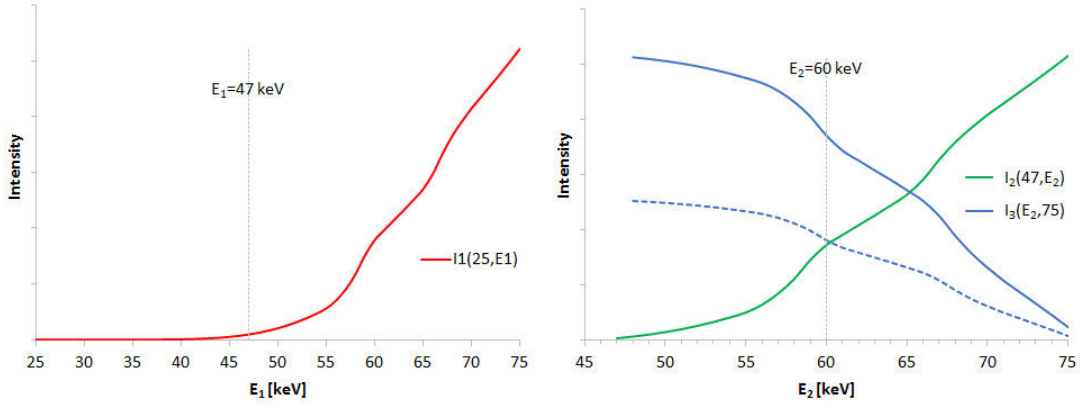

(a) Intensity function $I_1(25, E_1)$

(b) Intensity function $I_2(47, E_2)$ (green line), $I_3(E_2, 75)$ (blue line) and $(I_3(E_2, 75)+I_1(25, 47))/2$ (dotted blue line)

Figure 4.12: Evaluation of the intensity function $I_i(E_{i-1}, E_i)$ to determine the bin thresholds for the first three bins.

Equation 4.5 is represented by the dotted line in Figure 4.12(b), yielding E_2 =60 keV as a bin threshold. The bin thresholds for the third bin were set to [60,75) keV and for the second bin to [47,60) keV. (These new bin thresholds are referred to as optimized bin thresholds). For a comparison the bin thresholds were chosen according to [34], the bins were [25,34), [34,51), [51,80), [80,91), [91,110) and [110,120] keV (referred to as non-

optimized bin thresholds). The energy thresholds for the optimized and non-optimized case are shown in Figure 4.13. For the energy ranges with a low number of incident photons the bins are bigger in the optimized case and the bins just below and above the K-edge of gold are much smaller than in the non-optimized case.
It was stated that the non-optimized energy thresholds, provide the highest sensitivity with regard to simultaneous imaging of iodine and gold [34]. But the above results already indicate that the non-optimized energy thresholds are not optimal for imaging of gold in humans.
For this thesis, the SDNR was only used to calculate the optimized bin thresholds for the bin just below and just above the K-edge of gold. The remaining bin thresholds were selected considering the higher absorption of X-rays at lower energies. Therefore the bin thresholds were chosen such that the number of incident photons per bin was higher for lower energies. Further investigations could be done to improve these bin thresholds.

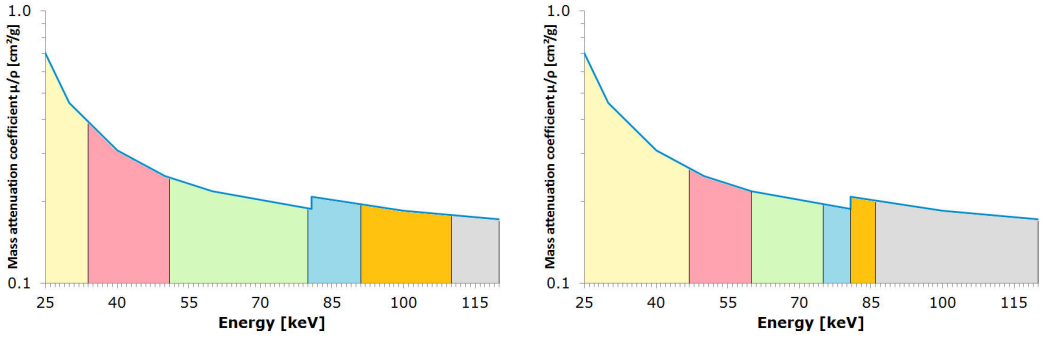

(a) Non-optimized bin thresholds (b) Optimized bin thresholds

Figure 4.13: Different bin thresholds related to the mass attenuation curve of the mixture of 0.3w% gold and liver tissue.

The purpose of the presented figures (4.14, 4.15 and 4.16) is to illustrate the big impact of the energy thresholds on the reconstructed CT images.
Especially the images in the first and the last bin show big differences. The proportion of incident photons in the first and the last bin were small for the non-optimized case. Furthermore the attenuated amount of photons is higher for lower energies. These effects are especially visible in the non-optimized [25,34) keV and [110,120] keV images, which show strong noise.

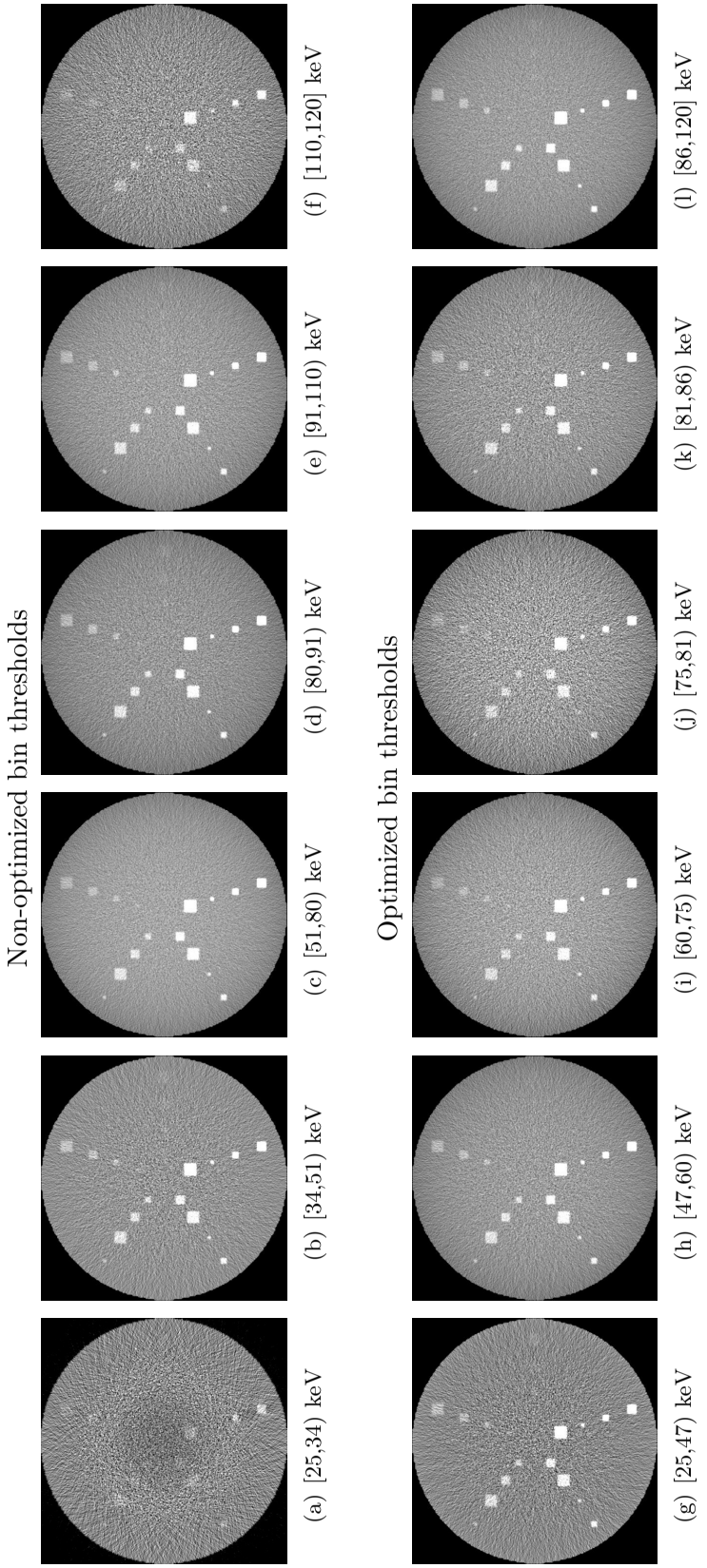

Figure 4.14: Reconstructed images for the simple voxel phantom (corresponding images are equally scaled and windowed).

Non-optimized bin thresholds

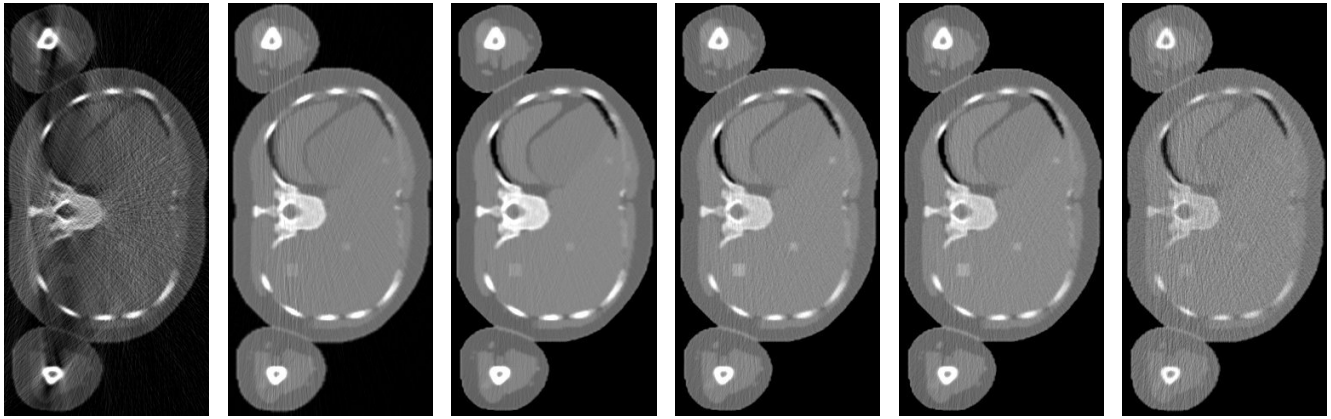

(a) [25,34) keV (b) [34,51) keV (c) [51,80) keV (d) [80,91) keV (e) [91,110) keV (f) [110,120] keV

Optimized bin thresholds

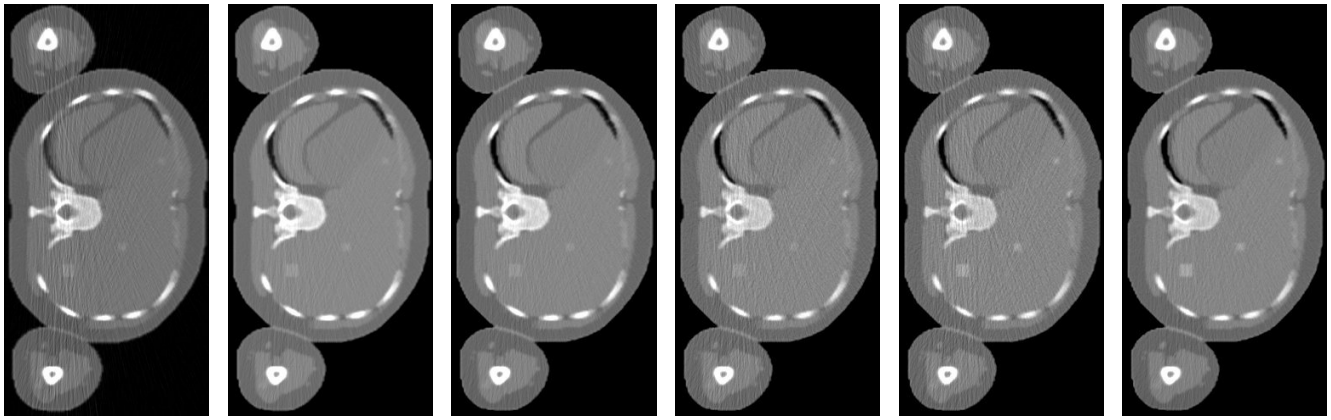

(g) [25,47) keV (h) [47,60) keV (i) [60,75) keV (j) [75,81) keV (k) [81,86) keV (l) [86,120] keV

Figure 4.15: Reconstructed images for the human voxel phantom with 0.3w% gold (corresponding images are equally scaled and windowed).

Non-optimized bin thresholds

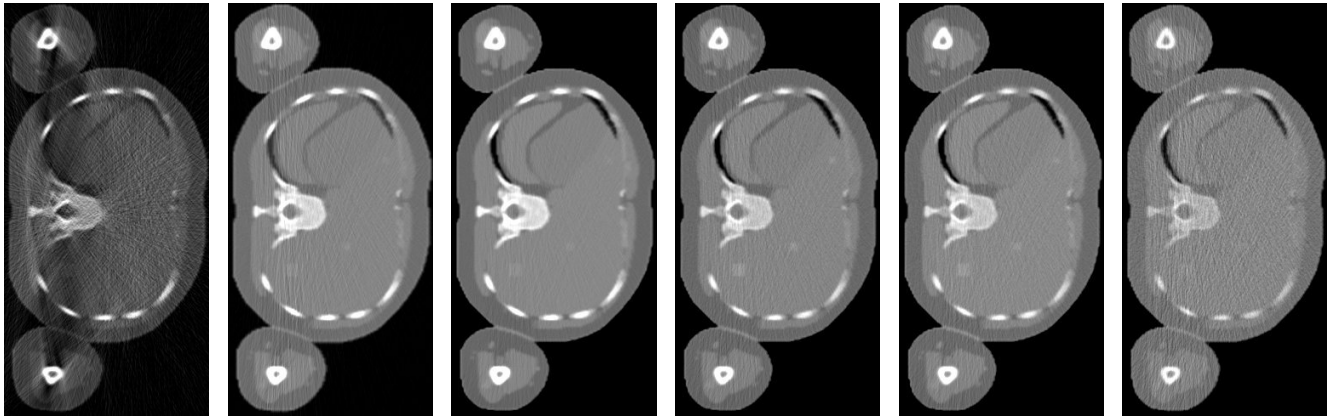

(a) [25,34) keV (b) [34,51) keV (c) [51,80) keV (d) [80,91) keV (e) [91,110) keV (f) [110,120] keV

Optimized bin thresholds

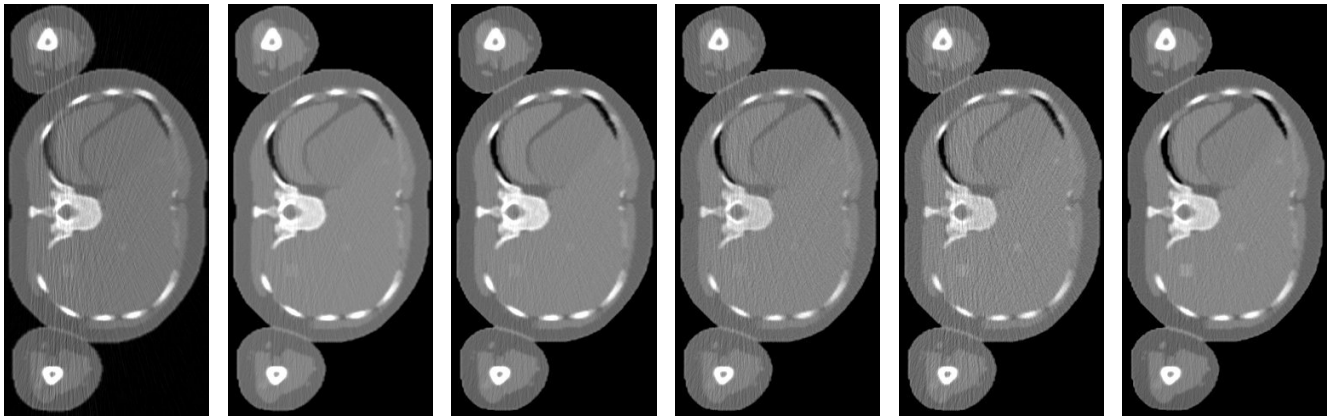

(g) [25,47) keV (h) [47,60) keV (i) [60,75) keV (j) [75,81) keV (k) [81,86) keV (l) [86,120] keV

Figure 4.16: Reconstructed images for the human voxel phantom with 0.2w% gold (corresponding images are equally scaled and windowed).

4.1.4 Material-decomposition techniques

4.1.4.1 Eigenvector decomposition

The eigenvector decomposition is basically a filter algorithm leading to a noise suppression in the energy domain. The required input data are the mass attenuation values for each bin of the basis materials (i.e. gold, hard bone mixture and liver tissue). The algorithm provides two distinct results. The first one are the noise suppressed images of each bin and the second one are images corresponding to the concentration of gold, bone and liver. The eigenvalues λ of the defined covariance matrix $M\mathrm{Cov}(\rho_{\mathrm{total}}w)M^T$ are summarized in Table 4.5. The eigenvalues relate to the whole image, not only to the metastases with gold.

Table 4.5: Eigenvalues of the covariance matrix $M\mathrm{Cov}(\rho_{\mathrm{total}}w)M^T$.

non-optimized bin thresholds	optimized bin thresholds
3.0799×10^{-1}	7.4316×10^{-1}
4.6819×10^{-3}	1.0432×10^{-2}
6.5803×10^{-7}	4.1400×10^{-7}
-1.8730×10^{-9}	1.2804×10^{-9}
-3.2922×10^{-9}	-3.6009×10^{-9}
-5.1772×10^{-10}	5.8947×10^{-9}

For this thesis only the three eigenvectors corresponding to the three largest eigenvalues will be used (i.e. $K' = 3$) to calculate the noise suppressed images. The results for the noise suppression performance of the algorithm is examined for the optimized bin thresholds in the human voxel phantom with 0.3w% gold. The difference between the unprocessed images and after the eigenvector decomposition are illustrated in Figure 4.17. The differences before and after the eigenvector decomposition are small. The images indicate that bins with a low number of photons benefit from the algorithm, this is particularly visible for bins four and five (Figure 4.17(d) and (e)). The noise suppression along the energy axis is illustrated in Figure 4.18. The linear attenuation value in the unprocessed images (blue squares) in bin 4 is too big and too small in bin 5. The K-edge effect is not correctly reflected, i.e. higher attenuation in bin 5 compared to bin 4. After applying the eigenvector decomposition algorithm the curve progression of the linear attenuation values (red dots) is very similar to the exact linear attenuation values (green triangles). The mean percentage deviation of the linear attenuation values decreases from 2.35% before the eigenvector decomposition to 1.49% after the eigenvector decomposition. The K-edge effect is correctly displayed after the eigenvector decomposition.

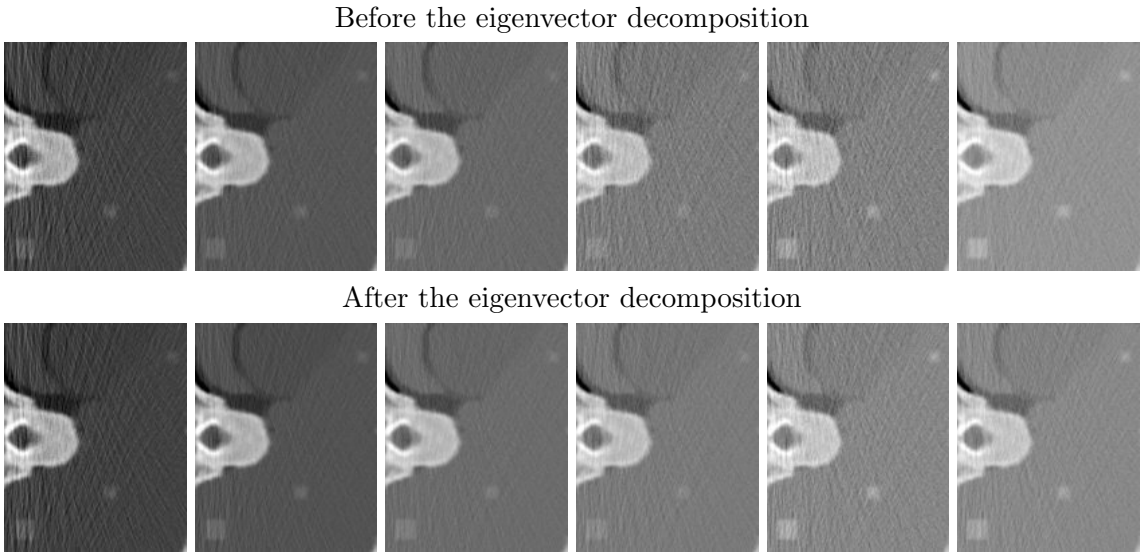

(a) [25,47) keV (b) [47,60) keV (c) [60,75) keV (d) [75,81) keV (e) [81,86) keV (f) [86,120] keV

Figure 4.17: Close-ups of the human voxel phantom with 0.3w% gold before and after the eigenvector decomposition.

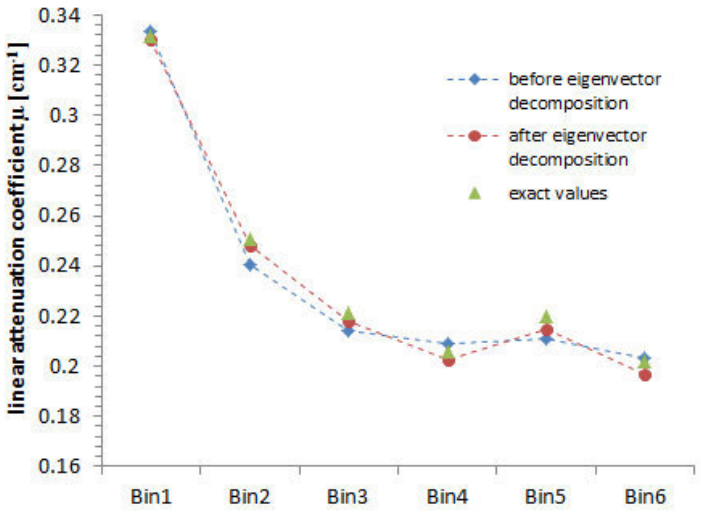

Figure 4.18: Demonstration of the noise suppression along the energy axis of the eigenvector decomposition algorithm for a single pixel inside the biggest metastasis in the human voxel phantom with 0.3w% gold (optimized bin thresholds). The blue squares correspond to the linear attenuation values in each bin in the unprocessed images. The red dots correspond to the linear attenuation values in each bin after applying the eigenvector decomposition algorithm. The green triangles show the exact linear attenuation values for each bin.

The graphs (Figure 4.19) show a clear increase of the SNR and CNR for bin 1 to 5 after the eigenvector decomposition. For bin 6 the SNR and the CNR decreases after the eigenvector decomposition. The contrast only increases for bins 2 and 5. The eigenvector

decomposition induces a SNR increase by 14.7% and a CNR increase by 12.3%. Only the contrast slightly decreases by -1.3%. In conclusion, it can be said that the eigenvector decomposition leads to a noise reduction in the images.

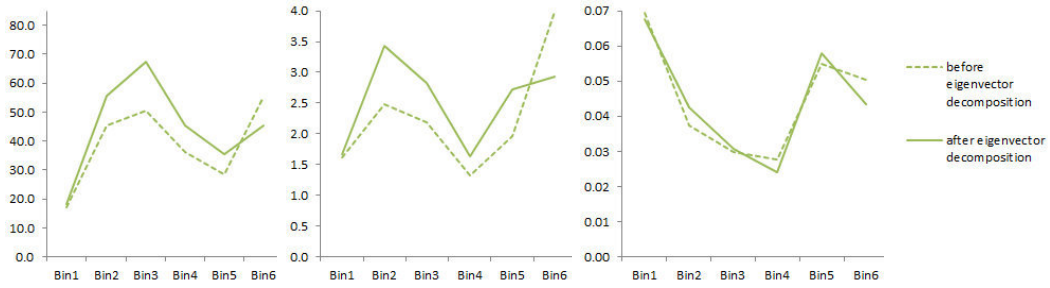

(a) SNR (b) CNR (c) Contrast

Figure 4.19: Comparing the SNR, CNR and the contrast for the human voxel phantom with 0.3w% gold (optimized case), before and after the eigenvector decomposition.

Non-optimized bin thresholds

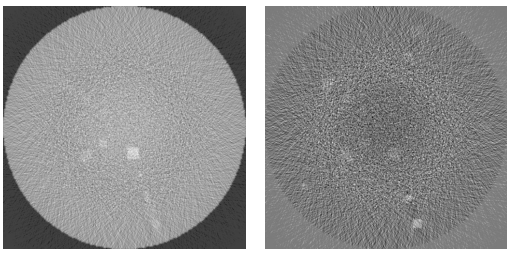

(a) Liver (b) Gold

Optimized bin thresholds

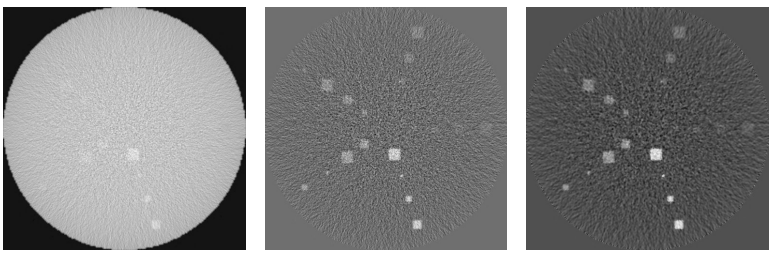

(c) Liver (d) Gold (e) Gold after bilateral filtering

Figure 4.20: Images corresponding to the concentration of gold, liver and bone of the eigenvector decomposition of the simple voxel phantom.

The images, corresponding to the concentration of the three materials (Figure 4.20), show a better result for the optimized bin thresholds than for the non-optimized bin thresholds. In Figure 4.20(d) and (e), all metastases with 0.7w% down to 0.2w% gold are identifiable. Even the metastases with 0.1w% gold are slightly visible. In the liver image (Figure 4.20(a) and (c)) a positive contribution from gold is still visible.

Non-optimized bin thresholds

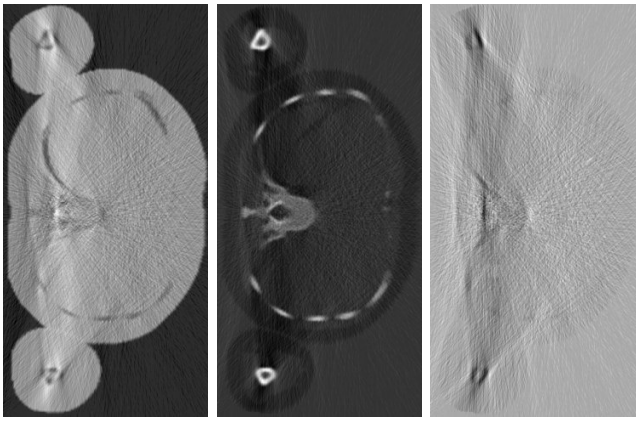

(a) Liver (b) Bone (c) Gold

Optimized bin thresholds

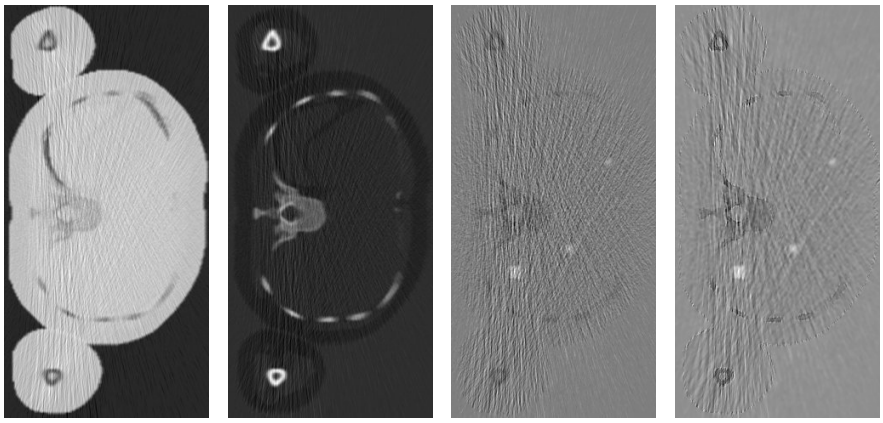

(d) Liver (e) Bone (f) Gold (g) Gold after bilateral filtering

Figure 4.21: Images corresponding to the concentration of gold, liver and bone of the eigenvector decomposition of the human voxel phantom with 0.3w% gold.

The results for the human voxel phantom with 0.3w% gold (Figure 4.21) and with 0.2w% gold (Figure 4.22) are very similar. The eigenvector decomposition achieved better results for the optimized bin thresholds, than for the non-optimized case, for which gold is barely visible. The first image (Figure4.20(a) and (d)) corresponds to liver, the second one to bone (Figure4.20(b) and (e)) and the third image (Figure4.20(c), (f) and (g)) contains the gold concentration. All three metastases with 0.3w% gold are clearly identifiable in the gold image (Figure 4.21(f) and (g)). The metastases with 0.2w% gold are barely visible in the unfiltered gold image, but they are visible in the filtered gold image (Figure 4.22(f) and (g)). The liver images (Figure 4.21(a), (d)) and Figure 4.22(a), (d)) do not provide much information. Hardly any contrast differences in the soft tissue are visible.

Non-optimized bin thresholds

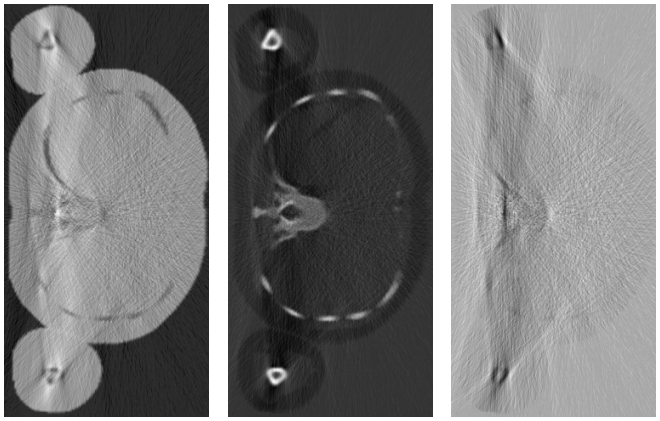

(a) Liver (b) Bone (c) Gold

Optimized bin thresholds

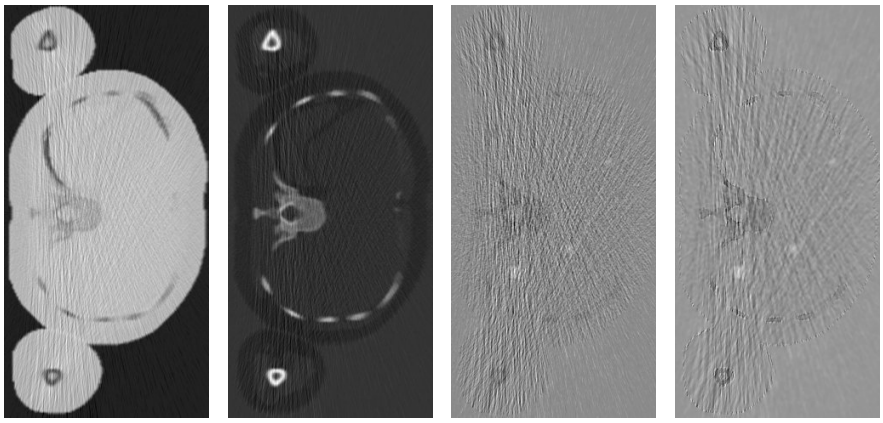

(d) Liver (e) Bone (f) Gold (g) Gold after bilateral filtering

Figure 4.22: Images corresponding to the concentration of gold, liver and bone of the eigenvector decomposition of the human voxel phantom with 0.2w% gold.

The optimized unfiltered and filtered gold images will be analyzed in more detail now. The performance results for the eigenvector decomposition are summarized in Table 4.6 and 4.7. The SNR is high, however the contrast is very low. The bilateral filter improves the SNR, (effective) CNR and the contrast for all cases. However, taking into consideration the standard deviation, the metastases with 0.1w% and 0.2w% gold in the unfiltered image can not be clearly distinguished from the background. In the filtered images all metastases have an effective CNR greater than 5, i.e. they can be clearly distinguished from the background.

Table 4.6: Performance results of the eigenvector decomposition for the optimized gold images of the simple voxel phantom.

	unfiltered				filtered			
	SNR	CNR	CNR_{eff}	C	SNR	CNR	CNR_{eff}	C
0.7w% gold	7.39±1.0	2.47±1.03	49.5±20.6	0.279±0.12	10.6±1.0	4.00±0.99	80.1±19.8	0.288±0.071
0.4w% gold	7.95±1.0	1.71±0.89	34.1±17.7	0.181±0.094	15.0±1.0	3.52±0.88	70.3±17.5	0.183±0.046
0.3w% gold	7.62±1.0	1.27±0.88	25.4±17.6	0.138±0.096	14.8±1.0	2.70±0.99	54.1±19.9	0.144±0.053
0.2w% gold	7.87±1.0	0.945±0.80	18.9±16.1	0.0930±0.079	16.1±1.0	1.96±0.96	39.1±19.1	0.0961±0.047
0.1w% gold	8.11±1.0	0.480±0.65	9.60±13.0	0.0469±0.064	18.9±1.0	1.07±0.72	21.3±14.3	0.0496±0.033

Table 4.7: Performance results of the eigenvector decomposition for the optimized gold images of the human voxel phantom.

	unfiltered				filtered			
	SNR	CNR	CNR_{eff}	C	SNR	CNR	CNR_{eff}	C
0.3w% gold	7.19±1.0	1.17±0.78	10.6±6.97	0.151±0.10	14.0±1.0	2.82±0.82	24.7±7.47	0.183±0.056
0.2w% gold	6.94±1.0	0.765±0.68	7.05±6.21	0.102±0.090	14.9±1.0	1.90±0.78	16.7±6.96	0.115±0.049

As described in equation 3.18, the concentration of gold multiplied by the total density can be calculated. The total density can be estimated according to $\rho_{\text{total}}(x) = \sum_{i=1}^{3} \widetilde{w}_i(x)$. The numerical values can then be corrected to obtain the weight fraction of gold. The results are summarized in Table 4.8. The algorithm underestimates the amount of gold for all simulations and all ROIs by 35 up to 40%. The bilateral filter algorithm reduces noise up to 57%, however the predicted concentration of gold remains almost unchanged. Further investigations about the ability of the eigenvector decomposition to estimate the gold concentration are summarized in the annex. The calculated concentrations there are in good agreement with the implemented gold concentration.

Table 4.8: Implemented gold concentration and by the eigenvector decomposition algorithm calculated weight fraction of gold multiplied by the total density (uncorrected) and the corrected weight fraction of gold.

		uncorrected		corrected	
	implemented	unfiltered	filtered	unfiltered	filtered
	0.7w% gold	0.50±0.16	0.49±0.11	0.43±0.16	0.42±0.11
simple	0.4w% gold	0.27±0.12	0.27±0.06	0.25±0.12	0.25±0.06
voxel	0.3w% gold	0.20±0.11	0.19±0.06	0.19±0.11	0.18±0.06
phantom	0.2w% gold	0.14±0.10	0.14±0.05	0.13±0.10	0.13±0.05
	0.1w% gold	0.066±0.09	0.066±0.04	0.064±0.09	0.064±0.04
human					
voxel	0.3w% gold	0.21±0.14	0.20±0.06	0.20±0.14	0.19±0.06
phantom	0.2w% gold	0.14±0.14	0.13±0.06	0.13±0.14	0.12±0.06

In Figure 4.23 the linear attenuation values in the reconstructed images for each bin and the attenuation values calculated with XCOM are compared. For liver tissue the values in the reconstructed images are consistent with the XCOM values. Only the value in the first bin is too small, which could be due to the rather high noise level in the first bin image. However, for the metastases with 0.2 and 0.3w% gold the values in the reconstructed images are clearly smaller than the XCOM values. Especially the value above the K-edge and in the first and second bin are too small. The deviations are summarized in Table 4.9. These deviations of the linear attenuation values could be the reason for the underestimation of the gold concentrations.

Table 4.9: Deviation of the linear attenuation values in the reconstructed images and the values calculated by XCOM in percent.

	Bin 1	Bin 2	Bin 3	Bin 4	Bin 5	Bin 6
Liver tissue	-3.22%	-0.78%	-0.50%	-0.14%	0.04%	-0.47%
0.2w% gold	-3.30%	-1.94%	-0.66%	0.34%	-2.23%	-0.55%
0.3w% gold	-3.91%	-2.25%	-0.86%	0.27%	-3.23%	-1.44%

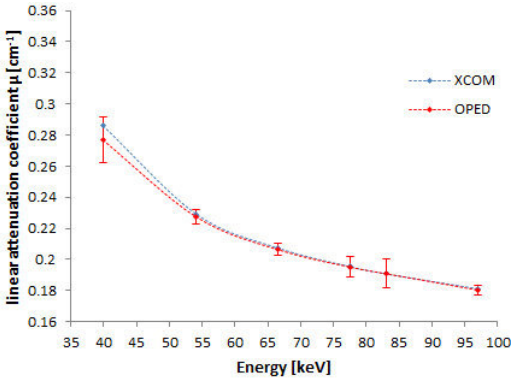

(a) Liver tissue

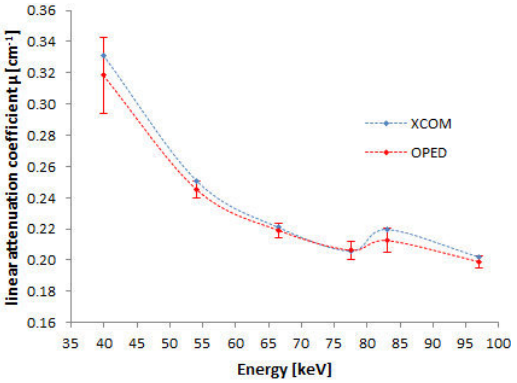

(b) 0.3w% gold

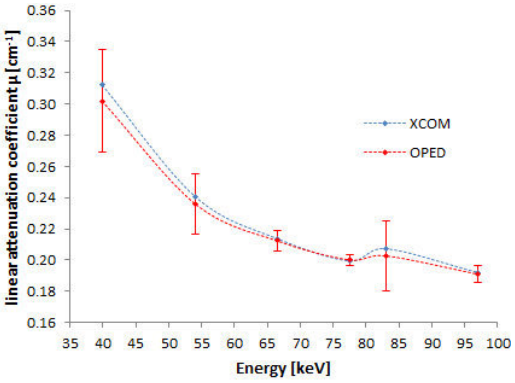

(c) 0.2w% gold

Figure 4.23: Comparing the linear attenuation values in the reconstructed images and the values calculated by XCOM.

The results indicate that a minimum amount of 0.2w% gold is required to provide sufficient contrast in spectral CT imaging. Gonzales et al. used a similar approach. The implementation of the described algorithm did not provide satisfying results for the here presented simulations, as the metastases were not visible at all.

The presented eigenvector decomposition is based on principal component analysis. The main advantage of the PCA is the possibility to reduce the dimensionality of the data, without losing a significant amount of information.

PCA was previously applied to spectral X-ray images and has yielded promising results [20]. Anderson et al. [10] used the PCA for spectral CT imaging in mice. Calcium, iodine- and barium-based contrast agents could be distinguished in the PC images. In contrast to the here presented approach, the covariance matrix was always estimated with the measured data. To my knowledge the PCA has not previously been applied to spectral images with gold-based contrast agents.

4.1.4.2 K-edge decomposition algorithm

The basic idea of the K-edge decomposition algorithm is to calculate the fractional contributions of the photoelectric effect, Compton scattering and the high-Z material to the total attenuation. The results of the K-edge decomposition method, as described in section 3.1.4.2, depend strongly on the chosen numerical target accuracy of the minimization problem. The accuracy was set to 10^{-6} for this evaluations. The linear independence of the three vectors $1/E^3$, $f_{\mathrm{KN}}(E/E_e)$ and $(\mu(E)/\rho)_{\mathrm{gold}}$ was verified with Wolfram Mathematica, enabling a clear separation of the three terms.

Non-optimized bin thresholds

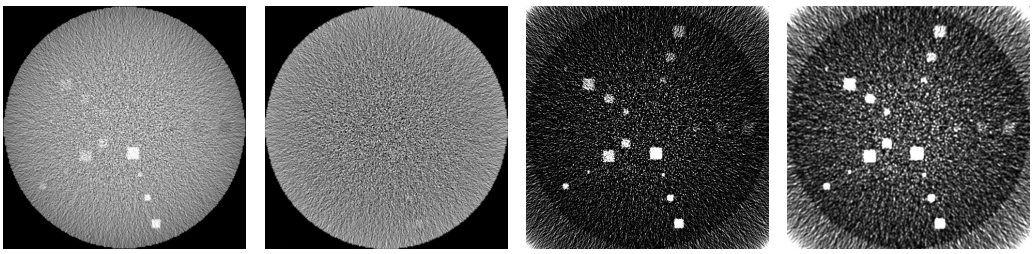

(a) Compton Effect (b) Photo Effect (c) Gold (d) Gold after bilateral filtering

Optimized bin thresholds

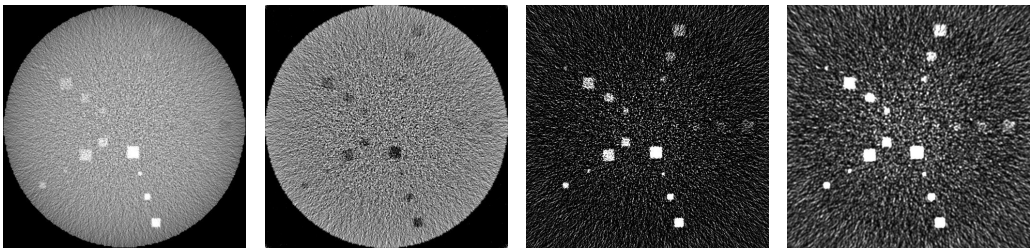

(e) Compton Effect (f) Photo Effect (g) Gold (h) Gold after bilateral filtering

Figure 4.24: Images of the K-edge decomposition algorithm of the simple voxel phantom (corresponding images are equally scaled and windowed).

The differences between the optimized and the non-optimized decomposed images (Figure 4.24) are small. In the Compton effect images (Figure 4.24(a) and (e)) the metastases with 0.7w%, 0.4w% and 0.3w% gold are still visible, the metastases with 0.2w% and 0.1w% gold are not visible. The K-edge decomposition algorithm seems to overestimate the Compton effect. As described in Equation 3.23 and 3.22 the total density ρ_{total} and the density of the low-Z material (here the metastasis) ρ_{lowZ} are taken into account in the calculation of the Compton and photoelectric effect images. If the gold concentration is low, i.e. $\rho_{\mathrm{lowZ}}(x) \approx \rho_{\mathrm{total}}(x)$ and $w_{\mathrm{lowZ}} \approx 1$, $\widetilde{C}_{\mathrm{photo}}(x)$ and $\widetilde{C}_{\mathrm{Compton}}(x)$ are not affected by gold (Equation 4.6 and 4.7). But for higher gold concentrations $\widetilde{C}_{\mathrm{photo}}(x)$ and $\widetilde{C}_{\mathrm{Compton}}(x)$ depend on $\rho_{\mathrm{total}}(x)$, and therefore on gold. The influence on the photoelectric effect is

minor, as $Z^3_{\text{lowZ}}(x) \gg \rho_{\text{total}}(x)$. But the Compton effect is proportional to $\rho_{\text{total}}(x)$ and therefore depends on gold.

$$\widetilde{C}_{\text{photo}}(x) \propto \begin{cases} Z^3_{\text{lowZ}}(x)\rho_{\text{lowZ}}(x) & \text{if } \rho_{\text{total}}(x) \approx \rho_{\text{lowZ}}(x) \\ Z^3_{\text{lowZ}}(x)\rho_{\text{total}}(x) & \text{if } \rho_{\text{total}}(x) > \rho_{\text{lowZ}}(x) \end{cases} \tag{4.6}$$

$$\widetilde{C}_{\text{Compton}}(x) \propto \begin{cases} \rho_{\text{lowZ}}(x) & \text{if } \rho_{\text{total}}(x) \approx \rho_{\text{lowZ}}(x) \\ \rho_{\text{total}}(x) & \text{if } \rho_{\text{total}}(x) > \rho_{\text{lowZ}}(x) \end{cases} \tag{4.7}$$

This seems to explain the positive contribution of gold in the Compton effect images and lead to the conclusion that the K-edge decomposition does not work effective for higher gold concentrations. In the optimized-case photoelectric image (Figure 4.24(f)) gold is clearly removed and there are "holes" in the image, where as for the non-optimized case (Figure 4.24(b)) this effect is not visible. The strong noise in the photoelectric images is partly due to the absence of materials with a high-atomic-number. The probability of the photo-effect at the used energies is therefore very low leading to high noise. The gold images (Figure 4.24(c), (d), (g) and (h)) are very noisy. Figure 4.24(d) and (h) show the gold images after applying the bilateral filter (section 3.1.1.2). The minimal concentration of gold which is clearly visible in the simple voxel phantom is 0.2w%. For the metastases with 0.1w% gold, a clear distinction between signal and noise is hardly possible. For 0.3, 0.4 and 0.7w% even the smallest metastases are clearly identifiable.

In the human voxel phantom with 0.3w% gold, all three metastases are clearly recognizable in the non-optimized and optimized case, but the images show strong noise (Figure 4.25(c), (d), (g) and (h)), which could be due to the small fractional contribution of gold compared to the total attenuation leading to strong noise in the raw data set corresponding to gold. Figure 4.25(d) and (h) show the gold images after applying the bilateral filter (section 3.1.1.2). The photoelectric effect images (Figure 4.25(b) and (f)) mainly show bones having a higher atomic number than the soft tissue. The Compton and photoelectric effect images are similar for both simulations. Gold is faintly visible in the Compton images for these simulations as well.

The results of the K-edge decomposition algorithm for the human voxel phantom with 0.2w% gold are shown in Figure 4.26. Again the photoelectric images (Figure 4.26(b) and (f)) mainly show bones and the Compton and photoelectric effect images are similar for both simulations. For the 0.2w% gold, it is harder to distinguish between noise and signal in the gold images (Figure 4.26(c), (d), (g) and (h)). Figure 4.26(d) and (h) show the gold images after applying the bilateral filter, all three metastases are identifiable in the non-optimized and optimized case.

Non-optimized bin thresholds

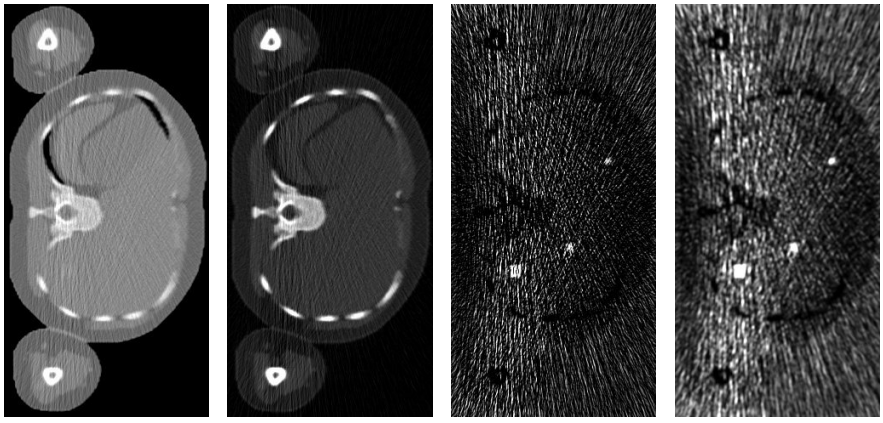

(a) Compton Effect (b) Photo Effect (c) Gold (d) Gold after bilateral filtering

Optimized bin thresholds

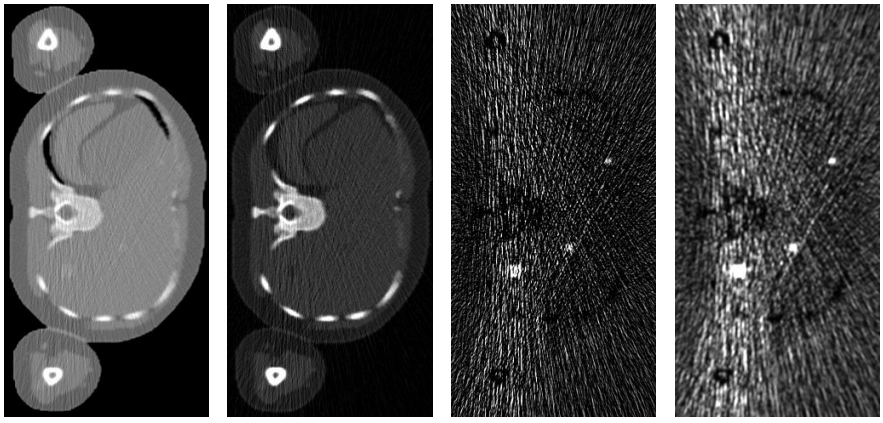

(e) Compton Effect (f) Photo Effect (g) Gold (h) Gold after bilateral filtering

Figure 4.25: Images of the K-edge decomposition algorithm of the human voxel phantom with 0.3w% gold (corresponding images are equally scaled and windowed).

The optimized gold images of all three simulations are now analyzed in more detail, the results are summarized in Table 4.10 and 4.11. Images were filtered with the bilateral filter algorithm first and were then evaluated with respect to the SNR, (effective) CNR and the contrast.

All filtered images provide an effective CNR higher than 5, indicating that the ROIs can be distinguished from the background. The differences between the non-optimized and optimized bin thresholds are not significant, making it difficult to decide which bin-thresholds should be preferred.

In comparison to the results of the photon-counting and energy-integrating detector (Table 4.1 and 4.2), the contrast is much higher. In the human voxel phantom with 0.3w% gold the contrast is 19 times higher and 33 times higher for the 0.2w% gold. The SNR is 81 up

to 97% smaller than for the photon-counting or energy-integrating detector. The CNRs are clearly smaller for almost all K-edge decomposition gold images, with the exception of 0.1w% gold in the simple voxel phantom having a 4 times higher CNR and a more than 200 times higher contrast than for the photon-counting and energy-integrating detector. However, the ROIs with 0.1% gold are barely recognizable in the image (Figure 4.24(c), (d), (g) and (h)). The results of the K-edge decomposition algorithm also predict a minimal gold concentration of 0.2w% gold.

Non-optimized bin thresholds

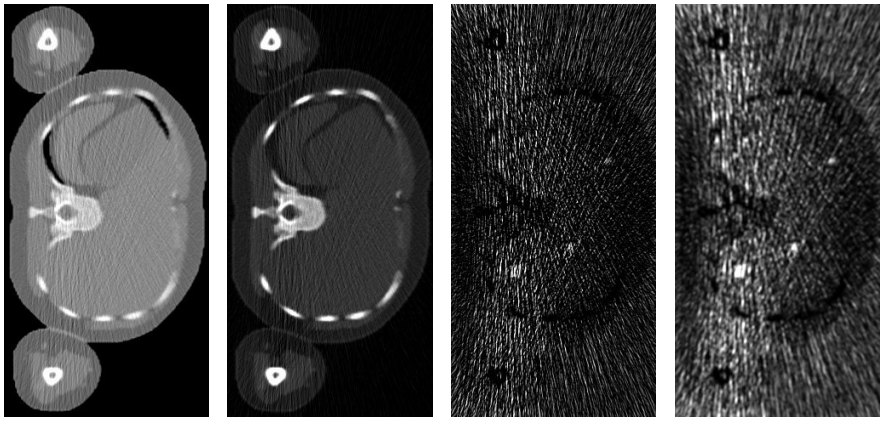

(a) Compton Effect (b) Photo Effect (c) Gold (d) Gold after bilateral filtering

Optimized bin thresholds

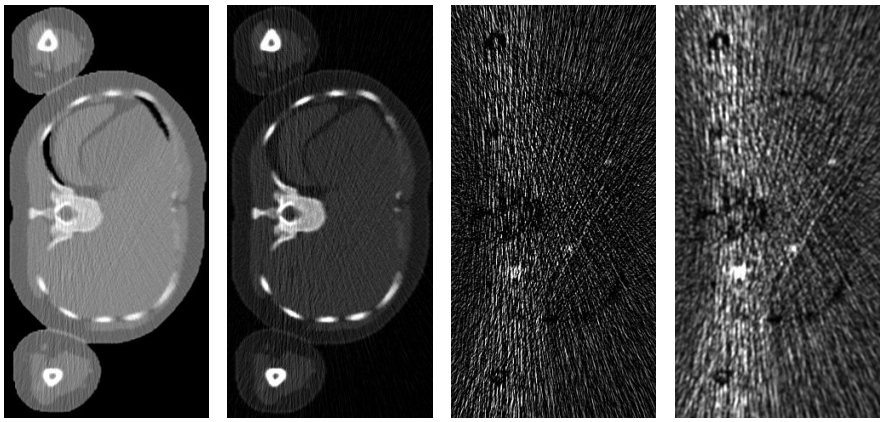

(e) Compton Effect (f) Photo Effect (g) Gold (h) Gold after bilateral filtering

Figure 4.26: Images of the K-edge decomposition algorithm of the human voxel phantom with 0.2w% gold (corresponding images are equally scaled and windowed).

Table 4.10: Performance results of the K-edge decomposition algorithm for the non-optimized and optimized gold images of the simple voxel phantom.

		non-optimized bin thresholds				optimized bin thresholds			
		SNR	CNR	CNR_{eff}	C	SNR	CNR	CNR_{eff}	C
0.7w% gold	unfiltered	3.50±1.0	2.98±1.02	59.6±20.3	0.859±0.29	3.54±1.0	3.03±1.02	60.7±20.4	0.859±0.29
	filtered	4.97±1.0	4.45±1.00	89.0±20.0	0.848±0.19	5.11±1.0	4.60±0.98	92.0±19.5	0.857±0.18
0.4w% gold	unfiltered	2.63±1.0	2.09±0.97	41.9±19.3	0.786±0.36	2.69±1.0	2.16±0.96	43.2±19.2	0.799±0.36
	filtered	4.92±1.0	4.09±1.00	81.7±20.1	0.777±0.19	5.25±1.0	4.39±1.00	87.9±20.1	0.792±0.18
0.3w% gold	unfiltered	2.01±1.0	1.58±0.95	31.5±19.1	0.747±0.45	2.09±1.0	1.55±0.89	31.1±17.9	0.720±0.41
	filtered	4.39±1.0	3.49±0.99	69.7±19.8	0.747±0.21	4.68±1.0	3.43±0.98	68.6±19.6	0.722±0.21
0.2w% gold	unfiltered	1.73±1.0	1.15±0.87	22.9±17.4	0.630±0.48	1.77±1.0	1.18±0.86	23.6±17.2	0.621±0.45
	filtered	4.43±1.0	2.89±1.00	57.7±20.1	0.632±0.22	3.95±1.0	2.72±0.95	54.3±19.0	0.623±0.22
0.1w% gold	unfiltered	1.11±1.0	0.466±0.73	9.31±14.5	0.366±0.57	1.17±1.0	0.487±0.69	9.75±13.9	0.355±0.50
	filtered	2.88±1.0	1.20±0.79	24.0±15.8	0.375±0.25	2.69±1.0	1.19±0.81	23.8±16.1	0.365±0.25

Table 4.11: Performance results of the K-edge decomposition algorithm for the non-optimized and optimized gold images of the human voxel phantom.

		non-optimized bin thresholds				optimized bin thresholds			
		SNR	CNR	CNR_{eff}	C	SNR	CNR	CNR_{eff}	C
0.3w% gold	unfiltered	1.86±1.0	1.42±0.90	13.0±8.37	0.712±0.46	2.10±1.0	1.52±0.95	13.5±8.63	0.692±0.46
	filtered	5.18±1.0	3.86±0.91	35.5±8.53	0.708±0.17	6.64±1.0	4.76±0.89	43.4±8.18	0.697±0.15
0.2w% gold	unfiltered	1.44±1.0	0.945±0.83	8.76±7.89	0.603±0.53	1.59±1.0	1.01±0.88	9.44±8.10	0.573±0.50
	filtered	4.17±1.0	2.67±0.88	24.2±8.14	0.596±0.20	5.31±1.0	3.29±1.01	30.5±9.33	0.582±0.19

The numerical values in the gold images of the K-edge decomposition algorithm contain the weight fraction of gold multiplied by the total density (in units of mass per volume). For the simulations the total density is known (Table 3.1) and the numerical values can be corrected to obtain the weight fraction of gold, however in clinical practice the total density is not known. The results are summarized in Table 4.12. The K-edge decomposition algorithm underestimates the concentration of gold by an average of 36% for all ROIs and both phantoms. The bilateral filter algorithm reduces noise (up to 73% and on average 57%), however the predicted concentration of gold remains almost unchanged. The underestimation could be due to the positive contribution of gold in the Compton effect images.

Table 4.12: Implemented gold concentration and by the K-edge decomposition algorithm calculated weight fraction of gold multiplied by the total density (uncorrected) and the corrected weight fraction of gold.

		uncorrected		corrected	
	implemented	unfiltered	filtered	unfiltered	filtered
	0.7w% gold	0.52±0.15	0.51±0.10	0.45±0.15	0.44±0.10
simple	0.4w% gold	0.28±0.10	0.27±0.05	0.26±0.10	0.25±0.05
voxel	0.3w% gold	0.20±0.10	0.20±0.04	0.19±0.10	0.19±0.04
phantom	0.2w% gold	0.14±0.08	0.14±0.03	0.13±0.08	0.13±0.03
	0.1w% gold	0.068±0.06	0.069±0.03	0.065±0.06	0.066±0.03
human					
voxel	0.3w% gold	0.21±0.11	0.20±0.03	0.20±0.11	0.19±0.03
phantom	0.2w% gold	0.15±0.10	0.14±0.03	0.11±0.10	0.13±0.03

The efficiency of the K-edge decomposition algorithm was already previously demonstrated in Monte Carlo simulations and real measurements. One of the first K-edge imaging simulations (Radonis CT-simulation package, Philips Research Hamburg) was applied to a artherosclerotic coronary vessel phantom. The used gadolinium concentrations in the coronary artery were 31.76 mg/ml (approximately 3.176w%) [97]. Feuerlein et al. [40] also used a vessel phantom partly filled with a gadolinium-based contrast agent (0.05 mol/L of Magnevist; Bayer-Schering Pharma, Leverkusen, Germany) for their measurements at the Philips Healthcare spectral CT. The spectral data and the K-edge imaging algorithm enabled the distinct detection of atherosclerotic plaques and the gadolinium-based contrast agent in both cases.

The K-edge decomposition algorithm can be extended using it for more than one contrast agent at the same time. The measurements and calculations done by Schlomka et al. [100] provide good results for simultaneous imaging of gadolinium- (30, 60 and 120 µmol/ml, approximately 0.47, 0.94 and 1.89w%) and iodine-based contrast agents (37.5, 75, and 150 µmol/ml, approximately 0.95, 1.91 and 3.81w%). The actual and the calculated concentrations were in good agreement. The simultaneous detection of gold and iodine in

an artery phantom was analyzed by Cormode et al. [34]. They furthermore injected mice with 500 mg gold-HDL/kg[26] body weight and performed the spectral CT measurements (Philips Healthcare) 24h after injection. The K-edge decomposition algorithm clearly identified the gold-HDL in plaques in the aorta, but the final gold concentration in these plaques was not investigated. Therefore no conclusion can be drawn about the required gold concentration which needs to accumulate in the target tissue.
Baturin et al. [15] applied the K-edge decomposition algorithm to two simulated phantoms. A small phantom (diameter 3 cm) containing 1.4 to 3.4 mg gold per cm^3 (approximately 1.4 to 3.4w%) was used for calibration measurements. The calculated gold concentrations corresponded well with the known concentrations and gold was identifiable in the decomposed images. The second phantom was a chest phantom ($33 \times 24\,cm^2$) containing one point of interest (diameter 2 mm) with a water-based iodine-gold-calcium mixture. The concentration of gold and iodine in the chest phantom was not specified. It is therefore not possible to relate these calculations to this thesis.
According to the references discussed above, the K-edge decomposition algorithm provided promising results with respect to the detection of the high-Z contrast agent and the calculated contrast agent concentrations. But the contrast agent concentrations were rather high, or in some cases not specified. To my knowledge, the impact of contrast agent concentration and the bin thresholds on the performance of the algorithm was not investigated yet. The here presented results demonstrate the strong dependency of the algorithm on the contrast agent concentration and the bin thresholds.
It should be mentioned that the decomposed raw data sets for the photoelectric effect and the high-atomic-number material contained negative values. Further investigations were performed and are outlined in the annex.

4.1.4.3 Least-squares parameter estimation

The least-squares parameter estimation is based on the least-squares fitting method. It is assumed that the tissue in each pixel is a combination of three basis materials (here: liver, hard bone mixture and gold). The mass attenuation values of these basis materials were used to fit the values in each pixel. The density filter was then applied to the material density images.
The results for all three phantoms are shown in Figure 4.27, 4.28 and 4.29. The least square parameter estimation also provides better results, with respect to the detection of gold, for the optimized bin thresholds than for the non-optimized bin thresholds. Especially in the liver images, and the gold images the density filter decreases the noise level compared to the images without the density filter.
The liver image (Figure 4.27(c)) should mainly contain the information related to the liver

[26] HDL means high density lipoprotein, which is specific for macrophages. It was used to identify plaques in the aorta containing numerous macrophages.

(representative for soft tissue), but gold is still visible in that image. In the gold image (Figure 4.27(d)) the metastases with 0.7w% down to 0.3w% gold are recognizable, but the image has a high noise level. The metastases with 0.2w% gold can be hardly identified due to the high noise level. In the images with the density filter (Figure 4.27(f) and (g)) all metastases with 0.7w%, 0.4w% and 0.3w% are clearly identifiable. For 0.2w% gold only the smallest metastasis can not be distinguished from noise, the other metastases are visible. The metastases with 0.1w% gold are not detectable.
The results of the least-squares parameter estimation for the human voxel phantom with 0.3w% gold are shown in Figure 4.28. The first images (Figure 4.28(a) and (d)) mainly show the soft tissue (calculated with the energy dependent mass attenuation coefficients of the liver). The second images (Figure 4.28(b) and (e)) are related to bone and the third images are related to gold (Figure 4.28(c) and (f)). The optimized images show less noise than the non-optimized images. In the optimized case the three metastases are hard to identify due to the high noise level (Figure 4.28(f)), but in the non-optimized case the metastases are not identifiable at all (Figure 4.28(c)). All three metastases can be detected easily in the images with the density filter (Figure 4.28(j)).
The algorithm performs also better for the optimized bin thresholds than for the non-optimized bin thresholds in the human voxel phantom with 0.2w% gold. The first two images (related to soft tissue and bone) of the least-squares parameter estimation algorithm (Figure 4.29) are similar for the human voxel phantom with 0.2w% and the 0.3w% gold, since the properties of soft tissue and bones are the same for both simulations. In the gold image (Figure 4.29(f)), the metastases are hardly identifiable. In the images with the density filter the three metastases are still hard to distinguish from noise (Figure 4.29(j)).
The performance results for the least-squares parameter estimation are summarized in Table 4.13 and 4.14. The bilateral filter improves the SNR, (effective) CNR and the contrast for almost all cases, the exceptions are the contrast for the 0.3w% and the 0.2w% gold in the simple voxel phantom. The SNR is on average 2.4 times higher with the bilateral filter, but with the density filter only 1.5 times higher. The CNR is on average 2.4 times higher with the bilateral filter and 1.7 times higher with the density filter. The SNR and the CNR for all metastases is lower than for the K-edge decomposition. The effective CNR for the ROI with 0.1w% gold is higher than 5 for all cases, but the standard deviation is very high, the metastasis with 0.1w% gold can therefore not be clearly distinguished from background. The contrast is very similar for both algorithms. The K-edge decomposition provides a slightly higher contrast for the 0.2w% and the 0.1w% gold in the simple voxel phantom and in the human voxel phantom for the unfiltered 0.3w% gold and the 0.2w% gold. In the other cases the contrast is slightly higher for the least-squares parameter estimation.

Non-optimized bin thresholds without density filter

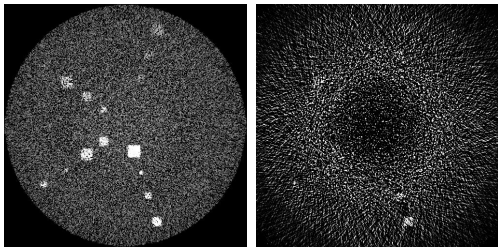

(a) Liver (b) Gold

Optimized bin thresholds without density filter

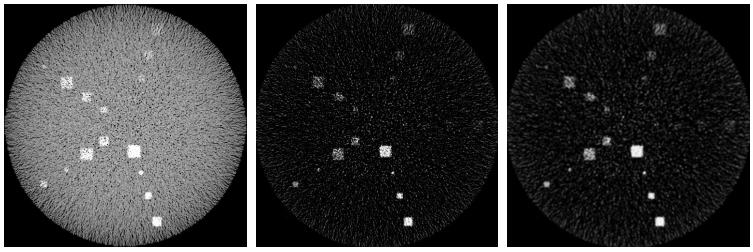

(c) Liver (d) Gold (e) Gold after bilateral filtering

Optimized bin thresholds with density filter

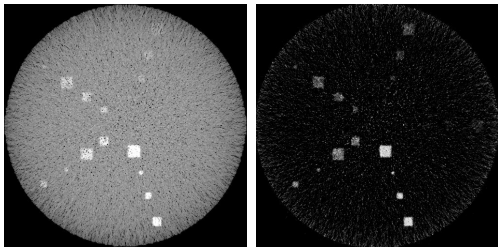

(f) Liver (g) Gold

Figure 4.27: Least-squares parameter estimation of the simple voxel phantom (corresponding images are equally scaled and windowed).

Non-optimized bin thresholds without density filter

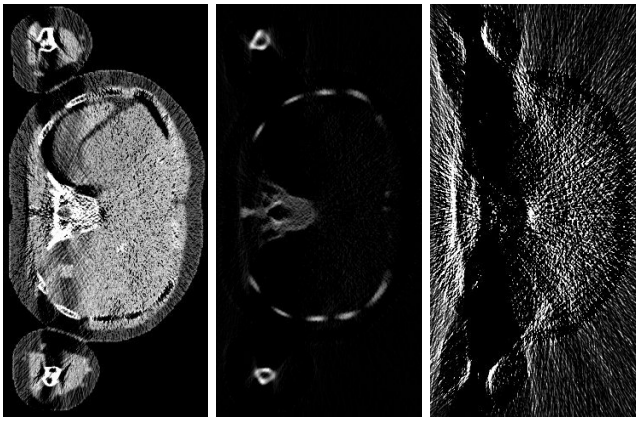

(a) Liver (b) Bone (c) Gold

Optimized bin thresholds without density filter

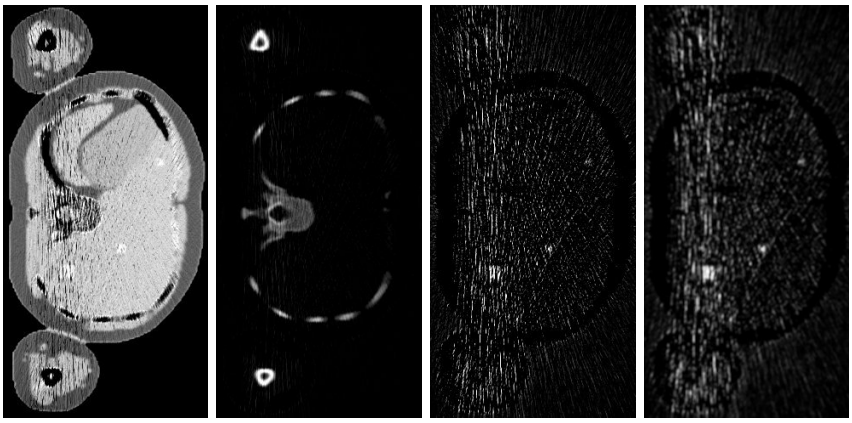

(d) Liver (e) Bone (f) Gold (g) Gold after bilateral filtering

Optimized bin thresholds with density filter

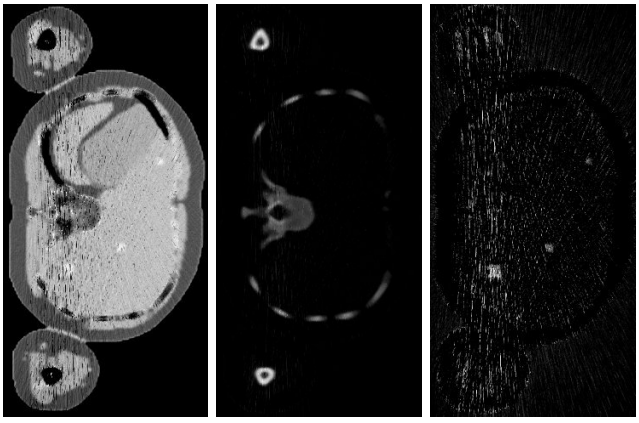

(h) Liver (i) Bone (j) Gold

Figure 4.28: Least-squares parameter estimation of the human voxel phantom with 0.3w% gold (corresponding images are equally scaled and windowed).

Non-optimized bin thresholds without density filter

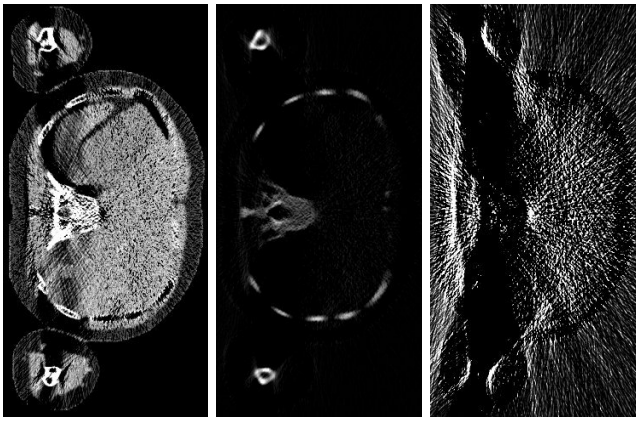

(a) Liver (b) Bone (c) Gold

Optimized bin thresholds without density filter

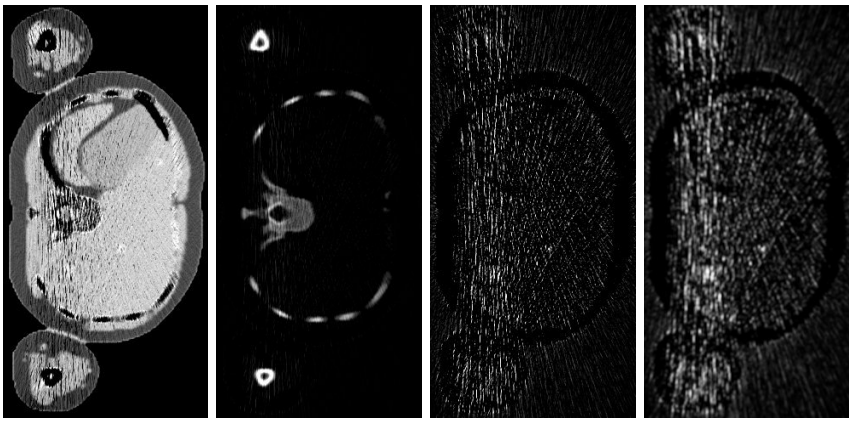

(d) Liver (e) Bone (f) Gold (g) Gold after bilateral filtering

Optimized bin thresholds with density filter

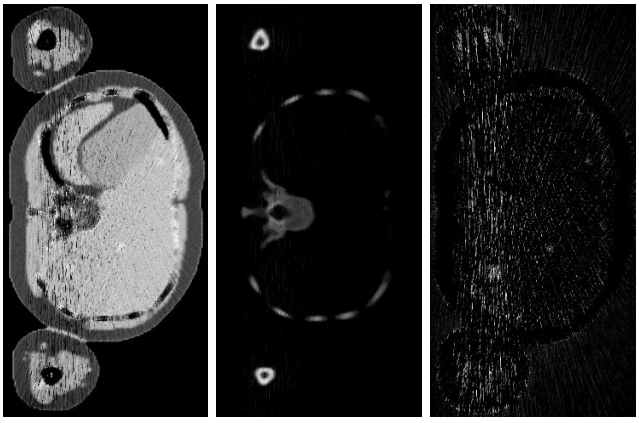

(h) Liver (i) Bone (j) Gold

Figure 4.29: Least-squares parameter estimation of the human voxel phantom with 0.2w% gold (corresponding images are equally scaled and windowed).

Table 4.13: Performance results of the least-squares parameter estimation for the optimized gold images of the simple voxel phantom.

	SNR	CNR	CNR_{eff}	C
	unfiltered			
0.7w% gold	2.62±1.0	2.36±1.00	47.2±20.0	0.889±0.38
0.4w% gold	1.83±1.0	1.54±0.92	30.8±18.5	0.822±0.49
0.3w% gold	1.37±1.0	1.08±0.89	21.6±17.8	0.747±0.61
0.2w% gold	1.26±1.0	0.832±0.82	16.6±16.5	0.606±0.60
0.1w% gold	0.849±1.0	0.307±0.72	6.15±14.4	0.302±0.71
	with bilateral filter			
0.7w% gold	4.54±1.0	4.19±0.99	83.8±19.8	0.891±0.21
0.4w% gold	4.00±1.0	3.46±0.96	69.2±19.2	0.817±0.23
0.3w% gold	2.98±1.0	2.42±0.97	48.4±19.3	0.746±0.30
0.2w% gold	3.00±1.0	1.20±0.92	39.9±18.4	0.604±0.28
0.1w% gold	2.04±1.0	0.767±0.68	15.3±13.6	0.311±0.27
	with density filter			
0.7w% gold	3.65±1.0	3.32±0.99	66.4±19.9	0.924±0.28
0.4w% gold	2.76±1.0	2.42±0.94	48.4±18.8	0.890±0.35
0.3w% gold	1.92±1.0	1.57±0.91	31.4±18.3	0.819±0.48
0.2w% gold	1.90±1.0	1.39±0.87	27.8±17.4	0.730±0.46
0.1w% gold	1.05±1.0	0.523±0.72	10.5±14.5	0.456±0.63

Table 4.14: Performance results of the least-squares parameter estimation for the optimized gold images of the human voxel phantom.

	SNR	CNR	CNR_{eff}	C
	unfiltered			
0.3w% gold	1.15±1.0	0.853±0.85	7.96±8.02	0.691±.069
0.2w% gold	0.878±1.0	0.524±0.82	4.99±7.71	0.519±0.82
	with bilateral filter			
0.3w% gold	3.54±1.0	2.62±0.95	24.4±8.95	0.709±0.26
0.2w% gold	2.68±1.0	1.67±0.96	15.8±9.05	0.557±0.32
	with density filter			
0.3w% gold	2.00±1.0	1.66±0.91	15.2±8.62	0.849±0.47
0.2w% gold	1.26±1.0	0.964±0.87	8.77±8.27	0.740±0.69

The numerical values in the gold images of the least-squares parameter estimation represent the concentration of gold in the tissue; the results are summarized in Table 4.15. The algorithm underestimates the concentration of gold on average by 44% for all ROIs and both phantoms. The bilateral filter leads to a higher noise reduction (on average 59%)

than the density filter (on average 22%), but the density filter improves the estimated gold concentration. Further investigations about the ability to estimate the gold concentration are summarized in the annex. The calculated concentrations there only slightly underestimate the gold concentration. It was already outlined in Section 4.1.4.1 (Figure 4.23 and Table 4.9), that the linear attenuation values in the reconstructed images differ from the XCOM values. These differences could be the reason for the underestimation of the gold concentrations.

Table 4.15: Implemented and by the least-squares parameter estimation calculated concentrations of gold in w%.

	implemented	unfiltered	with bilateral filter	with density filter
	0.7w% gold	0.31±0.15	0.31±0.08	0.34±0.11
simple	0.4w% gold	0.18±0.11	0.17±0.05	0.20±0.08
voxel	0.3w% gold	0.14±0.11	0.13±0.05	0.15±0.09
phantom	0.2w% gold	0.12±0.10	0.11±0.04	0.14±0.07
	0.1w% gold	0.056±0.07	0.056±0.03	0.059±0.06
human				
voxel	0.3w% gold	0.15±0.14	0.13±0.04	0.18±0.11
phantom	0.2w% gold	0.095±0.12	0.088±0.04	0.11±0.10

To my knowledge the least-squares parameter estimation algorithm was hardly applied to spectral CT till now. Least-squares parameter calculations of CT simulations of a breast phantom provided good separation and quantification of hydroxyapatite, iodine, glandular, and adipose tissues [68].

4.1.5 Conclusion

In this section the above presented results will be compared and summarized. For all simulations the total number of views was equal to 1160 and the number of histories per view was 10^9. A liver-spleen scan (scan-length approximately 18.4 cm, yielding 210 rotations) with that number of photons would lead to an effective dose of 13.0 mSv, which is approximately the same as for a real liver-spleen scan. The presented images should therefore be comparable to clinical CT images.

The obtained gold images of the eigenvector decomposition, the K-edge decomposition and the least-squares parameter estimation can be filtered with the bilateral filter (section 3.1.1.2) to decrease the high noise level in the gold images (refereed to as K-edge+bifilt, EV+bifilt and LSPE+bifilt). The reconstructed images of the individual bins have a rather high noise level. It might therefore be beneficial to filter these images prior to further processing. Again the bilateral filter is used to filter the reconstructed images of each bin. The density images generated by the least-squares parameter estimation can be filtered with the bilateral filter or the density filter (section 3.1.4.3), refereed to as LSPE+bifilt

or LSPE+density.

The results of the thus processed images for the simple voxel phantom and the human voxel phantom are shown in Figure 4.30, Figure 4.31 and Figure 4.32. Distinct differences of the different algorithms and filters are demonstrated in the close-ups.

All unfiltered images of the simple voxel phantom have a high noise level, which decreased after the application of the bilateral filter (Figure 4.30(b), (d), (f) and (i)). For the least-squares parameter estimation the density filter provides better results than the bilateral filter (Figure 4.30(f) and (g)). Filtering the reconstructed images prior to the least-squares parameter estimation produces better results than without that filtering (Figure 4.30(h), (i) and (j)). The biggest metastasis with 0.1w% gold is faintly visible in all subfigures. The smaller metastases with 0.1w% gold are barely identifiable. The smallest metastases with 0.2w% gold can not be distinguished from noise in all close-ups. The remaining metastases are detectable in all images.

For the human voxel phantom the different algorithms/filters give similar results (Figure 4.31 and 4.32) as for the simple voxel phantom. In the human voxel phantom with 0.3w% gold, all three metastases can be clearly identified in the filtered images (Figure 4.31(b), (d), (f), (g), (h), (i) and (j)). Even the smallest metastasis with a size of only $0.35 \times 0.35\,\mathrm{cm}^2$, is clearly recognizable. Figure 4.31(j) has the lowest background noise. The square shape of the metastases is well reproduced by all filtered images.

In the human voxel phantom with 0.2w% gold, the smallest metastasis is faintly visible in all images, but it is hard to distinguish it from background noise. The other two metastases are clearly identifiable especially in the filtered images (Figure 4.32(b), (d), (f), (g), (h), (i) and (j)). The least-squares parameter estimation in combination with the bilateral and density filter provides the lowest background noise and the square shape of the metastases is reproduced best (Figure 4.32(j)).

The above presented results are evaluated with respect to the SNR, the (effective) CNR and the contrast. For the simple voxel phantom only the biggest metastases for each gold concentration were selected as ROIs. For the human voxel phantom the SNR, (effective) CNR and the contrast was calculated for all three metastases individually and then the mean was calculated. Results are summarized in Tables 4.16, 4.17 and Figure 4.33. The gold images are very noisy, a higher number of simulated incident photons might overcome this problem. However, as already described, the effective dose is in the same range as for a real liver-spleen scan. The simulation results and the evaluation of the SNR, (effective) CNR and the contrast should provide a reasonable approximation.

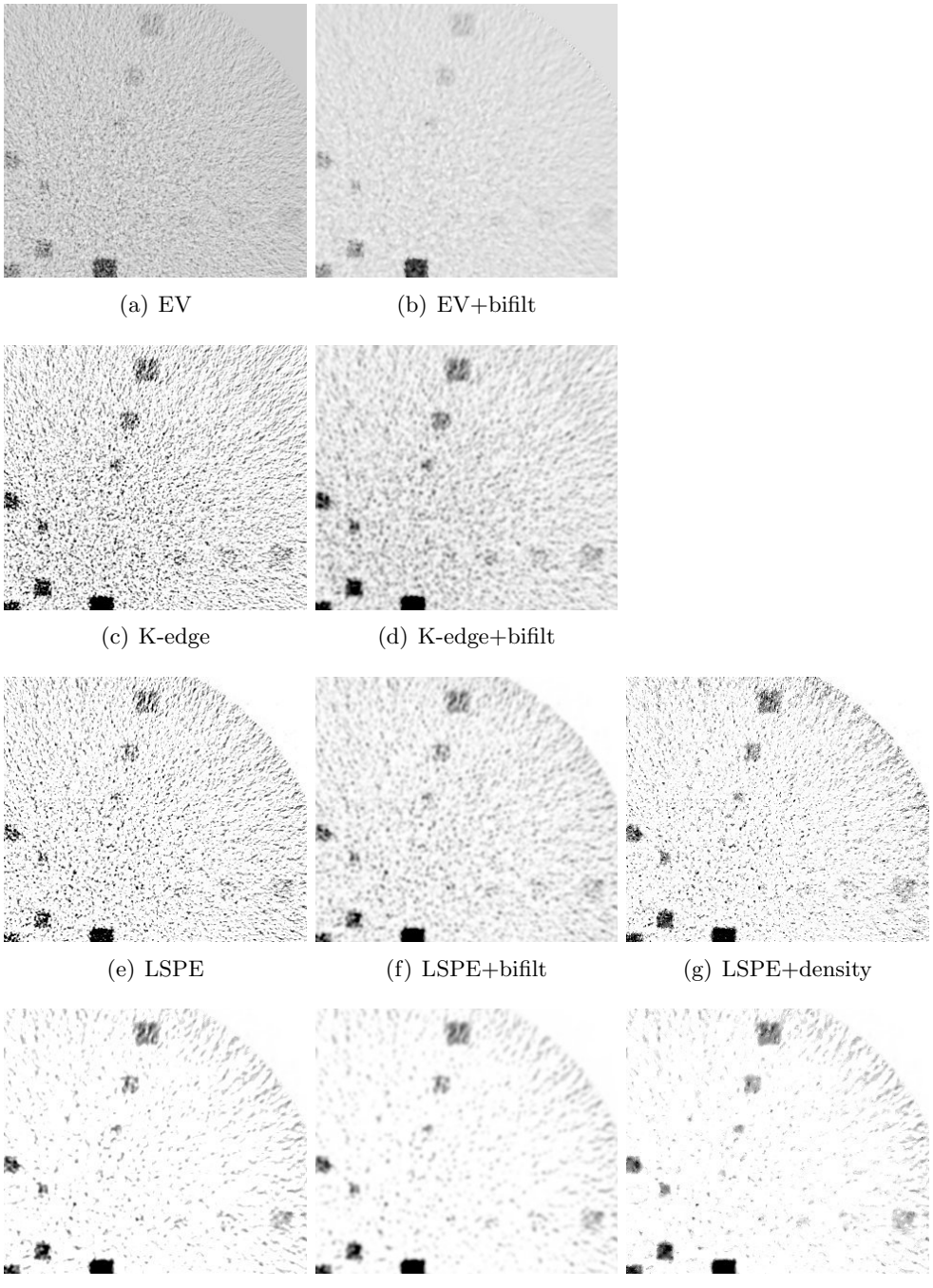

(a) EV (b) EV+bifilt

(c) K-edge (d) K-edge+bifilt

(e) LSPE (f) LSPE+bifilt (g) LSPE+density

(h) bifilt+LSPE (i) bifilt+LSPE+bifilt (j) bifilt+LSPE+density

Figure 4.30: Close-ups of the optimized simple voxel phantom. In order to better illustrate the differences in the algorithm results, the negative of the images is shown (all K-edge and LSPE images are equally scaled). LSPE - least-squares parameter estimation, density - density filter, bifilt - bilateral filter, EV - eigenvector decomposition, + - indicates successive application of the algorithm/filter

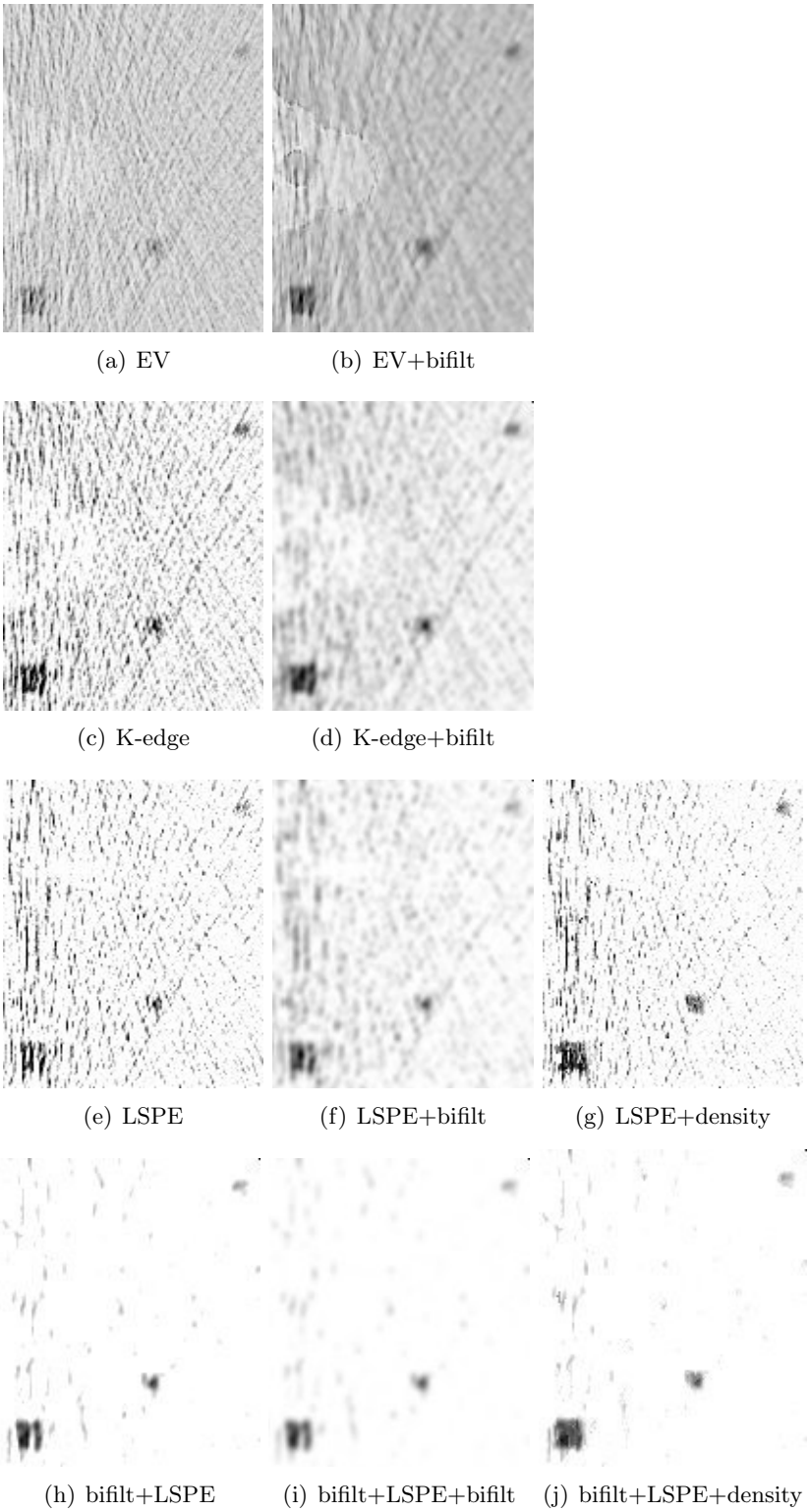

(a) EV (b) EV+bifilt

(c) K-edge (d) K-edge+bifilt

(e) LSPE (f) LSPE+bifilt (g) LSPE+density

(h) bifilt+LSPE (i) bifilt+LSPE+bifilt (j) bifilt+LSPE+density

Figure 4.31: Noise reduced close-ups of the optimized human voxel phantom with 0.3w% gold. In order to better illustrate the differences in the algorithm results, the negative of the images is shown (all K-edge and LSPE images are equally scaled). LSPE - least-squares parameter estimation, density - density filter, bifilt - bilateral filter, EV - eigenvector decomposition, + - indicates successive application of the algorithm/filter

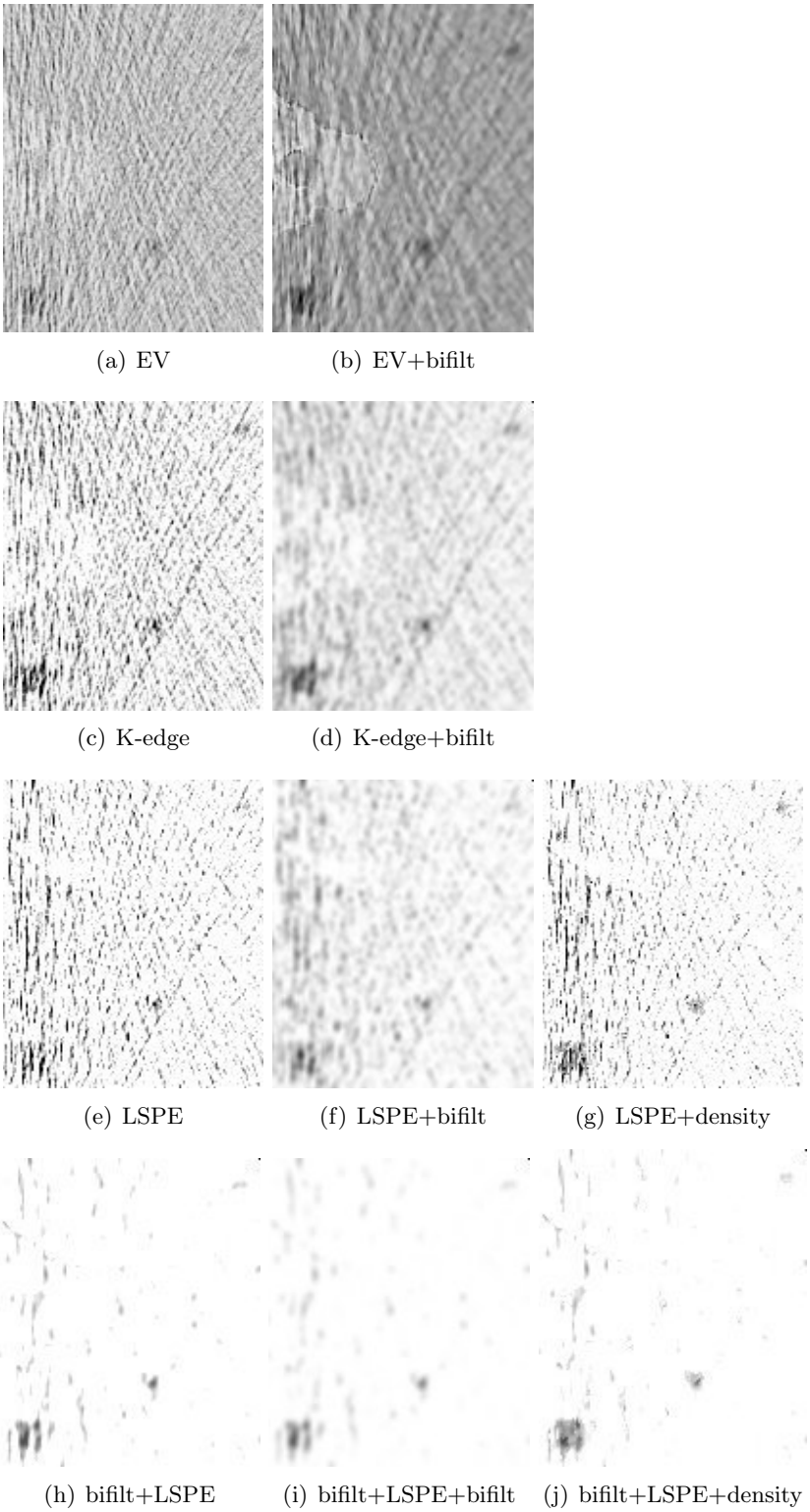

(a) EV (b) EV+bifilt

(c) K-edge (d) K-edge+bifilt

(e) LSPE (f) LSPE+bifilt (g) LSPE+density

(h) bifilt+LSPE (i) bifilt+LSPE+bifilt (j) bifilt+LSPE+density

Figure 4.32: Noise reduced close-ups of the optimized human voxel phantom with 0.2w% gold. In order to better illustrate the differences in the algorithm results, the negative of the images is shown (all K-edge and LSPE images are equally scaled). LSPE - least-squares parameter estimation, density - density filter, bifilt - bilateral filter, EV - eigenvector decomposition, + - indicates successive application of the algorithm/filter

For the 0.4w%, 0.3w%, 0.2w% and the 0.1w% gold the SNR is markedly highest for the eigenvector decomposition in combination with bilateral filtering (EV+bifilt), but the contrast is very low. In the simple voxel phantom the SNR for the unfiltered and filtered gold image is markedly higher than for the other algorithms. Considering only the K-edge decomposition and the least-squares parameter estimation, the highest SNR is attained by the K-edge decomposition in combination with the bilateral filter (K-edge+bifilt). The (effective) CNR and the contrast are also high. The least-squares parameter estimation in combination with the bilateral and density filter (bifilt+LSPE+density/bifilt) reveal the highest contrast and the SNR is only about 10% smaller than for the K-edge algorithm in combination with the bilateral filter. For the calculation of the SNR, the background is not taken into account. To be able to precisely identify the metastases a high contrast and low noise is needed. Therefore the (effective) CNR and the contrast are of main interest to us. The least-squares parameter estimation with all filter combinations provides a higher contrast than the K-edge or the eigenvector decomposition. The highest contrast for all metastases is attained with the least-squares parameter estimation in combination with the bilateral and the density filter (bifilt+LSPE+density). The highest (effective) CNR is obtained with the least-squares parameter estimation in combination with the bilateral and the density filter (bifilt+LSPE+density) or the bilateral filter (bifilt+LSPE+bifilt). As can be seen in Figure 4.30, the biggest metastases with 0.1w% gold is faintly visible in all images. The effective CNR is higher than 5 for all cases, however, taking into account the standard deviation of the effective CNR for the biggest metastasis with 0.1w% gold, a clear distinction between background and ROI is only possible for the filtered eigenvector decomposition (EV+bifilt), the filtered K-edge decomposition (K-edge+bifilt) and the least-squares parameter estimation in combination with the bilateral and the density filter (bifilt+LSPE+bifilt, bifilt+LSPE+density). Comparing the biggest metastases with 0.2w% gold and with 0.1w% gold reveals a reduction of the (effective) CNR and the SNR of approximately 50% and also the contrast decreases by more than 10%.
The results for the human voxel phantom (Table 4.17) are very similar to the ones for the simple voxel phantom. The highest SNR is attained for the filtered gold image of the eigenvector decomposition. The least-squares parameter estimation in combination with the bilateral and the density filter (bifilt+LSPE+density) provide the highest (effective) CNR and the highest contrast for the human voxel phantom with 0.3w% gold. For the human voxel phantom with 0.2w% gold, the highest contrast and the second highest (effective) CNR is achieved with the least-squares parameter estimation in combination with the bilateral and the density filter (bifilt+LSPE+density). The K-edge decomposition in combination with the bilateral filter (K-edge+bifilt) provides the highest (effective) CNR, but the contrast is almost 60% smaller than for the least-squares parameter estimation in combination with the bilateral and the density filter (bifilt+LSPE+density).

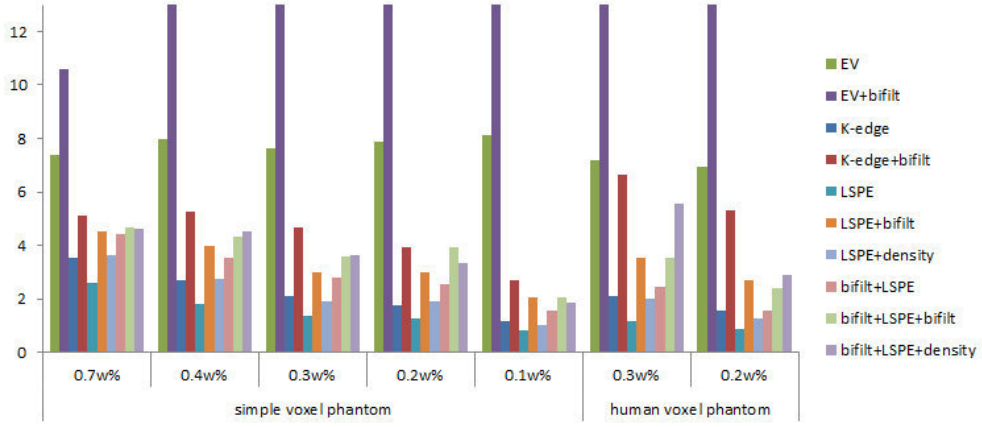

(a) SNR

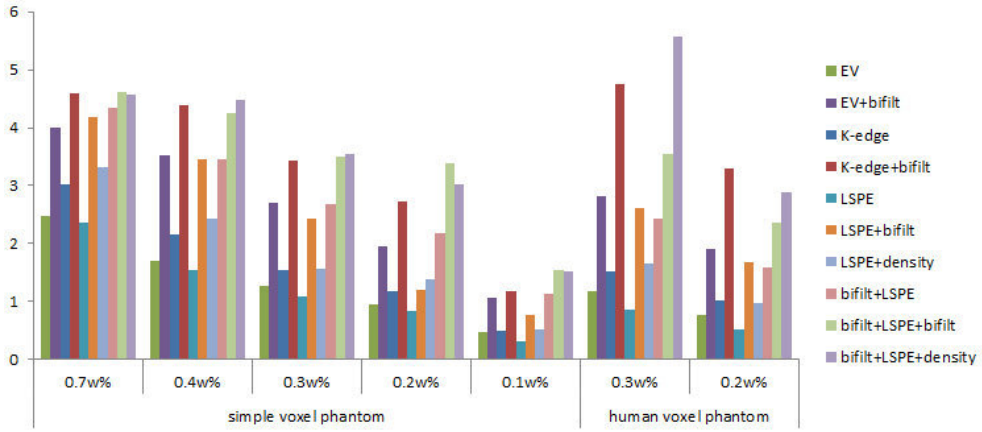

(b) CNR

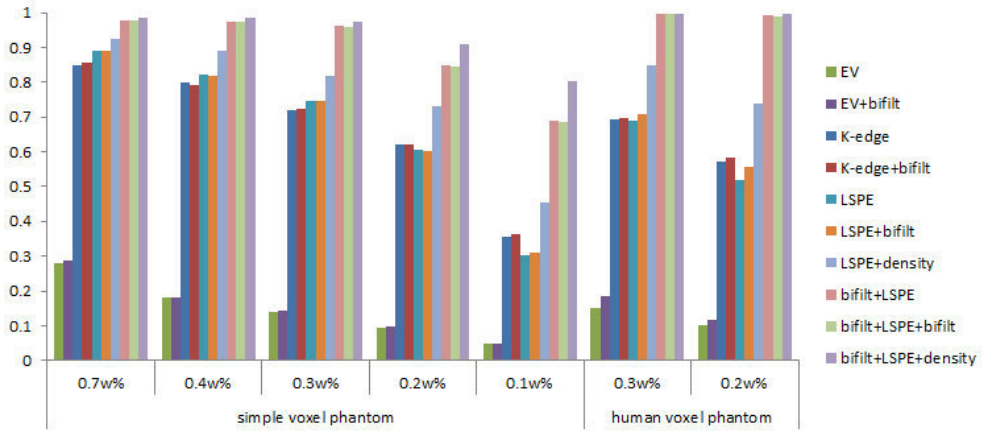

(c) contrast

Figure 4.33: Comparing the performance of the different algorithms.

Table 4.16: Comparing the performance of the different algorithms for the simple voxel phantom.

	simple voxel phantom							
	0.7w% gold				0.4w% gold			
	SNR	CNR	CNR_{eff}	C	SNR	CNR	CNR_{eff}	C
EV	7.39±1.0	2.47±1.03	49.5±20.6	0.279±0.12	7.95±1.0	1.71±0.89	34.1±17.7	0.181±0.094
EV+bifilt	**10.6**±1.0	4.00±0.99	80.1±19.8	0.288±0.071	**15.0**±1.0	3.52±0.88	70.3±17.5	0.183±0.046
K-edge	3.54±1.0	3.03±1.02	60.7±20.4	0.859±0.29	2.69±1.0	2.16±0.96	43.2±19.2	0.799±0.36
K-edge+bifilt	5.11±1.0	4.60±0.98	92.0±19.5	0.857±0.18	5.25±1.0	4.39±1.00	87.9±20.1	0.792±0.18
LSPE	2.62±1.0	2.36±1.0	47.2±20.0	0.889±0.38	1.83±1.0	1.54±0.92	30.8±18.5	0.822±0.49
LSPE+bifilt	4.54±1.0	4.19±0.99	83.8±19.8	0.891±0.21	4.00±1.0	3.46±0.96	69.2±19.2	0.817±0.23
LSPE+density	3.65±1.0	3.32±0.99	66.4±19.9	0.924±0.28	2.76±1.0	2.42±0.94	48.4±18.8	0.890±0.35
bifilt+LSPE	4.44±1.0	4.34±0.99	83.8±19.8	0.977±0.22	3.55±1.0	3.45±0.97	69.2±19.2	0.975±0.27
bifilt+LSPE+bifilt	4.68±1.0	**4.61**±0.99	**92.3**±19.8	0.978±0.21	4.35±1.0	4.25±0.97	84.9±19.4	0.974±0.22
bifilt+LSPE+density	4.64±1.0	4.56±0.98	91.3±19.6	**0.984**±0.21	4.55±1.0	**4.48**±0.98	**89.6**±19.6	**0.987**±0.22
	0.3w% gold				0.2w% gold			
	SNR	CNR	CNR_{eff}	C	SNR	CNR	CNR_{eff}	C
EV	7.62±1.0	1.27±0.88	25.4±17.6	0.138±0.096	7.87±1.0	0.945±0.80	18.9±16.1	0.0930±0.079
EV+bifilt	**14.8**±1.0	2.70±0.99	54.1±19.9	0.144±0.053	**16.1**±1.0	1.96±0.96	39.1±19.1	0.0961±0.047
K-edge	2.09±1.0	1.55±0.89	31.1±17.9	0.720±0.41	1.77±1.0	1.18±0.86	23.6±17.2	0.621±0.45
K-edge+bifilt	4.68±1.0	3.43±0.98	68.6±19.6	0.722±0.21	3.95±1.0	2.72±0.95	54.3±19.0	0.623±0.22
LSPE	1.37±1.0	1.08±0.89	21.6±17.8	0.747±0.61	1.26±1.0	0.832±0.82	16.6±16.5	0.606±0.60
LSPE+bifilt	2.98±1.0	2.42±0.97	48.4±19.3	0.746±0.30	3.00±1.0	1.20±0.92	39.9±18.4	0.604±0.28
LSPE+density	1.92±1.0	1.57±0.91	31.4±18.3	0.819±0.48	1.90±1.0	1.39±0.87	27.8±17.4	0.730±0.46
bifilt+LSPE	2.78±1.0	2.68±0.98	48.4±19.3	0.962±0.35	2.57±1.0	2.19±0.94	39.9±18.4	0.847±0.37
bifilt+LSPE+bifilt	3.60±1.0	3.50±0.99	70.0±19.7	0.960±0.27	3.95±1.0	**3.39**±0.93	**67.7**±18.6	0.845±0.23
bifilt+LSPE+density	3.66±1.0	**3.55**±1.00	**71.0**±20.0	**0.974**±0.27	3.32±1.0	3.02±0.98	60.4±19.7	**0.910**±0.30

	0.1w% gold			
	SNR	CNR	CNR_{eff}	C
EV	8.11±1.0	0.480±0.65	9.60±13.0	0.0469±0.064
EV+bifilt	**18.9**±1.0	1.07±0.72	21.3±14.3	0.0496±0.033
K-edge	1.17±1.0	0.487±0.69	9.75±13.9	0.355±0.50
K-edge+bifilt	2.69±1.0	1.19± 0.81	23.8±16.1	0.365±0.25
LSPE	0.849±1.0	0.307±0.72	6.15±14.4	0.302±0.71
LSPE+bifilt	2.04±1.0	0.767±0.68	15.3±13.6	0.311±0.27
LSPE+density	1.05±1.0	0.523±0.72	10.5±14.5	0.456±0.63
bifilt+LSPE	1.58±1.0	1.13±0.82	15.3±13.6	0.689±0.50
bifilt+LSPE+bifilt	2.07±1.0	**1.54**±0.90	**30.8**±17.9	0.686±0.40
bifilt+LSPE+density	1.85±1.0	1.53±0.87	30.6±17.4	**0.804**±0.46

Table 4.17: Comparing the performance of the different algorithms for the human voxel phantom.

	human voxel phantom, 0.3w% gold				human voxel phantom, 0.2w% gold			
	SNR	CNR	CNR_{eff}	C	SNR	CNR	CNR_{eff}	C
EV	7.19±1.0	1.17±0.78	10.6±6.97	0.151±0.10	6.94±1.0	0.765±0.68	7.05±6.21	0.102±0.090
EV+bifilt	**14.0**±1.0	2.82±0.82	24.7±7.47	0.183±0.056	**14.9**±1.0	1.90±0.78	16.7±6.96	0.115±0.049
K-edge	2.10±1.0	1.52±0.95	13.5±8.63	0.692±0.46	1.59±1.0	1.01±0.88	9.44±8.10	0.573±0.50
K-edge+bifilt	6.64±1.0	4.76±0.89	43.4±8.18	0.697±0.15	5.31±1.0	**3.29**±1.01	**30.5**±9.33	0.582±0.19
LSPE	1.15±1.0	0.853±0.85	7.96±8.02	0.691±0.69	0.878±1.0	0.524±0.82	4.99±7.71	0.519±0.82
LSPE+bifilt	3.54±1.0	2.62±0.95	24.4±8.95	0.709±0.26	2.68±1.0	1.67±0.96	15.8±9.05	0.557±0.32
LSPE+density	2.00±1.0	1.66±0.91	15.2±8.62	0.849±0.47	1.26±1.0	0.964±0.87	8.77±8.27	0.740±0.69
bifilt+LSPE	2.44±1.0	2.44±1.00	22.3±9.31	0.997±0.42	1.58±1.0	1.58±1.00	15.2±9.35	0.994±0.64
bifilt+LSPE+bifilt	3.56±1.0	3.55±1.00	32.7±9.37	0.995±0.29	2.39±1.0	2.37±1.01	22.5±9.42	0.988±0.43
bifilt+LSPE+density	5.57±1.0	**5.56**±1.00	**55.7**±9.36	**0.998**±0.21	2.89±1.0	2.89±1.00	28.6±9.36	**0.998**±0.38

Table 4.18: Implemented and calculated concentrations of gold in w%. The values for the eigenvector decomposition and the K-edge decomposition are corrected with the total density.

	simple voxel phantom				
implemented	0.7w%	0.4w%	0.3w%	0.2w%	0.1w%
EV	0.43±0.16	0.25±0.12	0.19±0.11	0.13±0.10	0.064±0.09
EV+bifilt	0.42±0.11	0.25±0.06	0.18±0.06	0.13±0.05	0.064±0.04
K-edge	0.45±0.15	0.26±0.10	0.19±0.10	0.13±0.08	0.065±0.06
K-edge+bifilt	0.44±0.10	0.25±0.05	0.19±0.04	0.13±0.03	0.066±0.03
LSPE	0.31±0.15	0.18±0.11	0.14±0.11	0.12±0.10	0.056±0.07
LSPE+bifilt	0.31±0.08	0.17±0.05	0.13±0.05	0.11±0.04	0.056±0.03
LSPE+density	0.34±0.11	0.20±0.08	0.15±0.09	0.14±0.07	0.059±0.06
bifilt+LSPE	0.32±0.08	0.19±0.06	0.14±0.06	0.12±0.05	0.058±0.04
bifilt+LSPE+bifilt	0.31±0.08	0.18±0.05	0.14±0.04	0.12±0.03	0.057±0.03
bifilt+LSPE+density	0.33±0.08	0.19±0.05	0.15±0.04	0.13±0.04	0.059±0.03

	human voxel phantom	
implemented	0.3w%	0.2w%
EV	0.20±0.14	0.13±0.14
EV+bifilt	0.19±0.06	0.12±0.06
K-edge	0.20±0.11	0.11±0.10
K-edge+bifilt	0.19±0.03	0.13±0.03
LSPE	0.15±0.14	0.095±0.12
LSPE+bifilt	0.13±0.04	0.088±0.04
LSPE+density	0.18±0.11	0.11±0.10
bifilt+LSPE	0.13±0.06	0.078±0.05
bifilt+LSPE+bifilt	0.12±0.04	0.072±0.03
bifilt+LSPE+density	0.15±0.03	0.086±0.03

The numerical values in the gold images of the three different algorithms represent the fractional weight of gold in the tissue. The values are summarized in Table 4.18. All algorithms underestimate the concentration of gold for all ROIs and both phantoms. The reason for the underestimation for the K-edge decomposition was already outlined in 4.1.4.2 (Equation 4.6 and 4.7). The reason for the underestimation of the gold concentration for the eigenvector decomposition and the least-squares parameter estimation could be the differences between the linear attenuation values in the reconstructed images and the XCOM values. The eigenvector decomposition and the K-edge decomposition provide slightly better results than the least-squares parameter estimation. The eigenvector decomposition and the least-squares parameter estimation are able to calculate the weight fraction of gold without any prior information. For the K-edge decomposition algorithms the values need to be corrected with the total density, which is generally not known. The total density of soft tissue can be approximated by one, but when gold is in the tissue the total density increases considerably. The error in the total density, which is introduced

by neglecting the gold concentration, is illustrated in Table 4.19. The numerical values in the gold images of the K-edge decomposition could be used to correct the total density.

Table 4.19: Error in the total density, when the gold concentration is neglected.

gold concentration	ρ_{total}	error
0w%	1.0	0%
0.1w%	1.0183	1.83%
0.2w%	1.0366	3.66%
0.3w%	1.0549	5.49%
0.4w%	1.0732	7.32%
0.7w%	1.1281	12.81%

The applied filter algorithms clearly reduce noise, only the density filter slightly improves the estimated gold concentration, for the bilateral filter the predicted concentration of gold remains almost unchanged.
In summary, the best results were achieved by the least-squares parameter estimation in combination with the bilateral and the density filter (bifilt+LSPE+density).
The computing time and the required input and output of the different algorithms and the filters is summarized in Table 4.20 and 4.21. The eigenvector decomposition is very fast and could be used to get a first impression. The performance results of the K-edge decomposition and the least-squares parameter estimation are very promising. All algorithms provide the density of gold in the decomposed images. But the K-edge decomposition has a very long computation time compared to the least-squares parameter estimation. This fact and the high SNR, (effective) CNR and contrast, which were obtained with the least-squares parameter estimation in combination with the bilateral and density filter, make this algorithm with the two filters a very promising candidate for the material-decomposition in spectral CT imaging.

Table 4.20: Comparison of the relative computing time of the different algorithms

	Computing time		Computing time
EV	1	LSPE+density	102
K-edge	1129	bifilt+LSPE	100
K-edge+bifilt	1129	bifilt+LSPE+bifilt	101
LSPE	100	bifilt+LSPE+density	102
LSPE+bifilt	101		

It was already outlined in section 3.1.1.3, that the effective CNR (and taking into account the standard deviation) must be greater than 5 to be able to clearly distinguish the background and the metastases with gold. This Rose criterion is fulfilled by all algorithms (in combination with different filter algorithms) if the gold concentration is at least 0.2w%.

Several factors influence the detectability of gold, e.g. the size of the ROI, the applied decomposition algorithm and the X-ray spectrum. It could furthermore be beneficial to use statistical reconstruction algorithms [99].

Table 4.21: Comparison of the different algorithms

	Specific detection of gold	required input	output
EV	yes	energy dependent mass attenuation coefficients of gold, liver and bone	six noise reduced images of the original images and six basis images, providing information about the covariance and the gold concentration
K-edge	yes	energy dependent mass attenuation coefficients of gold	three images, corresponding to the photoelectric effect, Compton scattering and the gold concentration
LSPE	yes	energy dependent mass attenuation coefficients of gold, liver and bone	three images, corresponding to gold, liver and bone, each image contains the density of the corresponding material
bifilt	/	image	noise reduced image
density	/	material density images and standard CT image and mass attenuation coefficients of gold, liver and bone at the mean energy of the used X-ray spectrum	noise reduced material density images

4.2 Dose enhancement effect - Monte Carlo simulations

4.2.1 Simulation results

The dose enhancement simulations provide information about the secondary electron spectra and about the deposited dose. The used voxel phantom imitated a cell culture flask which can be used for irradiation cell experiments.
Figure 4.34 shows the energy distribution of secondary Compton, photo- and Auger electrons for the 100 kV spectrum and 0.2w% gold in the tissue. The produced Compton electrons have a low energy below 30 keV. The energy of the produced photo-electrons is distributed over the whole spectrum. The energy of the Auger electrons shows no continuous distribution.

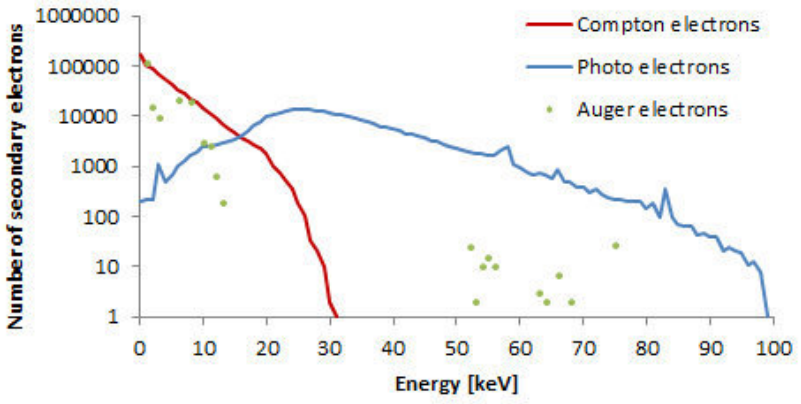

Figure 4.34: Spectrum of secondary electrons for 100 kV and 0.2w% gold.

In Figure 4.35 the number of produced secondary electrons depending on the X-ray tube voltage is plotted. The number of Compton electrons is almost the same for all spectra and for the different concentrations of gold. With increasing X-ray tube voltage the number of produced Compton electrons slightly decreases. The number of produced photo- and Auger electrons decreases with increasing X-ray tube voltage, due to the lower interaction probability. The higher the concentration of gold the more secondary photo- and Auger electrons are generated.
Table 4.22 displays the percentage of the produced Compton, photo- and Auger electrons for different gold concentration and different X-ray spectra. The percentage of Compton electrons increases with increasing X-ray tube voltage, but decreases for increasing concentrations of gold. Photo- and Auger electrons show the opposite behavior. The percentage of produced photo- and Auger electrons decreases with increasing X-ray tube voltage and increases with increasing concentrations of gold. Only for the 60 kV spectrum the percentage of photo-electrons for 0.1 up to 0.3w% gold is smaller than in the metastasis. The reason for this is the high number of Auger electrons.

Figure 4.36 shows the number of produced Auger electrons as a function of energy for different X-ray spectra and 0.1w% gold. First of all, the distribution of Auger electrons is not continuous. It can be seen that most of the produced Auger electrons have a low energy and therefore a short penetration range.
Dose increases almost linearly with the gold concentration (Figure 4.37). The highest dose in tissue is produced by the 60 kV spectrum. As the energy of the spectrum increases, the dose in tissue decreases. This effect is due to the higher interaction probability at lower energies, leading to a higher number of secondary electrons. The dose in the liver is higher than for the metastasis due to the higher density of liver tissue (Figure 4.37).
The dose enhancement factor was calculated according to Eq. 3.40 and is shown in Figure 4.38. The dose enhancement factor is almost independent of the used spectra. The concentration of gold is the main factor influencing the dose enhancement. The maximum dose enhancement factor is 1.95 at 80 kV for 0.1w% gold, 2.89 at 80 kV for 0.2w% gold, 3.84 at 80 kV for 0.3w% gold and 4.98 at 60 kV for 0.4w% gold.

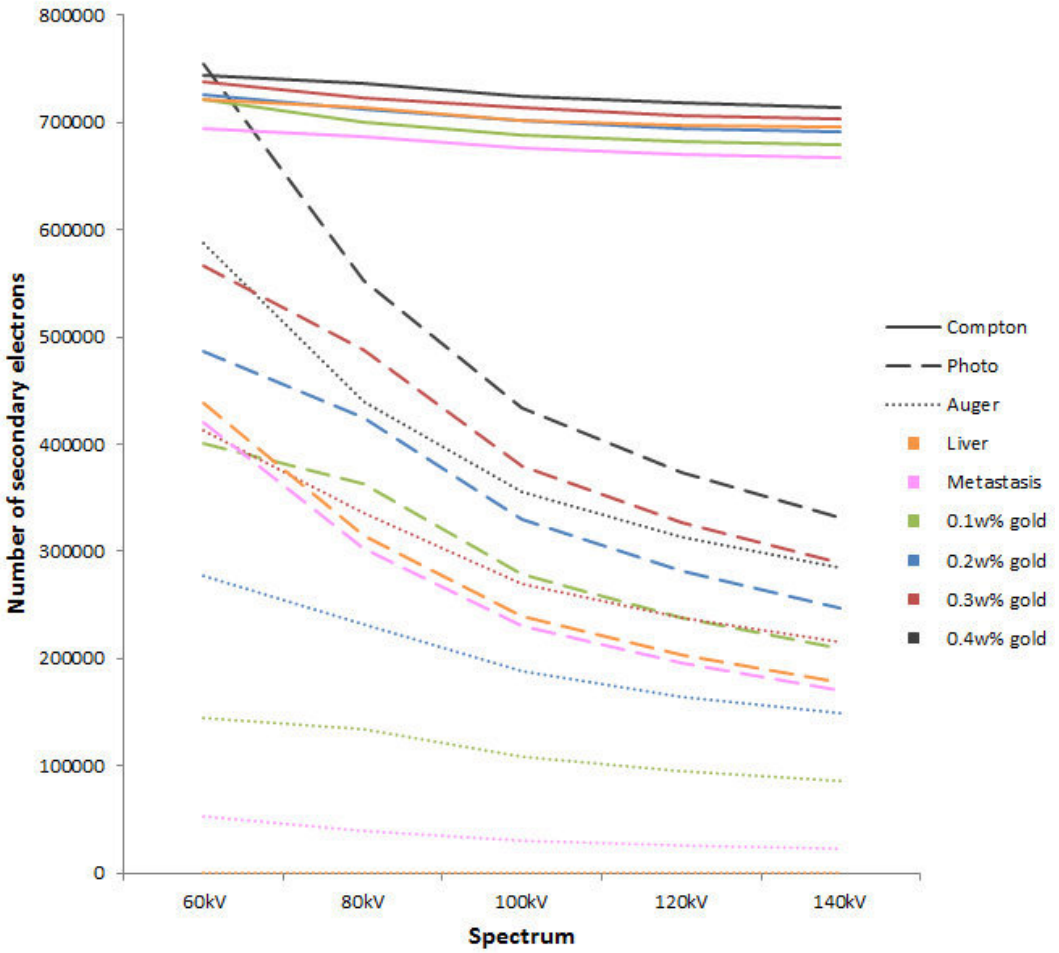

Figure 4.35: Number of secondary Compton, photo- and Auger electrons for different spectra and different concentrations of gold.

Table 4.22: Comparison of the number of produced secondary electrons for different concentrations of gold and different X-ray spectra. The number of secondary electrons in the metastasis was set to 100%.

gold concentration	60 kV	80 kV	100 kV	120 kV	140 kV
	Compton electrons				
Metastasis	59.4%	66.8%	72.2%	75.1%	77.5%
0.1w%	57.0%	58.4%	64.1%	67.2%	69.7%
0.2w%	48.7%	52.0%	57.6%	60.9%	63.5%
0.3w%	43.0%	46.7%	52.5%	55.6%	58.2%
0.4w%	35.7%	42.6%	47.9%	51.1%	53.7%
	photo-electrons				
Metastasis	36.0%	29.4%	24.6%	22.0%	19.8%
0.1w%	31.6%	30.3%	25.9%	23.5%	21.5%
0.2w%	32.7%	31.0%	27.0%	24.7%	22.8%
0.3w%	33.0%	31.6%	27.9%	25.7%	23.9%
0.4w%	36.2%	32.0%	28.6%	26.6%	24.9%
	Auger electrons				
Metastasis	4.6%	3.8%	3.2%	2.9%	2.7%
0.1w%	11.4%	11.3%	10.0%	9.3%	8.8%
0.2w%	18.6%	17.0%	15.4%	14.4%	13.7%
0.3w%	24.0%	21.7%	19.8%	18.7%	17.9%
0.4w%	28.1%	25.4%	23.5%	22.3%	21.4%

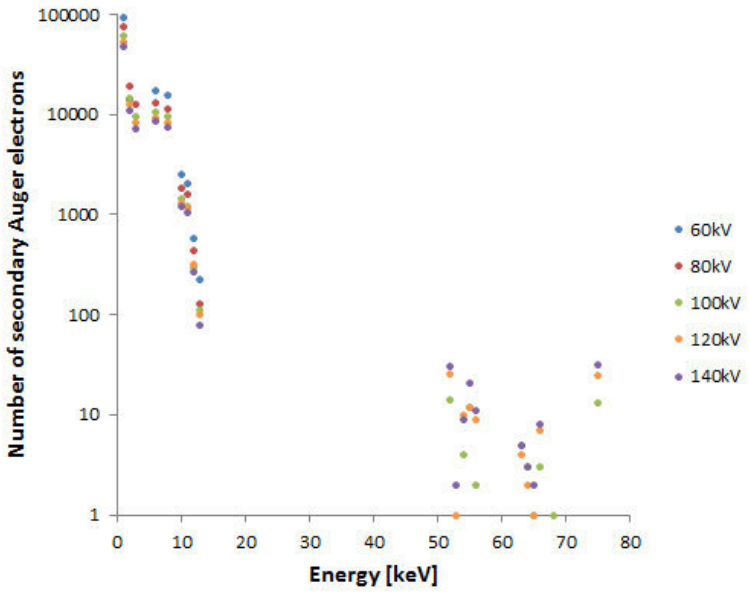

Figure 4.36: Number of Auger electrons for different X-ray spectra and 0.1w% gold.

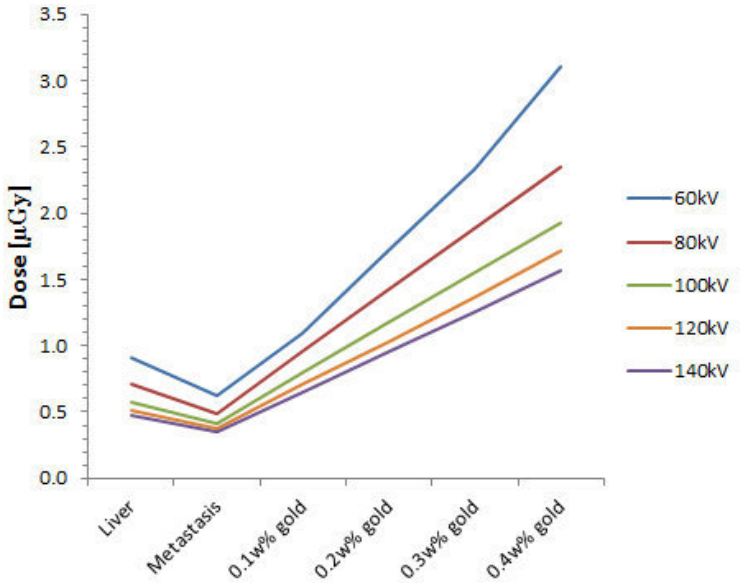

Figure 4.37: Calculated dose in different tissues and for different spectra.

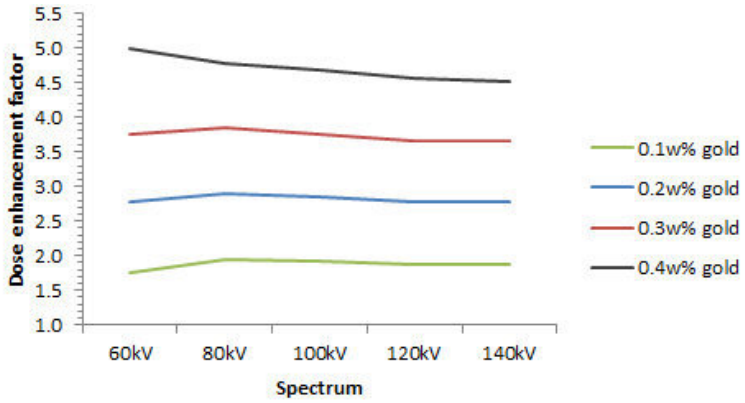

Figure 4.38: Dose enhancement factor for different X-ray spectra and different concentrations of gold.

4.2.2 Conclusion

The simulations indicate that the dose enhancement factor depends mainly on the concentration of gold. The X-ray tube voltage has a minor influence. Low X-ray tube voltages seem to lead to a higher dose enhancement effect. As shown in Figure 4.35, the total number of Compton electrons is much higher than the produced photo- and Auger electrons and is almost the same for all simulations. But the percentage of Compton electrons (Table 4.22) decreases with increasing gold concentration. On the contrary, the percentage of photo- and Auger electrons increases with increasing gold concentration, leading to the conclusion that photo- and Auger electrons induce the dose enhancement effect.
Owing to the fact that most Auger electrons have a very low energy (Figure 4.36), i.e. a

short penetration range, they can get absorbed within the gold-nanoparticles. Lechtman et al. [69] obtained a non-linear correlation between the dose enhancement factor and the gold-nanoparticle radius-cubed, by cause of the self-absorption of Auger electrons. This self-absorption cannot be analyzed with the presented simulations, as a homogeneous distribution of gold was simulated instead of individual gold-nanoparticles. In consequence, the EGSnrc simulations might overestimate the dose enhancement factor.
In the imaging section, the minimum concentration of gold required to provide sufficient contrast in spectral CT imaging, is predicted to be 0.2w% for the used 120 kV X-ray spectrum. The dose enhancement simulations for this X-ray spectrum yield a dose enhancement factor of 2.77 for 0.2w% gold. This dose enhancement effect should not be neglected when using gold-nanoparticles for medical X-ray imaging. Gold-nanoparticles should be functionalized to ensure specific targeting of metastases or other tissues.
The different dose enhancement factors from the literature (Table 2.1) and the here calculated dose enhancement factors are rather difficult to compare, due to the different spectra and the different gold concentrations. The dose enhancement factors by Cho et al. [30] (DEF=2.114 up to 5.601), McMahon et al. [77] (DEF=1.7), Martinez-Rovira et al. [75] (DEF=1.304 up to 1.597) and Lechtman et al. [69] are smaller than the values predicted here. The obtained dose enhancement factor with the novel multicompartment phantom radiochromic radiation dosimeter by Alqathami et al. [5] was 1.77 for a 100 kV spectrum. This result is close to the here presented simulations.

4.3 Internalization of gold-nanoparticles into cells - biological experiments

In the first part of the thesis the concentration of gold required for medical CT imaging was estimated with Monte-Carlo simulations. In the following part biological experiments will be performed to determine the actual concentration of gold which can be specifically conjugated to cells. For the specific targeting of cancer cells the monoclonal antibody cmHsp70.1 was used. This antibody binds to Hsp70, which is only present on the cell membrane of tumor cells.
The main aim of the cell culture experiments was to determine the amount of gold which is internalized by the cells or attached to the cell membrane. On the basis of these results, the question, whether the amount of gold-nanoparticles is sufficient for spectral CT imaging, can be addressed. To be able to specifically target malignant tissues, the tumor specific monoclonal antibody cmHsp70.1 was conjugated to gold-nanoparticles, referred to as gold-cmHsp70.1; as a reference, gold-nanoparticles were coated with BSA, referred to as gold-BSA.

4.3.1 Optimization of antibody concentration for gold-antibody conjugation

To determine the required cmHsp70.1 concentration to stabilize the gold-nanoparticles (15 and 50 nm) a titration series was performed. If the cmHsp70.1 concentration is too low, the gold-solution turns blue, otherwise no color change is visible. The first tube for which no color change is visible, determines the minimum required cmHsp70.1 concentration to stabilize the gold-nanoparticles.

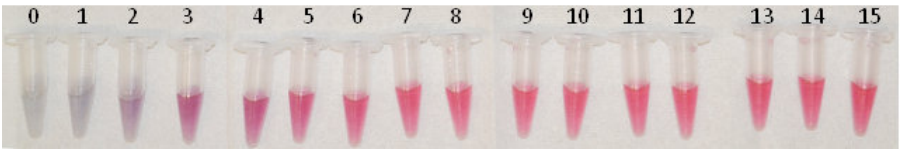

Figure 4.39: Titration series for the gold-nanoparticles with a diameter of 50 nm: The numbers above the tube designate the antibody concentration in µg/ml.

For the tube with 7 µg/ml antibody, no color change in the solution is visible; the required minimum concentration of cmHsp70.1 is therefore 7 µg/ml (Figure 4.39). For the conjugation of the 50 nm gold-nanoparticles and the antibody, the antibody concentration was scaled up to 8 µg/ml in order to ensure a sufficient antibody concentration.
For the 15 nm gold-nanoparticles, the minimum concentration of cmHsp70.1 is 8 µg/ml. The conjugation is done with a concentration of 9 µg/ml.

4.3.2 Conjugation of gold-nanoparticles and antibody

To verify the conjugation of the cmHsp70.1 antibody and the gold-nanoparticles, a dot blot with the 50 nm gold-nanoparticles was performed. After the conjugation of cmHsp70.1 and gold-nanoparticles, different BSA amounts (final concentrations in the solution: 0.25%, 0.5%, 1%) were added. In this way, remaining free surface areas on the gold-nanoparticles were covered with BSA.

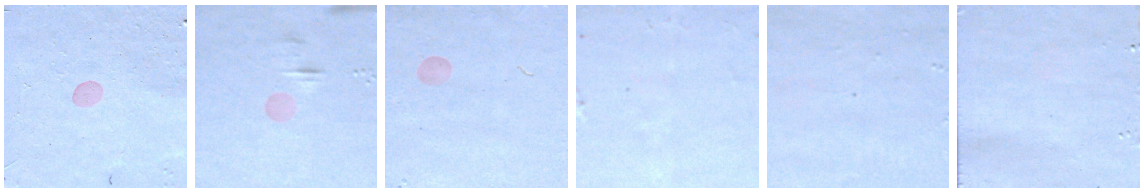

(a) Hsp70 with gold-cmHsp70.1 and 0.25%BSA | (b) Hsp70 with gold-cmHsp70.1 and 0.5%BSA | (c) Hsp70 with gold-cmHsp70.1 and 1%BSA | (d) Hsc70 with gold-cmHsp70.1 and 0.25%BSA | (e) Hsc70 with gold-cmHsp70.1 and 0.5%BSA | (f) Hsc70 with gold-cmHsp70.1 and 1%BSA

Figure 4.40: Dot blot with 50 nm gold-nanoparticles and the cmHsp70.1 antibody.

The red spots in Figure 4.40 are due to the red color of the gold-nanoparticles. As shown in Figure 4.40(a), (b) and (c) the gold-cmHsp70.1 bound to the Hsp70 protein on the membrane, but not to the similar Hsc70 protein (Figure 4.40(d), (e) and (f)). The different amounts of BSA do not seem to have a big impact on the conjugation. For the following experiments, 1% BSA was used. The results of this dot blot indicate that the gold-nanoparticles were successfully conjugated to the cmHsp70.1 antibody.

4.3.3 Verification of gold-antibody conjugation with UV-visible spectroscopy

UV-visible spectroscopic measurements were performed to verify the conjugation of gold-nanoparticles (50 nm) and antibody, respectively BSA. To do this the wavelength and intensity of the absorption of UV-visible radiation was measured for the gold-solution, gold-BSA and gold-cmHsp70.1. The differences in wavelength and intensity between the three substances indicate the presence of different proteins on the surface of the gold-nanoparticles [83].
The results are shown in Figure 4.41. UV-visible spectra of the gold-solution showed peak absorbance at 530 nm. The peak absorbance for gold-BSA was at 533 nm and for gold-cmHsp70.1 at 534 nm, indicating the presence of proteins on the surface of the gold-nanoparticles. The maxima were also calculated with a forth order polynomial fit, which revealed a peak absorbance at 530.12 nm for the gold-solution, 533.12 nm for gold-BSA and 533.94 nm for gold-cmHsp70.1. The gold-cmHsp70.1 spectra was slightly shifted to the right compared with gold-BSA. This slight shift of the absorbance spectra indicates

the presence of different proteins on gold-BSA and gold-cmHsp70.1. These results and the results of the dot blot lead to the conclusion, that the cmHsp70.1 antibody was successfully conjugated to the gold-nanoparticles.

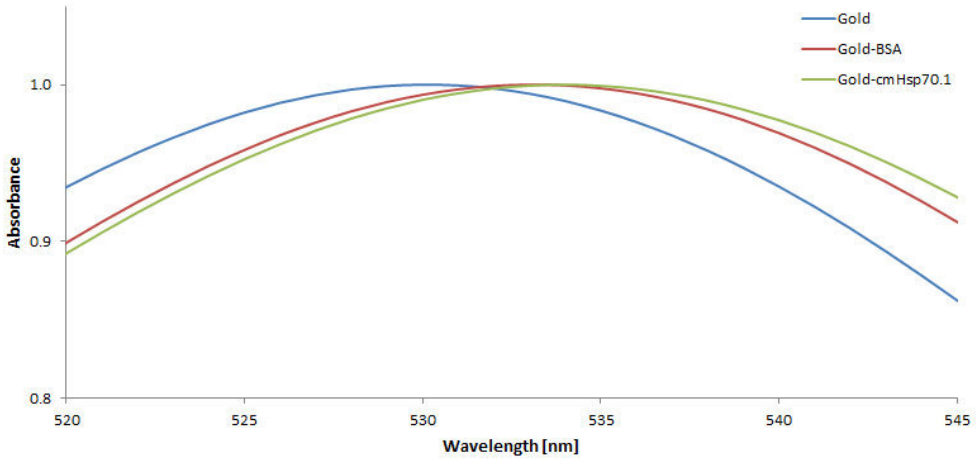

Figure 4.41: UV-visible spectra of gold-solution (blue line), gold-BSA (red line) and gold-cmHsp70.1 (green line). The gold-nanoparticles had a diameter of 50 nm.

4.3.4 Determination of the amount of gold per cell with ICP-OES

The amount of gold (15 and 50 nm) internalized into the cell or attached to the cell membrane was measured with inductively coupled plasma optical emission spectrometry (ICP-OES). In order to ensure the ICP-OES measurements the gold-solution (without any cells) was measured first. The obtained measurements of the gold-solution were in good agreement with the gold amount named by BBI Solutions [1]. The internalized amount of gold-cmHsp70.1 and gold-BSA is summarized in Table 4.23 and Figure 4.42. The 15 and 50 nm gold-BSA show a higher uptake at all time points than the gold-cmHsp70.1. The antibody does therefore not lead to a higher amount of the gold-nanoparticles per cell. The reason for that is not obvious, the number of binding sites at the cell membrane for BSA might be higher than those for cmHsp70.1. Smaller gold-nanoparticles conjugated to cmHsp70.1 improve the uptake of gold-nanoparticles. Incubating the cells with gold-cmHsp70.1, respectively gold-BSA for 12 hours yields the highest uptake. The underlying cause for the low number of gold-nanoparticles per cell in the samples is uncertain. The experiments were repeated but the results were similar.

As already mentioned in section 3.3.2, the conjugation of antibodies and gold-nanoparticles is based on electrostatic interactions. As Kumar et al. [67] pointed out this method has several drawbacks. First of all, the conjugated antibodies have a random orientation, but the correct orientation is essential for appropriate targeting. Secondly, due to the noncovalent binding of the antibodies to the gold-nanoparticles other biological molecules can replace

the conjugated antibodies. Furthermore, a rather high concentration of antibodies is required. One important issue influencing the interaction between gold-nanoparticles and the cells is the protein layer around the gold-nanoparticles. Uncoated gold-nanoparticles interact with serum proteins[27] leading to an adhesion of serum proteins (i.e. a variety of different proteins) to the nanoparticle surface. Gold-nanoparticles coated with serum proteins can bind to a number of different receptors, whereas gold-nanoparticles coated with one specific protein can only bind to the corresponding receptor (i.e. limited number of protein specific receptors) [28]. These factors might explain the low amounts of gold in each cell.

Table 4.23: Cellular uptake of gold-BSA and gold-cmHsp70.1, after 6, 12 and 24h of incubation (in gold-nanoparticles per cell).

incubation time	6h	12h	24h
	gold-nanoparticles 50 nm		
gold-cmHsp70.1	48±4.8	66±6.5	61±0.6
gold-BSA	66±19.4	90±7.4	65±8.1
	gold-nanoparticles 15 nm		
gold-cmHsp70.1	$4.4\times10^3\pm670$	$7.7\times10^3\pm690$	$29\times10^3\pm7940$
gold-BSA	$5.3\times10^3\pm280$	$21\times10^3\pm2300$	$70\times10^3\pm5840$

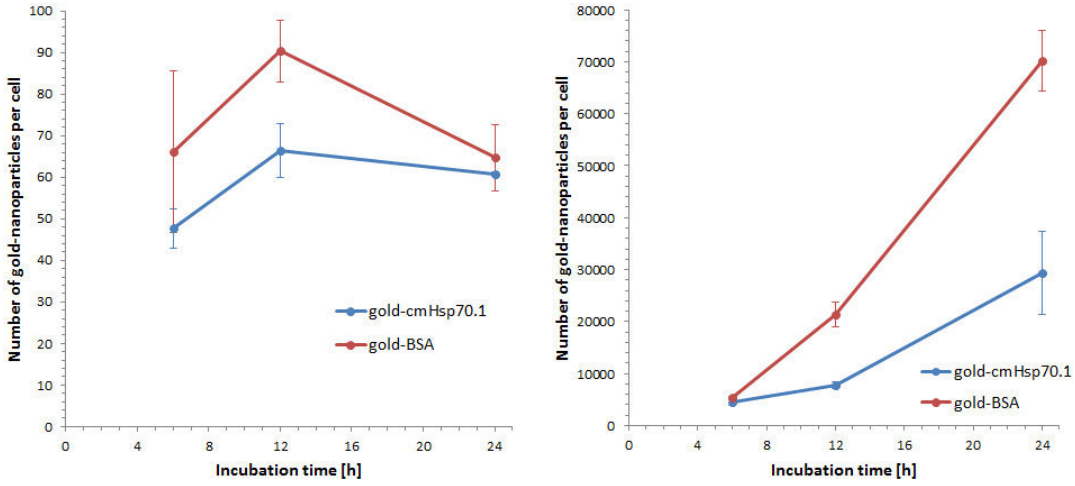

(a) Cellular uptake of 50 nm gold-nanoparticles (b) Cellular uptake of 15 nm gold-nanoparticles

Figure 4.42: Cellular uptake of gold-BSA and gold-cmHsp70.1, after 6, 12 and 24h of incubation.

Experiments done by several groups have observed a much higher uptake of gold-nanoparticles per cell (Table 4.24). The cellular uptake of uncoated gold-nanoparticles (i.e.

[27] Serum proteins are albumin, α1-globuline, α2-globuline, β-globuline and γ-globuline.

nanoparticles get coated with serum protein after being added to the cell culture medium/into blood) was higher than the uptake of gold-nanoparticles coated with other proteins (e.g. antibodies, bovine serum albumin, epidermal growth factor).

Table 4.24: Summary of ICP-OES gold amount measurements in the literature.

	Nanoparticle characterization	Cell type	uptake [NP/cell]
1.	14 nm, uncoated [26]	Hela	3000
2.	50 nm, uncoated [26]	Hela	6160
3.	74 nm, uncoated [26]	Hela	2988
4.	50 nm, uncoated [27]	MCF-7	≈7500[28]
5.	50 nm, coated with BSA [27]	MCF-7	≈4100[28]
6.	50 nm, uncoated [27]	MDA-MB-468	≈2750[28]
7.	50 nm, coated with BSA [27]	MDA-MB-468	≈1700[28]
8.	30 nm, conjugated to anti-EGFR antibody [93]	A431	39000
9.	15 nm, PEGylated and conjugated to trastuzumab [50]	BT474	430000
10.	30 nm, PEGylated [70]	PC-3	22700

4.3.5 Investigation of the spatial distribution of gold-nanoparticles in the cell with TEM

The purpose of the transmission electron microscopy (TEM) investigations was to determine the location of the gold-nanoparticles (50 nm) in the cell and to get a direct optical verification of the gold-nanoparticle uptake. For the preparation of the TEM samples the cells were incubated with gold-cmHsp70.1, respectively gold-BSA. The cells were then detached from the cell culture vessel and were centrifuged. The obtained cell pellets were red (Figure 4.43). This result already indicates that gold-BSA, respectively gold-cmHsp70.1 were internalized into the cell or at least attached to the cell membrane.

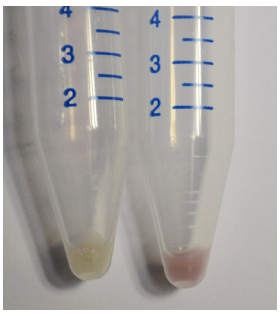

Figure 4.43: Cell pellets of 4T1 cells without gold (left) and after incubation with 50 nm gold-cmHsp70.1 (right).

[28]Data was read off Table Supplement Figure S4 and Supplement Figure S6 [27].

The further preparation steps of the cell pellets for the TEM analysis were performed by the Institute of Pathology at the Helmholtz Zentrum Munich (Prof. Dr. A. Walch and Dr. M. Aichler). The resulting TEM images are shown in Figure 4.44. The images show only part of the cell, approximately 2.9× 2.9 µm. The uptake and localization of gold-cmHsp70.1 (second row) and gold-BSA (first row) is compared for different incubation times. In the three gold-BSA TEM images only a few gold-nanoparticles are visible (yellow arrows in Figure 4.44(a), (b) and (c)). The gold-nanoparticles from the gold-cmHsp70.1 could not be detected at all (Figure 4.44(d), (e) and (f)).
Ultra-thin slices of the cells with a thickness of approximately 60 nm are needed for the TEM examinations. Assuming a cell diameter of 13 µm, the volume of the ultra-thin slice is then only about 0.7% of the total cell volume and in Figure 4.44 only 0.04% of the total cell volume is shown. Due to the small number of nanoparticles per cell (as calculated with the ICP-OES measurements) the probability to detect gold-nanoparticles in the ultra-thin slices is very low, e.g. for the maximum of 90 nanoparticles per cell, only 0.63 nanoparticles per ultra-thin slice or 0.039 nanoparticles in each subfigure are expected. Furthermore the complex sample preparation for the TEM could furthermore lead to a washout of the gold-nanoparticles.

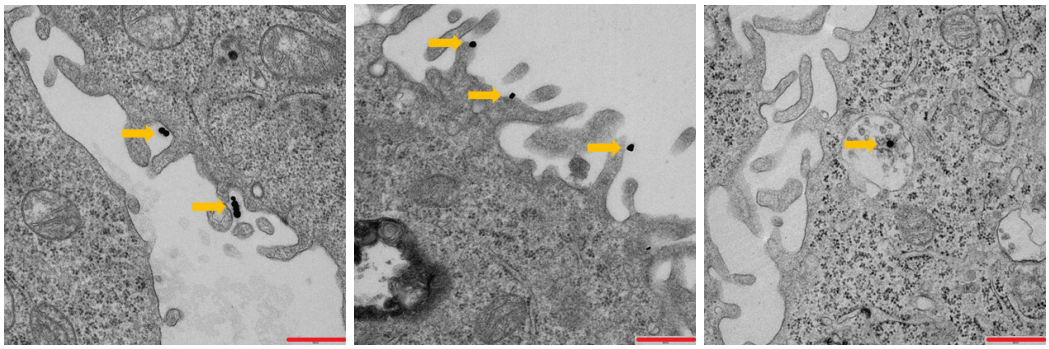

(a) Gold-BSA, incubation time: 2h

(b) Gold-BSA, incubation time: 4h

(c) Gold-BSA, incubation time: 6h

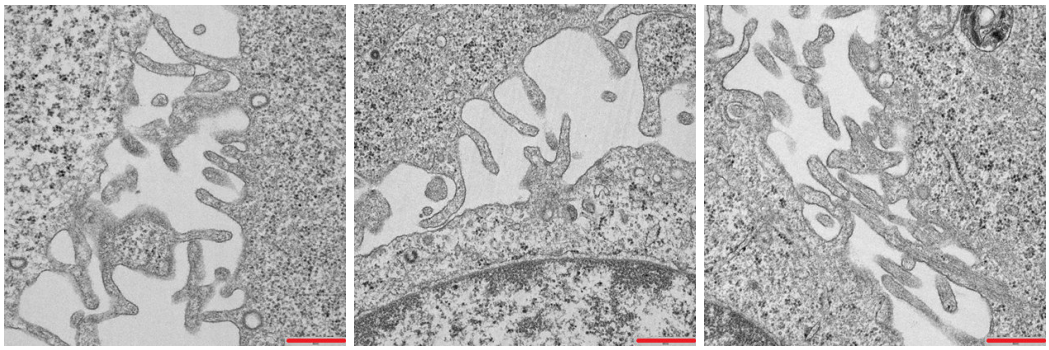

(d) Gold-cmHsp70.1, incubation time: 2h

(e) Gold-cmHsp70.1, incubation time: 4h

(f) Gold-cmHsp70.1, incubation time: 6h

Figure 4.44: TEM images of 4T1 cells after the incubation with 50 nm gold-cmHsp70.1 or 50 nm gold-BSA (Magnification 10000×, length of the scale bar: 500 nm).

4.3.6 Conclusion

Summarizing the results of the biological experiments yields the following outcome. A titration series with different antibody concentrations has shown that the addition of cmHsp70.1 to the gold solution stabilizes the gold-nanoparticles by replacing the citrate layer around the gold-nanoparticles. The conjugation of cmHsp70.1 was then verified with a dot blot using gold-nanoparticles, which are conjugated to the primary antibody cmHsp70.1. Furthermore the differences in the UV-visible spectra of gold-solution, gold-cmHsp70.1 and gold-BSA indicate that the conjugation of gold-nanoparticles and cmHsp70.1 respectively BSA was successful. Last but not least, the ICP-OES measurements showing differences in the cellular uptake of gold-cmHsp70.1 and gold-BSA lead to the conclusion that gold-nanoparticles were successfully conjugated to the cmHsp70.1 antibody.

Table 4.25: Estimated amount of gold per cell based on gold uptake experiments from literature and own experiments.

	Nanoparticle characterization and Reference	calculated mass of gold per cell [pg]	cell diameter d=26 µm fractional weight of gold [w%]	cell diameter d=13 µm fractional weight of gold [w%]
		references		
1	14 nm, stabilized by citric acid [26]	0.0832	0.0009	0.0074
2	50 nm, stabilized by citric acid [26]	7.7812	0.0805	0.6636
3	74 nm, stabilized by citric acid [26]	12.239	0.1265	1.0428
4	50 nm, uncoated [27]	9.4739	0.0980	0.8078
5	50 nm, coated with BSA [27]	5.1790	0.0536	0.4418
6	50 nm, uncoated [27]	3.4738	0.0359	0.2959
7	50 nm, coated with BSA [27]	2.1474	0.0222	0.1830
8	30 nm, conjugated to anti-EGFR antibody [93]	10.064	0.1041	0.8581
9	15 nm, PEGylated and conjugated to trastuzumab [50]	14.666	0.1517	1.2505
10	30 nm, PEGylated [70]	6.1936	0.0641	0.5284
		own results		
11	50 nm, gold-BSA	0.1137	0.0012	0.0099
12	50 nm, gold-cmHsp70.1	0.0834	0.0009	0.0074
13	15 nm, gold-BSA	2.3917	0.0240	0.2039
14	15 nm, gold-cmHsp70.1	1.0000	0.0103	0.0853

To address the question whether the concentration of gold-nanoparticles inside the cell or attached to the cell membrane is sufficient for spectral CT imaging, the density of the cell was assumed to be $1.02\,\mathrm{g/cm^3}$. The cell diameter ranges a lot for different cell

types. For the used 4T1 cells the cell diameter was approximated by 13 µm (Figure 3.7). For a second alternative evaluation, a cell diameter of 26 µm, as proposed by Lechtman et al. [70], was assumed. Based on the assumption that the cell is a sphere, calculating the cell volume and mass gives 1150 µm^3 and 1.1734 ng and 9480 µm^3 and 9.6696 ng, respectively. With this estimated cell masses, the density of gold (ρ_{gold} =19.3 g/cm^3), the mass of each nanoparticle ($m_{\text{nanoparticle}} = 4/3\pi r^3 \rho_{\text{gold}}$) and the number of nanoparticles per cell (Table 4.24 and 4.23) the fractional weight of gold per cell was calculated (Table 4.25). The required concentration of gold obtained by the simulations (0.2w% gold) cannot be attained for the cell diameter of 26 µm. Only for the 15 nm PEGylated gold-nanoparticles, which were conjugated to trastuzumab (Table 4.25 (9.)), the concentration was close to the required concentration of 0.2w%. For a cell diameter of 13 µm almost all measurements in Table 4.25 would be sufficient for spectral-CT imaging. However, the results obtained within this thesis (Table 4.25 (11.)-(14.)) yield very small amounts of gold. Only the 15 nm gold-BSA amount (assumed cell diameter 13 µm) would be sufficient for spectral-CT imaging as estimated by simulations in Section 4.1.

The ICP-OES measurements seem to be reliable as the measured amount of the gold-solution corresponds well with the named amount. The unsatisfactory results of the TEM images are a result of the small number of nanoparticles per cell. Further research is required to optimize the conjugation of the antibodies to the gold-nanoparticles.

Chapter 5

Conclusion and Summary

Computed tomography (CT) is an important X-ray-based diagnostic tool in medical imaging, especially for cancer diagnosis and therapy monitoring. A drawback of CT imaging, however, is the lack of targeted and molecularly specific CT contrast agents. Newly developed spectral CT devices with an energy-selective and photon-counting detector can be expected to substantially increase the sensitivity and the specificity of contrast agent detection. High-atomic-number materials such as gold-nanoparticles are promising new contrast agents for these systems, which can be detected by exploiting the material-specific K-edge absorption properties. A restricting factor for the application of gold-nanoparticles as spectral CT contrast agents in humans is the required in-vivo concentration of gold.
The potential improvement of medical tumor imaging by combining spectral CT and the properties of gold-nanoparticles was the background and motivation of this thesis. The major part of this work reports the design and analysis of Monte-Carlo simulations of medical spectral CT imaging with gold as a contrast agent; the purpose of these simulations were to demonstrate the general feasibility of gold-enhanced spectral CT, to optimize and evaluate acquisition and post-processing strategies, and to estimate the minimum in-vivo concentration of gold required for sufficient image contrast in spectral CT. Furthermore the dose enhancement effect of gold was examined, to estimate potential side effects. For both tasks Monte Carlo simulations were performed with the software tool EGSnrc, which models the transition of photons and electrons through matter. Finally, biological experiments were performed in which gold-nanoparticles were functionalized with a tumor-specific antibody for nanoparticle-based targeted tumor imaging.
To compare and optimize spectral CT acquisition and post-processing strategies as well as to estimate the minimal tissue concentration of gold-nanoparticles required for gold-specific spectral CT, Monte Carlo simulations were performed in two voxel phantoms. The first phantom was a simple cylindrical voxel phantom consisting of simulated liver parenchyma and five sets of four metastases. The metastases had sizes between $0.35 \times 0.35\,\mathrm{cm}^2$ and $1.4 \times 1.4\,\mathrm{cm}^2$. For each set of four metastases, different concentrations of gold (0.7w%, 0.4w%, 0.3w%, 0.2w% and 0.1w%) were added to the metastases. The second phantom

was an anatomic human voxel phantom, where three liver metastases with gold concentrations of 0.3w% and 0.2w% were implemented. Spectral CT was simulated with a 120 kV X-ray source and an ideal energy-selective and photon-counting detector. The energy-resolved projection data was binned to six energy bins with thresholds optimized with respect to the attenuation properties of gold and biological tissue. The generated spectral data sets were then processed with different material-decomposition algorithms: K-edge decomposition (applied to the raw data sets), eigenvector decomposition, and a least-squares parameter estimation. Furthermore two filters were applied to reduce noise in the images: a bilateral filter and a density filter. The calculated decomposed images were evaluated with respect to the signal-to-noise ratio (SNR), the contrast-to-noise ratio (CNR), and the contrast of the metastases.

To distinguish gold from background and to precisely identify the metastases, a high contrast and low noise is needed characterized by the image-quality parameters CNR and contrast. The eigenvector decomposition provided a high SNR in the gold images, but the CNR and the contrast were comparably low. The K-edge decomposition and the least squares parameter estimation provided very good results, which could be further improved by the additional application of the bilateral filter and the density filter. The K-edge decomposition yielded higher SNR, but lower CNR and contrast than the least-squares parameter estimation. The least-squares parameter estimation in combination with the bilateral and density filter revealed the highest CNR and contrast, while the SNR was only about 10% smaller than for the K-edge algorithm in combination with the bilateral filter. The computing time for the K-edge decomposition was by a factor of approximately 11 longer than for the least-squares parameter estimation, which, summarizing the results described above, appeared to be the most recommandable post-processing algorithm for gold-specific spectral CT. In the simple voxel phantom, the biggest metastasis ($1.4\times1.4\,\mathrm{cm}^2$) with 0.1w% gold was weakly detected by all three algorithms, while the smaller metastases with 0.1w% gold were not or hardly visible. All three algorithms allowed the specific identification of gold, i.e. a clear distinction between gold and bone, in all three metastases with 0.3w% gold in the human voxel phantom. The smallest metastasis ($0.35\times0.35\,\mathrm{cm}^2$) in the human voxel phantom with 0.2w% was only faintly visible in the decomposed images, and it was hard to distinguish between noise and the metastasis. The numerical values in the gold images of the three different algorithms represent the fractional weight of gold in the tissue. All algorithms underestimate the absolute concentration of gold (up to 56%) in all metastases and both phantoms. The eigenvector decomposition and the K-edge decomposition provide slightly better results than the least-squares parameter estimation. Summarized, the accomplished results indicate a lower limit of 0.2w% on the required gold enrichment in malignant tissue for the specific identification of gold in spectral CT imaging.

The dose enhancement effect in the vicinity of gold-nanoparticles is a consequence of the

higher mass attenuation coefficient of gold compared to biological tissues. This effect leads to an increased absorption followed by secondary electron production when the incoming photons interact with gold-nanoparticles. On the one hand, it should be carefully considered as undesirable side effect of gold-based contrast agents; on the other hand, the dose enhancement effect might also be of interest for the application of gold-nanoparticles in radiotherapy. The dose enhancement was simulated with EGSnrc, which provided information about the secondary Compton, photo-electric and Auger electron spectra and about the deposited dose. The simulations revealed a significant dose enhancement effect in the considered energy range, which mainly depends on the gold concentration and almost not on the used X-ray tube voltage. For the concentration of 0.2w% gold in tissue, a dose enhancement of 2.77 (ratio of absorbed dose with and without gold) was found. Thus, for a safe application of gold-nanoparticles in medical imaging, a specific localized targeting of gold-nanoparticles should be ensured to protect healthy tissue against this additional dose.

One beneficial characteristic of gold-nanoparticles is the possibility to easily couple them with biological targeting molecules, which enables targeted nanoparticle-based tumor imaging. Whether the required gold concentration found above can be specifically targeted to malignant tissue was investigated with cell culture experiments. The tumor specific monoclonal antibody cmHsp70.1 was conjugated to gold-nanoparticles (gold-cmHsp70.1) with a diameter of 50 nm and 15 nm. As a reference gold-nanoparticles were coated only with (non-targeting) BSA (gold-BSA). Spectroscopy with wavelengths of the ultraviolet and visible spectrum as well as inductively coupled plasma optical emission spectrometry (ICP-OES) measurements indicated that the conjugation of cmHsp70.1 and gold-nanoparticles was successful. The gold amount per cell was measured with ICP-OES. Unfortunately only the unspecific 15 nm gold-BSA showed a sufficient accumulation in the cells with the required concentration of about 0.2w%. Specific targeting of tumor cells with gold-cmHsp70.1 did not lead to a sufficiently high accumulation of gold-nanoparticles. Thus, a further optimization of the conjugation process of gold-nanoparticles and antibody is required to obtain a considerably higher cellular accumulation of gold.

In conclusion, gold-nanoparticles are promising candidates for medical spectral CT imaging. The Monte Carlo simulations performed for this thesis provide performance comparisons of different material-decomposition algorithms and, in particular, an estimation of the minimum concentration of gold in tissue (0.2w%) required for gold-specific spectral CT in humans. Cell culture experiments performed for this thesis indicate that a concentration of 0.2w% gold in tissue might be realistically obtained with an optimized antibody conjugation procedure. Thus, it remains to be examined whether and how the required gold concentration in malignant tissue in vivo can be achieved in practice. Further research needs to be done concerning the uptake, specific targeting and functionalization, kinetics of biodistribution and toxic effects of gold-nanoparticles.

Kapitel 6

Zusammenfassung

Die Computertomographie (CT) hat als röntgenbasiertes bildgebendes Verfahren vor allem für die Krebsdiagnostik und Therapieüberwachung einen hohen medizinischen Stellenwert. Allerdings ist bislang keine molekulare Bildgebung mit der Computertomographie möglich. Neu entwickelte Spektral-CT-Geräte mit einem energieselektiven und Photonen zählenden Detektor ermöglichen einen wichtigen Fortschritt in der CT-Bildgebung. Diese neuen CT-Systeme sollen zu einer Erhöhung der Sensitivität und der Spezifität bei der Detektion von Kontrastmitteln führen. Materialien mit einer hohen Ordnungszahl, wie z.B. Gold-Nanopartikel, sind vielversprechende neue Kontrastmittel und können mit Hilfe der materialspezifischen Absorptionseigenschaften an der K-Kante detektiert werden.
Den Hintergrund und die Motivation für diese Doktorarbeit bildete das Verbesserungspotential in der medizinischen Tumorbildgebung durch die Kombination von Spektral-CT und den spezifischen Eigenschaften von Gold-Nanopartikeln. Der Hauptteil der Arbeit beschreibt die Entwicklung und Analyse von Monte-Carlo-Simulationen der medizinischen Spektral-CT-Bildgebung mit Gold als Kontrastmittel. Der Zweck der Simulationen bestand in der Demonstration der generellen Realisierbarkeit des gold-verstärkten Spektral-CT, der Optimierung und Auswertung von Aufnahme- und Nachbearbeitungsstrategien, sowie der Abschätzung der minimalen In-vivo-Goldkonzentration, die für einen ausreichenden Bildkontrast im Spektral-CT benötigt wird. Weiterhin wurde der Dosiserhöhungseffekt von Gold untersucht, um mögliche Nebenwirkungen besser abschätzen zu können. Für beide Fragestellungen wurden Monte-Carlo-Simulationen mit der Software-Anwendung EGSnrc berechnet; EGSnrc modelliert den Transport von Photonen und Elektronen in Gewebe. Im letzten Teil der Arbeit wurden biologische Experimente durchgeführt, um eine zielgerichtete Tumorbildgebung mit Nanopartikel zu ermöglichen. Die Gold-Nanopartikel wurden hierzu mit einem tumorspezifischen Antikörper gekoppelt.
Um die Einstellungen des Spektral-CTs und die Nachbearbeitungsstrategien zu vergleichen und zu optimieren, sowie die benötigte minimale Goldkonzentration im Geweben zu bestimmen, wurden Monte-Carlo-Simulationen mit zwei Voxelphantomen durchgeführt. Das erste Phantom war ein einfaches zylindrisches Voxelphantom, das aus simuliertem Le-

bergewebe und fünf Gruppen mit je vier Metastasen besteht. Die Metastasen hatten eine Größe zwischen $0{,}35\times0{,}35\,\mathrm{cm}^2$ und $1{,}4\times1{,}4\,\mathrm{cm}^2$. Jede Gruppe von je vier Metastasen enthielt eine unterschiedliche Goldkonzentration (0,7w%, 0,4w%, 0,3w%, 0,2w% und 0,1w%). Das zweite Phantom war ein anatomisches Human-Voxelphantom bei dem drei Lebermetastasen mit einer Goldkonzentration von 0,3w% bzw. 0,2w% implementiert wurden. Das Spektral-CT wurde mit einer 120-kV-Röntgenquelle und einem idealen energieselektiven und photonen-zählenden Detektor implementiert. Die energieaufgelösten Projektionsdaten wurden in sechs Energie-Bins aufgeteilt. Die Grenzen der einzelnen Bins wurden unter Berücksichtigung der Abschwächungseigenschaften von Gold und biologischem Gewebe optimiert. Die so generierten spektralen Datensätze wurden dann mit verschiedenen Materialzerlegungsalgorithmen weiterverarbeitet: eine K-Kanten-Zerlegung (angewendet auf die Rohdaten), eine Eigenvektor-Zerlegung und einer Kleinste-Quadrate-Parameterschätzung. Zur Rauschreduzierung in den Bildern wurden zusätzlich zwei Filter, ein bilateraler und ein Dichtefilter angewendet. Die so erzeugten zerlegten Bilder wurden in Bezug auf das Signal-Rausch-Verhältnis (SNR), das Kontrast-Rausch-Verhältnis (CNR) und den Kontrast der Metastasen ausgewertet.

Um Gold vom Hintergrund zu unterscheiden und zur exakten Identifizierung der Metastasen wird ein hoher Kontrast und ein geringes Rauschen benötigt; dies wird durch die Bildqualitätsparameter CNR und Kontrast charakterisiert. Die Eigenvektor-Zerlegung lieferte ein hohes SNR in den Goldbildern, allerdings war das CNR und der Kontrast vergleichsweise niedrig. Die K-Kanten-Zerlegung und die Kleinste-Quadrate-Parameterschätzung lieferten sehr gute Ergebnisse, die durch die zusätzliche Anwendung des bilateralen und des Dichtefilters noch verbessert werden konnten. Die K-Kanten-Zerlegung ergab ein höheres SNR, aber ein geringeres CNR und geringeren Kontrast als die Kleinste-Quadrate-Parameterschätzung. Die Kleinste-Quadrate-Parameterschätzung in Kombination mit dem bilateralen und dem Dichtefilter lieferte das höchste CNR und den höchsten Kontrast, wobei das SNR nur ca. 10% geringer war, als für die K-Kanten-Zerlegung in Kombination mit dem bilateralen Filter. Die Berechnungszeit für die K-Kanten-Zerlegung ist annähernd 11 mal länger als für die Kleinste-Quadrate-Parameterschätzung. Zusammenfassend kann man sagen, dass die Kleinste-Quadrate-Parameterschätzung der empfehlenswerteste Nachbearbeitungsalgorithmus für das Gold-spezifische Spektral-CT ist. Im einfachen Voxelphantom wurde die größte Metastase ($1{,}4\times1{,}4\,\mathrm{cm}^2$) mit 0,1w% Gold von allen drei Algorithmen schwach detektiert, die kleineren Metastasen waren allerdings nicht oder kaum sichtbar. Alle drei Algorithmen ermöglichen die spezifische Identifizierung der drei Metastasen mit 0,3w% Gold im Human-Voxelphantom, d.h. eine klare Unterscheidung zwischen Gold und Knochen. Die kleinste Metastase ($0{,}35\times0{,}35\,\mathrm{cm}^2$) mit 0,2w% Gold im Human-Voxelphantom war in den zerlegten Goldbildern nur schwach sichtbar; eine eindeutige Unterscheidung zwischen Rauschen und der Metastase war kaum möglich. Die numerischen Werte in den Goldbildern der drei Zerlegungsalgorithmen geben den Gewichtsanteil

von Gold im Gewebe an. Alle Algorithmen unterschätzten die absolute Konzentration von Gold (bis zu 56%) in allen Metastasen und beiden Phantomen. Die Eigenvektor- und die K-Kanten-Zerlegung lieferten geringfügig bessere Ergebnisse als die Kleinste-Quadrate-Parameterschätzung. In der Zusammenfassung kann man für die Spektral-CT-Bildgebung mit Gold die benötigte minimale Goldkonzentration in malignem Gewebe mit 0,2w% angeben.

Die Dosiserhöhung in der Umgebung von Gold-Nanopartikeln basiert auf dem höheren Absorptionskoeffizienten von Gold im Vergleich zu biologischem Gewebe. Bei der Wechselwirkung von Photonen mit Gold-Nanopartikeln kommt es daher zu einer erhöhten Absorption und der Erzeugung von Sekundärelektronen. Auf der einen Seite sollte dies als unerwünschte Nebenwirkung von auf gold-basierenden Kontrastmitteln sorgfältig überprüft werden; auf der anderen Seite kann der Dosiserhöhungseffekt für die Anwendung von Gold-Nanopartikeln in der Strahlentherapie genutzt werden. Die Simulations-Untersuchungen zur Dosiserhöhung wurden mit EGSnrc durchgeführt und lieferten Informationen über die Sekundärelektronenspektren von Compton-, Photo- und Auger-Elektronen und die deponierte Dosis. Die Simulationen zeigen einen deutlichen Dosiserhöhungseffekt im betrachteten Energiebereich, wobei die Dosiserhöhung hauptsächlich von der Goldmenge im Gewebe abhängt und kaum von der Röntgenröhren-spannung. Für eine Goldkonzentration von 0,2w% ergibt sich eine Dosiserhöhung von 2,77 (Verhältnis von absorbierter Dosis mit und ohne Gold). Für eine sichere Anwendung von Gold-Nanopartikeln in der medizinischen Bildgebung sollte daher eine räumlich spezifische Anreicherung der Gold-Nanopartikel sichergestellt werden, um gesundes Gewebe vor der zusätzlichen Strahlenbelastung zu schützen.

Eine nützliche Eigenschaft von Gold-Nanopartikeln ist die Möglichkeit, sie an biologische Moleküle zu koppeln, um so eine zielgerichtete Tumorbildgebung zu ermöglichen. Ob die oben bestimmte benötigte Goldkonzentration spezifisch und zielgerichtet in malignem Gewebe erreicht werden kann, wurde mit Zellkulturexperimenten untersucht. Der tumorspezifische Antikörper cmHsp70.1 wurde an Gold-Nanopartikel mit einem Durchmesser von 50 nm und 15 nm gekoppelt. Als Referenz wurden Gold-Nanopartikel mit BSA (unspezifisch) beschichtet. Spektroskopische Messungen mit Wellenlängen im ultravioletten und sichtbaren Spektrum, sowie die optische Emissionsspektrometrie mit induktiv gekoppeltem Plasma (ICP-OES) deuteten darauf hin, dass die Kopplung von cmHsp70.1 und Gold-Nanopartikeln erfolgreich war. Die Goldmenge pro Zelle wurde mit ICP-OES bestimmt. Leider ergab sich nur für die unspezifischen 15 nm Gold-Nanopartikel eine ausreichende Anreicherung in den Zellen von rund 0,2w%. Der spezifische und zielgerichtete Gold-cmHsp70.1-Komplex führte nicht zu einer ausreichend hohen Anreicherung von Gold-Nanopartikeln. Eine weitere Optimierung des Kopplungsprozesses von Gold-Nanopartikeln und Antikörper ist daher erforderlich, um eine deutlich höhere Anreicherung von Gold in den Zellen zu erreichen.

Abschließend kann festgehalten werden, dass Gold-Nanopartikel vielversprechende neue Spek-tral-CT-Kontrastmittel sind. Die im Rahmen dieser Arbeit durchgeführten Monte-Carlo-Simulationen liefern einen Vergleich von unterschiedlichen Materialzerlegungsalgorithmen und insbesondere eine Abschätzung der minimal benötigten Goldkonzentration im Gewebe (0,2w%) für die Spektral-CT-Bildgebung im Menschen. Zellkulturexperimente, die für diese Arbeit durchgeführt wurden, lassen vermuten, dass eine Konzentration von 0,2w% Gold im Gewebe mit einer optimierten Antikörperkopplung realistisch ist. Es bleibt daher noch zu zeigen, wie und ob die benötigte Goldmenge in malignem Gewebe in-vivo in der Praxis erreicht werden kann. Weiterführende Forschung hinsichtlich der Aufnahme, spezifischen Bindung, Biokinetik und der Toxizität von Gold-Nanopartikeln ist allerdings nötig.

Acknowledgments

I would like to express my sincere thanks to all people who helped and supported me during my work.
Foremost, I would like to express my profound gratitude to my doctoral advisor PD Dr. rer. nat. Olaf Dietrich, for his very helpful and friendly support.
I want to thank all members of the Research Unit Medical Radiation Physics and Diagnostics.
I would particularly like to thank Prof. Dr. Christoph Hoeschen for giving me the opportunity to perform this study.
My sincere thanks goes Dr. Helmut Schlattl and Dr. Uwe Oeh for their kind and helpful supervision.
I wish to thank Dr. Vera Höllriegl and Dr. Matthias Greiter for all the fruitful discussions, the technical and personal encouragement and advices.
My special thanks goes to Prof. Dr. Gabriele Multhoff for the donation of the 4T1 cells and the cmHsp70.1 antibody and for her advices.
I am very thankful for the help of Dr. Peter Noel and Adie Radin Nasirudin.
I would like to sincerely thank the Institute of Experimental Genetics for letting me work in their lab and for their kind assistance.
I wish to thank Prof. Dr. Bernhard Michalke, Peter Grill and Bärbel Benker for the ICP-OES and UV-Vis Spectrometer measurements.
My thanks go to Dr. Michaela Aichler and Gabrielle Mettenleiter for the TEM preparation and analysis.
Claudia Braun is greatly indebted for being a friend during all the time.
I am profoundly grateful for the support, motivation and understanding from my sister, my mother, my boyfriend and all my friends throughout the whole time .

This study was conducted in the framework of the m^4 cluster and was funded by the Federal Ministry of Education and Research - BMBF.

Bibliography

[1] Gold Colloid-Technical Data. Retrieved July 25th, 2012, from http://www.bbisolutions.com/support/technical-information/molar-concentration-of-nanoparticles/.

[2] Gold Colloids. Technical report, BBI Solutions. Retrieved July 25th, 2012 via personal correspondence from BBIsolutions.

[3] Tables of X-ray Mass Attenuation Coefficients and Mass Energy-Absorption Coefficients from 1keV to 20MeV for Elements Z=1 to 92 and 48 Additional Substances of Dosimetric Interest.

[4] A. M. Alkilany and C. J. Murphy. Toxicity and cellular uptake of gold nanoparticles: what we have learned so far? *J Nanopart Res*, 12(7):2313–2333, Sep 2010.

[5] M. Alqathami, A. Blencowe, U. J. Yeo, S. J. Doran, G. Qiao, and M. Geso. Novel multicompartment 3-dimensional radiochromic radiation dosimeters for nanoparticle-enhanced radiation therapy dosimetry. *Int J Radiat Oncol Biol Phys*, 84(4):e549–e555, Nov 2012.

[6] C. Alric, J. Taleb, G. Le Duc, C. Mandon, C. Billotey, A. Le Meur-Herland, T. Brochard, F. Vocanson, M. Janier, P. Perriat, S. Roux, and O. Tillement. Gadolinium chelate coated gold nanoparticles as contrast agents for both X-ray computed tomography and magnetic resonance imaging. *J Am Chem Soc*, 130(18):5908–5915, May 2008.

[7] R. E. Alvarez and A. Macovski. Energy-selective reconstructions in X-ray computerized tomography. *Phys Med Biol*, 21(5):733–744, Sep 1976.

[8] American Type Culture Collection (ATCC). 4T1 cell description. Retrieved August 19th, 2013, from http://www.atcc.org/Products/All/CRL-2539.aspx?geo_country=us.

[9] M. A. Anastasio and P. La Riviere. *Emerging Imaging Technologies in Medicine (Imaging in Medical Diagnosis and Therapy)*. CRC Press, Boca Raton, USA, 2012.

[10] N. G. Anderson, A. P. Butler, N. J. A. Scott, N. J. Cook, J. S. Butzer, N. Schleich, M. Firsching, R. Grasset, N. de Ruiter, M. Campbell, and P. H. Butler. Spectroscopic (multi-energy) CT distinguishes iodine and barium contrast material in MICE. *Eur Radiol*, 20(9):2126–2134, Sep 2010.

[11] A. Asea, S. K. Kraeft, E. A. Kurt-Jones, M. A. Stevenson, L. B. Chen, R. W. Finberg, G. C. Koo, and S. K. Calderwood. HSP70 stimulates cytokine production through a CD14-dependant pathway, demonstrating its dual role as a chaperone and cytokine. *Nat Med*, 6(4):435–442, Apr 2000.

[12] B. Aydogan, J. Li, T. Rajh, A. Chaudhary, S. J. Chmura, C. Pelizzari, C. Wietholt, M. Kurtoglu, and P. Redmond. AuNP-DG: deoxyglucose-labeled gold nanoparticles as X-ray computed tomography contrast agents for cancer imaging. *Mol Imaging Biol*, 12(5):463–467, Oct 2010.

[13] J. A. Barreto, W. O'Malley, M. Kubeil, B. Graham, H. Stephan, and L. Spiccia. Nanomaterials: applications in cancer imaging and therapy. *Adv Mater*, 23(12):H18–H40, Mar 2011.

[14] S. Basu, R. J. Binder, R. Suto, K. M. Anderson, and P. K. Srivastava. Necrotic but not apoptotic cell death releases heat shock proteins, which deliver a partial maturation signal to dendritic cells and activate the NF-kappa B pathway. *Int Immunol*, 12(11):1539–1546, Nov 2000.

[15] P. Baturin, Y. Alivov, and S. Molloi. Spectral CT imaging of vulnerable plaque with two independent biomarkers. *Phys Med Biol*, 57(13):4117–4138, Jul 2012.

[16] R. I. Berbeco, W. Ngwa, and G. M. Makrigiorgos. Localized dose enhancement to tumor blood vessel endothelial cells via megavoltage X-rays and targeted gold nanoparticles: new potential for external beam radiotherapy. *Int J Radiat Oncol Biol Phys*, 81(1):270–276, Sep 2011.

[17] M. Bethesda. Report 44 of the International Commission on Radiation Units and Measurements. Technical report, Tissue Substitutes in Radiation Dosimetry and Measurement, 1989.

[18] E. Boote, G. Fent, V. Kattumuri, S. Casteel, K. Katti, N. Chanda, R. Kannan, K. Katti, and R. Churchill. Gold nanoparticle contrast in a phantom and juvenile swine: models for molecular imaging of human organs using x-ray computed tomography. *Acad Radiol*, 17:410–417, 2010.

[19] C. Botzler, G. Li, R. D. Issels, and G. Multhoff. Definition of extracellular localized epitopes of Hsp70 involved in an NK immune response. *Cell Stress Chaperones*, 3(1):6–11, Mar 1998.

[20] J. S. Butzer, A. Butler, P. Butler, P. Bones, N. Cook, and L. Tlustos. Medipix Imaging - Evaluation of Datasets with PCA. *IEEE*, 2008.

[21] T. M. Buzug. *Einführung in die Computertomographie*. Springer Verlag Berlin Heidelberg, 2005.

[22] W. Cai, T. Gao, H. Hong, and J. Sun. Applications of gold nanoparticles in cancer nanotechnology. *Nanotechnology*, 1:17–32, 2008.

[23] N. Chattopadhyay, Z. Cai, J.-P. Pignol, B. Keller, E. Lechtman, R. Bendayan, and R. M. Reilly. Design and characterization of HER-2-targeted gold nanoparticles for enhanced X-radiation treatment of locally advanced breast cancer. *Mol Pharm*, 7(6):2194–2206, Dec 2010.

[24] Y.-S. Chen, Y.-C. Hung, I. Liau, and G. S. Huang. Assessment of the In Vivo Toxicity of Gold Nanoparticles. *Nanoscale Res Lett*, 4(8):858–864, 2009.

[25] B. D. Chithrani and W. C. W. Chan. Elucidating the mechanism of cellular uptake and removal of protein-coated gold nanoparticles of different sizes and shapes. *Nano Lett*, 7(6):1542–1550, Jun 2007.

[26] B. D. Chithrani, A. A. Ghazani, and W. C. W. Chan. Determining the size and shape dependence of gold nanoparticle uptake into mammalian cells. *Nano Lett*, 6(4):662–668, Apr 2006.

[27] B. D. Chithrani, J. Stewart, C. Allen, and D. A. Jaffray. Intracellular uptake, transport, and processing of nanostructures in cancer cells. *Nanomedicine*, 5(2):118–127, Jun 2009.

[28] D. B. Chithrani. Optimization of Bio-Nano Interface Using Gold Nanostructures as a Model Nanoparticle System. *Insciences Journal*, pages 115–135, Jul 2011.

[29] D. B. Chithrani, S. Jelveh, F. Jalali, M. van Prooijen, C. Allen, R. G. Bristow, R. P. Hill, and D. A. Jaffray. Gold nanoparticles as radiation sensitizers in cancer therapy. *Radiat Res*, 173(6):719–728, Jun 2010.

[30] S. H. Cho. Estimation of tumour dose enhancement due to gold nanoparticles during typical radiation treatments: a preliminary Monte Carlo study. *Phys Med Biol*, 50(15):N163–N173, Aug 2005.

[31] W.-S. Cho, M. Cho, J. Jeong, M. Choi, B. S. Han, H.-S. Shin, J. Hong, B. H. Chung, J. Jeong, and M.-H. Cho. Size-dependent tissue kinetics of PEG-coated gold nanoparticles. *Toxicol Appl Pharmacol*, 245(1):116–123, May 2010.

[32] L. Chouchane, F. S. Bowers, S. Sawasdikosol, R. M. Simpson, and T. J. Kindt. Heat-shock proteins expressed on the surface of human T cell leukemia virus type I-infected cell lines induce autoantibodies in rabbits. *J Infect Dis*, 169(2):253–259, Feb 1994.

[33] D. P. Clark, K. Ghaghada, E. J. Moding, D. G. Kirsch, and C. T. Badea. In vivo characterization of tumor vasculature using iodine and gold nanoparticles and dual energy micro-CT. *Phys Med Biol*, 58(6):1683–1704, Mar 2013.

[34] D. P. Cormode, E. Roessl, A. Thran, T. Skajaa, R. E. Gordon, J.-P. Schlomka, V. Fuster, E. A. Fisher, W. J. M. Mulder, R. Proksa, and Z. A. Fayad. Atherosclerotic plaque composition: analysis with multicolor CT and targeted gold nanoparticles. *Radiology*, 256(3):774–782, Sep 2010.

[35] K. Cranley, B. Gilmore, W. Fogarty, and L. Deponds. Catalogue of diagnostic x-ray spectra and other data. *IPEM Report. 78 (The Institute of Physics and Engineering in Medicine, York)*, 1997.

[36] W. H. De Jong, W. I. Hagens, P. Krystek, M. C. Burger, A. J. A. M. Sips, and R. E. Geertsma. Particle size-dependent organ distribution of gold nanoparticles after intravenous administration. *Biomaterials*, 29(12):1912–1919, Apr 2008.

[37] A. Detappe, P. Tsiamas, W. Ngwa, P. Zygmanski, M. Makrigiorgos, and R. Berbeco. The effect of flattening filter free delivery on endothelial dose enhancement with gold nanoparticles. *Med Phys*, 40(3):031706, Mar 2013.

[38] J. L. Ducote, Y. Alivov, and S. Molloi. Imaging of nanoparticles with dual-energy computed tomography. *Phys Med Biol*, 56(7):2031–2044, Apr 2011.

[39] M. Ferrarini, S. Heltai, M. R. Zocchi, and C. Rugarli. Unusual expression and localization of heat-shock proteins in human tumor cells. *Int J Cancer*, 51(4):613–619, Jun 1992.

[40] S. Feuerlein, E. Roessl, R. Proksa, G. Martens, O. Klass, M. Jeltsch, V. Rasche, H.-J. Brambs, M. H. K. Hoffmann, and J.-P. Schlomka. Multienergy photon-counting K-edge imaging: potential for improved luminal depiction in vascular imaging. *Radiology*, 249(3):1010–1016, Dec 2008.

[41] G. Frens. Controlled nucleation for the regulation of the particle size in monodisperse gold suspensions. *Nature*, 241:20–22, 1973.

[42] R. Gastpar, M. Gehrmann, M. A. Bausero, A. Asea, C. Gross, J. A. Schroeder, and G. Multhoff. Heat shock protein 70 surface-positive tumor exosomes stimulate migratory and cytolytic activity of natural killer cells. *Cancer Res*, 65(12):5238–5247, Jun 2005.

[43] M. Gehrmann, G. Liebisch, G. Schmitz, R. Anderson, C. Steinem, A. De Maio, G. Pockley, and G. Multhoff. Tumor-specific Hsp70 plasma membrane localization is enabled by the glycosphingolipid Gb3. *PLoS One*, 3(4):e1925, 2008.

[44] M. Gehrmann, J. Radons, M. Molls, and G. Multhoff. The therapeutic implications of clinically applied modifiers of heat shock protein 70 (Hsp70) expression by tumor cells. *Cell Stress Chaperones*, 13(1):1–10, 2008.

[45] J. Giersch, D. Niederlöhner, and G. Anton. The influence of energy weighting on X-ray imaging quality. *Nucl. Instrum. Methods A*, 531:68–74, 2004.

[46] B. J. Gonzales and D. Lalush. Performance of reconstruction and processing techniques for dense full-spectrum x-ray computed tomography. *IEEE Nuclear Science Symposuim & Medical Imaging Conference*, 2010.

[47] B. J. Gonzales and D. S. Lalush. Eigenvector decomposition of full-spectrum x-ray computed tomography. *Phys Med Biol*, 57(5):1309–1323, Mar 2012.

[48] M. A. Hahn, A. K. Singh, P. Sharma, S. C. Brown, and B. M. Moudgil. Nanoparticles as contrast agents for in-vivo bioimaging: current status and future perspectives. *Anal Bioanal Chem*, 399(1):3–27, Jan 2011.

[49] J. F. Hainfeld, F. A. Dilmanian, Z. Zhong, D. N. Slatkin, J. A. Kalef-Ezra, and H. M. Smilowitz. Gold nanoparticles enhance the radiation therapy of a murine squamous cell carcinoma. *Phys Med Biol*, 55(11):3045–3059, Jun 2010.

[50] J. F. Hainfeld, M. J. O'Connor, F. A. Dilmanian, D. N. Slatkin, D. J. Adams, and H. M. Smilowitz. Micro-CT enables microlocalisation and quantification of Her2-targeted gold nanoparticles within tumour regions. *Br J Radiol*, 84(1002):526–533, Jun 2011.

[51] J. F. Hainfeld, D. N. Slatkin, T. M. Focella, and H. M. Smilowitz. Gold nanoparticles: a new X-ray contrast agent. *Br J Radiol*, 79(939):248–253, Mar 2006.

[52] J. F. Hainfeld, D. N. Slatkin, and H. M. Smilowitz. The use of gold nanoparticles to enhance radiotherapy in mice. *Phys Med Biol*, 49(18):N309–N315, Sep 2004.

[53] M. Hantschel, K. Pfister, A. Jordan, R. Scholz, R. Andreesen, G. Schmitz, H. Schmetzer, W. Hiddemann, and G. Multhoff. Hsp70 plasma membrane expression on primary tumor biopsy material and bone marrow of leukemic patients. *Cell Stress Chaperones*, 5(5):438–442, Nov 2000.

[54] P. He, B. Wei, W. Cong, and G. Wang. Optimization of K-edge imaging with spectral CT. *Med Phys*, 39(11):6572–6579, Nov 2012.

[55] J. H. Hubbel and S. M. Seltzer. Tables of X-ray mass attenuation coefficients and mass energy-absorption coefficients from 1keV to 20MeV for elements Z=1 to 92 and 48 additional substances of dosimetric interest, 1996. Retrieved May 8th, 2012, from
http://physics.nist.gov/PhysRefData/Xcom/html/xcom1.html.

[56] International Commission on Radiological Protection. Basic anatomical and physiological data for use in radiological protection: reference values. *ICRP Publication 89, Pergamon Press, Oxford, UK*, 2002.

[57] P. Jackson, S. Periasamy, V. Bansal, and M. Geso. Evaluation of the effects of gold nanoparticle shape and size on contrast enhancement in radiological imaging. *Australas Phys Eng Sci Med*, 34(2):243–249, Jun 2011.

[58] I. T. Jolliffe. *Principal Component Analysis*, volume Second Edition. Springer Verlag New York, 2002.

[59] B. L. Jones, S. Krishnan, and S. H. Cho. Estimation of microscopic dose enhancement factor around gold nanoparticles by Monte Carlo calculations. *Med Phys*, 37(7):3809–3816, Jul 2010.

[60] W. A. Kalender, E. Klotz, and L. Kostaridou. An algorithm for noise suppression in dual energy CT material density images. *IEEE Trans Med Imaging*, 7(3):218–224, 1988.

[61] H. H. Kampinga, J. Hageman, M. J. Vos, H. Kubota, R. M. Tanguay, E. A. Bruford, M. E. Cheetham, B. Chen, and L. E. Hightower. Guidelines for the nomenclature of the human heat shock proteins. *Cell Stress Chaperones*, 14(1):105–111, Jan 2009.

[62] I. Kawrakow, E. Mainegra-Hing, D. W. Rogers, F. Tessier, and B. R. B. Walters. The EGSnrc Code System: Monte Carlo Simulation of Electron and Photon Transport. Technical report, National Research Council Canada, 2011.

[63] N. Khlebtsov and L. Dykman. Biodistribution and toxicity of engineered gold nanoparticles: a review of in vitro and in vivo studies. *Chem Soc Rev*, 40(3):1647–1671, Mar 2011.

[64] Y.-H. Kim, J. Jeon, S. H. Hong, W.-K. Rhim, Y.-S. Lee, H. Youn, J.-K. Chung, M. C. Lee, D. S. Lee, K. W. Kang, and J.-M. Nam. Tumor targeting and imaging using cyclic RGD-PEGylated gold nanoparticle probes with directly conjugated iodine-125. *Small*, 7(14):2052–2060, Jul 2011.

[65] J. M. Kinsella, R. E. Jimenez, P. P. Karmali, A. M. Rush, V. R. Kotamraju, N. C. Gianneschi, E. Ruoslahti, D. Stupack, and M. J. Sailor. X-Ray Computed Tomography Imaging of Breast Cancer by using Targeted Peptide-Labeled Bismuth Sulfide Nanoparticles. *Angew Chem Int Ed Engl*, 50(51):12308–12311, Dec 2011.

[66] O. Klein and Y. Nishina. Über die Streuung von Strahlung durch freie Elektronen nach der neuen relativistischen Quantendynamik von Dirac. *Zeitschrift fÜr Physik*, 52(11-12):853–868, Nov 1929.

[67] S. Kumar, J. Aaron, and K. Sokolov. Directional conjugation of antibodies to nanoparticles for synthesis of multiplexed optical contrast agents with both delivery and targeting moieties. *Nat Protoc*, 3(2):314–320, 2008.

[68] H. Q. Le and S. Molloi. Least squares parameter estimation methods for material decomposition with energy discriminating detectors. *Med Phys*, 38:245–255, 2011.

[69] E. Lechtman, N. Chattopadhyay, Z. Cai, S. Mashouf, R. Reilly, and J. P. Pignol. Implications on clinical scenario of gold nanoparticle radiosensitization in regards to photon energy, nanoparticle size, concentration and location. *Phys Med Biol*, 56(15):4631–4647, Aug 2011.

[70] E. Lechtman, S. Mashouf, N. Chattopadhyay, B. M. Keller, P. Lai, Z. Cai, R. M. Reilly, and J.-P. Pignol. A Monte Carlo-based model of gold nanoparticle radiosensitization accounting for increased radiobiological effectiveness. *Phys Med Biol*, 58(10):3075–3087, May 2013.

[71] M. K. K. Leung, J. C. L. Chow, B. D. Chithrani, M. J. G. Lee, B. Oms, and D. A. Jaffray. Irradiation of gold nanoparticles by x-rays: Monte Carlo simulation of dose enhancements and the spatial properties of the secondary electrons production. *Med Phys*, 38(2):624–631, Feb 2011.

[72] J. Li, A. Chaudhary, S. J. Chmura, C. Pelizzari, T. Rajh, C. Wietholt, M. Kurtoglu, and B. Aydogan. A novel functional CT contrast agent for molecular imaging of cancer. *Phys Med Biol*, 55(15):4389–4397, Aug 2010.

[73] S. Lindquist and E. A. Craig. The heat-shock proteins. *Annu Rev Genet*, 22:631–677, 1988.

[74] A. Macovski, R. E. Alvarez, J. L. Chan, J. P. Stonestrom, and L. M. Zatz. Energy dependent reconstruction in X-ray computerized tomography. *Comput Biol Med*, 6(4):325–336, Oct 1976.

[75] I. Martínez-Rovira and Y. Prezadoa. Monte Carlo dose enhancement studies in microbeam radiation therapy. *Med Phys*, 38(7):4430–4439, Jul 2011.

[76] H. Matsudaira, A. M. Ueno, and I. Furuno. Iodine contrast medium sensitizes cultured mammalian cells to X rays but not to gamma rays. *Radiat Res*, 84(1):144–148, Oct 1980.

[77] S. J. McMahon, M. H. Mendenhall, S. Jain, and F. Currell. Radiotherapy in the presence of contrast agents: a general figure of merit and its application to gold nanoparticles. *Phys Med Biol*, 53(20):5635–5651, Oct 2008.

[78] P. D. med. Ernst J. Rummeny. Antrag auf Förderung im Rahmen der BMBF-Fördermaßnahme Spitzenclusterwettbewerb - m4 "Personalisierte Medizin und zielgerichtete Therapien Eine neue Dimension in der Medikamentenentwicklung" Vorhaben PM8: "Entwicklung und Evaluation neuer CT und MRT-Techniken als Biomarker für die Beurteilung eines medikamentösen Therapieerfolgs". Technische Universität München Klinikum rechts der Isar.

[79] R. L. V. Metter, J. Beutel, and H. L. Kundel. *Handbook of Medical Imaging, Volume 1. Physics and Psychophysics (SPIE Press Monograph Vol. PM79/SC)*. SPIE Publications, 2009.

[80] G. Multhoff. Heat shock protein 70 (Hsp70): membrane location, export and immunological relevance. *Methods*, 43(3):229–237, Nov 2007.

[81] G. Multhoff, C. Botzler, M. Wiesnet, E. Müller, T. Meier, W. Wilmanns, and R. D. Issels. A stress-inducible 72-kDa heat-shock protein (HSP72) is expressed on the surface of human tumor cells, but not on normal cells. *Int J Cancer*, 61(2):272–279, Apr 1995.

[82] G. Multhoff and L. E. Hightower. Distinguishing integral and receptor-bound heat shock protein 70 (Hsp70) on the cell surface by Hsp70-specific antibodies. *Cell Stress Chaperones*, 16(3):251–255, May 2011.

[83] P. Njoki, I.-I. Lim, D. Mott, H.-Y. Park, B. Khan, S. Mishra, R. Sujakumar, J. Luo, and C.-J. Zhong. Size Correlation of Optical and Spectroscopic Properties for Gold Nanoparticles. *Journal of Physical Chemistry C*, 111(40):14664???14669, Oct 2007.

[84] T. Nowak, M. Hupfer, R. Brauweiler, F. Eisa, and W. A. Kalender. Potential of high-Z contrast agents in clinical contrast-enhanced computed tomography. *Med Phys*, 38(12):6469–6482, Dec 2011.

[85] K. Pfister, J. Radons, R. Busch, J. G. Tidball, M. Pfeifer, L. Freitag, H.-J. Feldmann, V. Milani, R. Issels, and G. Multhoff. Patient survival by Hsp70 membrane phenotype: association with different routes of metastasis. *Cancer*, 110(4):926–935, Aug 2007.

[86] H. Pietsch, G. Jost, T. Frenzel, M. Raschke, J. Walter, H. Schirmer, J. Hütter, and M. A. Sieber. Efficacy and safety of lanthanoids as X-ray contrast agents. *Eur J Radiol*, 80(2):349–356, Nov 2011.

[87] G. G. Poludniowski. Calculation of x-ray spectra emerging from an x-ray tube. Part II. X-ray production and filtration in x-ray targets. *Med Phys*, 34(6):2175–2186, Jun 2007.

[88] G. G. Poludniowski and P. M. Evans. Calculation of x-ray spectra emerging from an x-ray tube. Part I. electron penetration characteristics in x-ray targets. *Med Phys*, 34(6):2164–2174, Jun 2007.

[89] R. Popovtzer, A. Agrawal, N. A. Kotov, A. Popovtzer, J. Balter, T. E. Carey, and R. Kopelman. Targeted gold nanoparticles enable molecular CT imaging of cancer. *Nano Lett*, 8(12):4593–4596, Dec 2008.

[90] O. Rabin, J. Manuel Perez, J. Grimm, G. Wojtkiewicz, and R. Weissleder. An X-ray computed tomography imaging agent based on long-circulating bismuth sulphide nanoparticles. *Nat Mater*, 5(2):118–122, Feb 20042006.

[91] G. Raschke. *Molekulare Erkennung mit einzelnen Gold-Nanopartikeln*. PhD thesis, Ludwig-Maximilians-Universität München, 2005.

[92] D. F. Regulla, L. B. Hieber, and M. Seidenbusch. Physical and biological interface dose effects in tissue due to X-ray-induced release of secondary radiation from metallic gold surfaces. *Radiat Res*, 150(1):92–100, Jul 1998.

[93] T. Reuveni, M. Motiei, Z. Romman, A. Popovtzer, and R. Popovtzer. Targeted gold nanoparticles enable molecular CT imaging of cancer: an in vivo study. *Int J Nanomedicine*, 6:2859–2864, 2011.

[94] F. Ritossa. Discovery of the heat shock response. *Cell Stress Chaperones*, 1(2):97–98, Jun 1996.

[95] E. Roessl and C. Herrmann. Cramér-Rao lower bound of basis image noise in multiple-energy x-ray imaging. *Phys Med Biol*, 54(5):1307–1318, Mar 2009.

[96] E. Roessl, C. Herrmann, E. Kraft, and R. Proksa. A comparative study of a dual-energy-like imaging technique based on counting-integrating readout. *Med Phys*, 38(12):6416–6428, Dec 2011.

[97] E. Roessl and R. Proksa. K-edge imaging in x-ray computed tomography using multi-bin photon counting detectors. *Phys Med Biol*, 52(15):4679–4696, Aug 2007.

[98] L. Romans. CT Image Quality, 2013. Retrieved September 2th, 2013, from http://www.cewebsource.com/coursePDFs/CTimageQuality.pdf.

[99] C. O. Schirra, B. Brendel, M. A. Anastasio, and E. Roessl. Spectral CT: a technology primer for contrast agent development. *Contrast Media Mol Imaging*, 9(1):62–70, Jan 2014.

[100] J. P. Schlomka, E. Roessl, R. Dorscheid, S. Dill, G. Martens, T. Istel, C. Bäumer, C. Herrmann, R. Steadman, G. Zeitler, A. Livne, and R. Proksa. Experimental feasibility of multi-energy photon-counting K-edge imaging in pre-clinical computed tomography. *Phys Med Biol*, 53(15):4031–4047, Aug 2008.

[101] T. G. Schmidt. Optimal "image-based" weighting for energy-resolved CT. *Med Phys*, 36(7):3018–3027, Jul 2009.

[102] E. Schmitt, M. Gehrmann, M. Brunet, G. Multhoff, and C. Garrido. Intracellular and extracellular functions of heat shock proteins: repercussions in cancer therapy. *J Leukoc Biol*, 81(1):15–27, Jan 2007.

[103] M. Sherman and G. Multhoff. Heat shock proteins in cancer. *Ann N Y Acad Sci*, 1113:192–201, Oct 2007.

[104] P. M. Shikhaliev. The upper limits of the SNR in radiography and CT with polyenergetic x-rays. *Phys Med Biol*, 55(18):5317–5339, Sep 2010.

[105] P. M. Shikhaliev. Photon counting spectral CT: improved material decomposition with K-edge-filtered x-rays. *Phys Med Biol*, 57(6):1595–1615, Mar 2012.

[106] P. M. Shikhaliev, T. Xu, and S. Molloi. Photon counting computed tomography: concept and initial results. *Med Phys*, 32(2):427–436, Feb 2005.

[107] P. C. Shrimpton, H. M. C., M. A. Lewis, and M. Dunn. *Dose from Computed Tomography (CT) Examinations in the UK - 2003 Review*. National Radiological Protection Board, 2005.

[108] S. Stangl, M. Gehrmann, R. Dressel, F. Alves, C. Dullin, G. Themelis, V. Ntziachristos, E. Staeblein, A. Walch, I. Winkelmann, and G. Multhoff. In vivo imaging of CT26 mouse tumours by using cmHsp70.1 monoclonal antibody. *J Cell Mol Med*, 15(4):874–887, Apr 2011.

[109] J. W. Steidley. Exploring the spectrum Advances and potential of spectral CT, 2008. Retrieved October 18th, 2011, from http://clinical.netforum.healthcare.philips.com/us_en/Explore/White-Papers/CT/Exploring-the-spectrum-Advances-and-potential-of-spectral-CT.

[110] K. Steiner, M. Graf, K. Hecht, S. Reif, L. Rossbacher, K. Pfister, H.-J. Kolb, H. M. Schmetzer, and G. Multhoff. High HSP70-membrane expression on leukemic cells from patients with acute myeloid leukemia is associated with a worse prognosis. *Leukemia*, 20(11):2076–2079, Nov 2006.

[111] R. Suto and P. K. Srivastava. A mechanism for the specific immunogenicity of heat shock protein-chaperoned peptides. *Science*, 269(5230):1585–1588, Sep 1995.

[112] V. Taranenko, M. Zankl, and H. Schlattl. Voxel phantom setup in MCNPX. In *American Nuclear Society Topical Meeting in Monte Carlo, Chattanooga, TN*, 2005.

[113] C. Tomasi and R. Manduchi. Bilateral Filtering for Gray and Color Images. *Proceedings of the 1998 IEEE International Conference on Computer Vision, Bombay, India*, pages 839–846, 1998.

[114] P. Tsiamas, B. Liu, F. Cifter, W. F. Ngwa, R. I. Berbeco, C. Kappas, K. Theodorou, K. Marcus, M. G. Makrigiorgos, E. Sajo, and P. Zygmanski. Impact of beam quality on megavoltage radiotherapy treatment techniques utilizing gold nanoparticles for dose enhancement. *Phys Med Biol*, 58(3):451–464, Feb 2013.

[115] J. Turkevich, P. C. Stevenson, and H. J. A study of the nucleation and growth processes in the synthesis of colloidal gold. *Discussions of the Faraday Society*, 11:55–75, 1951.

[116] G. Unak, F. Ozkaya, E. I. Medine, O. Kozgus, S. Sakarya, R. Bekis, P. Unak, and S. Timur. Gold nanoparticle probes: design and in vitro applications in cancer cell culture. *Colloids Surf B Biointerfaces*, 90:217–226, Feb 2012.

[117] A. Vanbuskirk, B. L. Crump, E. Margoliash, and S. K. Pierce. A peptide binding protein having a role in antigen presentation is a member of the HSP70 heat shock family. *J Exp Med*, 170(6):1799–1809, Dec 1989.

[118] T. Vogl, W. Reith, and E. Rummeny. *Diagnostische und Interventionelle Radiologie*. Springer Verlag Berlin Heidelberg, 2011.

[119] C.-H. Wang, C.-J. Liu, C.-L. Wang, T.-E. Hua, J. M. Obliosca, K. Lee, Y. Hwu, C.-S. Yang, R.-S. Liu, H.-M. Lin, et al. Optimizing the size and surface properties of polyethylene glycol (PEG)–gold nanoparticles by intense x-ray irradiation. *Journal of Physics D: Applied Physics*, 41(19):195301, 2008.

[120] W. J. Welch. Mammalian stress response: cell physiology, structure/function of stress proteins, and implications for medicine and disease. *Physiol Rev*, 72(4):1063–1081, Oct 1992.

[121] Y. Xu, O. Tischenko, and C. Hoeschen. Image reconstruction by OPED algorithm with averaging. *Numerical Algorithms*, 45(1-4):179–193, Aug 2007.

[122] X.-D. Zhang, D. Wu, X. Shen, P.-X. Liu, N. Yang, B. Zhao, H. Zhang, Y.-M. Sun, L.-A. Zhang, and F.-Y. Fan. Size-dependent in vivo toxicity of PEG-coated gold nanoparticles. *Int J Nanomedicine*, 6:2071–2081, 2011.

[123] Y. Zheng, D. J. Hunting, P. Ayotte, and L. Sanche. Radiosensitization of DNA by gold nanoparticles irradiated with high-energy electrons. *Radiat Res*, 169(1):19–27, Jan 2008.

Annex

A. Algorithms

Eigenvector decomposition

IDL algorithm used for the eigenvector decomposition (section 3.1.4.1).

Listing 6.1: IDL Source Code: Eigenvector decomposition algorithm

```
pro eigendecomp, file, dim ,FOD, speichern=sp
;Eigenvector decomposition
;file - reconstructed CT images
;dim -dimension of images [xsize x ysize x #bins]

time1 = systime(/seconds)

rdata=fltarr(dim)
for i=1, dim[2] do begin
  if (i lt 10) then filename=file+string(i,format='(i1)')+'.img' $
  else filename=file+string(i,format='(i2)')+'.img'
  img=read_binary(filename, data_type=4, data_dim=[dim[0],dim[1]])
endfor

f=fltarr([dim[2],3])

;Bins [25-47-60-75-81-86-120] optimized
f[*,0]=[13.070,5.9140,3.4790,2.3650,8.2920,5.5590] ;Gold
f[*,1]=[0.6125,0.3479,0.2623,0.2232,0.2100,0.1865] ;HardBoneMixture
f[*,2]=[0.2698,0.2162,0.1957,0.1844,0.1800,0.1709] ;Liver

;Bins [25-34-51-80-91-110-120] non-optimized
;f[*,0]=[25.470,10.490,3.9630,7.8490,5.3600,3.7850] ;Gold
;f[*,1]=[1.1110,0.5149,0.2792,0.2063,0.1847,0.1700] ;HardBoneMixture
;f[*,2]=[0.3638,0.2507,0.2001,0.1787,0.1701,0.1630] ;Liver

pixel=long(dim[0])*dim[1]
rdata=reform(rdata,[pixel,dim[2]])

;calculation of the correlation matrix
U=dblarr([dim[2],dim[2]])
pixel=long(dim[0])*dim[1]
cow=replicate(0.,[3,pixel])
for i=0,581 do cow[*,i]=[0.00322,0.,1.0716]
for i=582,50771 do cow[*,i]=[0.,1.782,0.]
```

```
for i=50771,130562 do cow[*,i]=[0.,0.,1.06]
cow=correlate(cow,/covariance)
U=transpose(f)##cow##f
U=(U+transpose(U))/2.

;Eigenvalue decomposition, to calculate a set of basic functions
EW=Eigenql(float(U),EIGENVECTORS=EV,/double)

;projecting the attenutation curves onto the orthogonal basic functions
;calculate dot product
Z=replicate(0.,[pixel,dim[2]]) ;noise-suppressed attenuation curves
B=fltarr([pixel,6])

for i=0,pixel-1 do begin
  B[i,*]=EV##rdata[i,*]
  Z[i,*]=transpose(EV[*,0:2])##EV[*,0:2]##rdata[i,*]
endfor

Z=reform(Z,dim)
B=reform(B,[dim[0],dim[1],6])
rdata=reform(rdata,dim)

time2 =systime(/seconds)
print,'Eigendecomp calculation took ',time2-time1,' seconds'

end
```

K-edge decomposition

IDL algorithm used to calculate the decomposed images corresponding to the photoelectric effect, Compton scattering and gold (section 3.1.4.2).

Listing 6.2: IDL Source Code: K-edge decomposition algorithm

```
;IMAGING SPECTRAL CT
;;using the decomposition of the attenuation, in photo-effect, compton
;scattering and constrast agent (with K-edge)
;based on "K-edge imaging in x-ray computed tomography using multi-bin
;photon counting detectors", E. Roessl and R. Proksa
;Phys. Med. Biol. 52 (2007) 4679-4696

pro Kedge, file,fileneu,dim,meth
;file - name of input files with raw data
;fileneu - name of output files
;dim - [xsize x ysize x bins]
;meth - which method should be used
;       ML - maximum likelihood approac
;       LS - least squares method
;       NB - with constraints
;       Re - applied to reconstructed images

common variKedge, I0,C, d ;global variables
```

```
time1 = systime(/seconds)

  rdata=fltarr(dim)              ;array for sinogramm data
  Photo=fltarr(dim(0),dim(1))    ;array for photo effect
  Compton=fltarr(dim(0),dim(1)) ;array for compton effect
  Gold=fltarr(dim(0),dim(1))     ;array for gold

  ;mean energies
  E=[39.9,54.1,66.5,77.5,83.0,97.1] ;optimized
  ;E=[30.9,43.4,63.2,84.8,98.5,113.0];non-optimized
  ;Mass attenuation of gold
  fAu=[13.070,5.9140,3.4790,2.3650,8.2920,5.5590];optimized
  ;fAu=[25.470,10.490,3.9630,7.8490,5.3600,3.7850];non-optimized

  hilf=1./E^3
  ;Klein Nishina cross section
  en=E/511.
  fKN=(1+en)/en^2*((2*(1+en)/(1+2*en)-alog(1+2*en)/en)) $
         +alog(1+2*en)/(2*en)-(1+3*en)/(1+2*en)^2

  Ct=([[hilf],[fKN],[fAu]])
  C=transpose(Ct)

  case meth of
    'Re': begin
            for i=1,dim[2] do begin
              filename=file+string(i,format='(i1)')+'.img'
              rdata[*,*,i-1]=read_binary(filename, data_type=4, $
                          data_dim=[dim(0),dim(1)])
            endfor
            fileneu=fileneu+'img'
      end
    else: begin
            I0=fltarr(dim[2])
            for i=1,dim[2] do begin
              filename=file+string(i,format='(i1)')+'.fdat'
              rdata[*,*,i-1]=read_binary(filename, data_type=4, $
                  data_dim=[dim(0),dim(1)])
              I0[i-1]=max(rdata[*,*,i-1])
            endfor
            fileneu=fileneu+'fdat'
      end
  endcase

  case meth of
    'ML': begin
            for j=0,dim[1]-1 do begin
              for i=0,dim[0]-1 do begin
                A=[1.d,1.d,1.d]  ;first estimate
                ;Define the starting directional vectors
                Xi=transpose([[1.0d,0.0d,0.0d],[0.0d,1.0d,0.0d], $
                              [0.0d,0.0d,1.d]])
                d=reform(rdata[i,j,*])
```

```
            Powell,A,Xi,0.000001,Fmin,'MLfunc',ITMAX=10000
            Photo[i,j]=A[0]
            Compton[i,j]=A[1]
            Gold[i,j]=A[2]
          endfor
          print,j
        endfor
    end
  'LS': begin
        for i=0,dim[0]-1 do begin ;loop over detector elements
          for j=0,dim[1]-1 do begin ;loop over projections
            d=reform(alog(I0/rdata[i,j,*]))
            A=LA_Linear_equation(Ct##C,Ct##d)
            Photo[i,j]=A[0]
            Compton[i,j]=A[1]
            Gold[i,j]=A[2]
          endfor
          print, i
        endfor
    end
  'NB': begin
        for i=0,dim[0]-1 do begin ;loop over detector elements
          for j=0,dim[1]-1 do begin ;loop over projections
            d=reform(alog(I0/rdata[i,j,*]))
            ;minimization with constraint A>=0
            A=[1.d,1.d,1.d] ;first estimate
            Abnd=[[0,0,0],[1.0e30,1.0e30,1.0e30]]
            ;lower and upper bounds for A
            Gbnd=[[0,0,0,0],[1.0e30,1.0e30,1.0e30,0]]
            ;lower and upper bounds of the contraints
            constrained_min,A,Abnd,Gbnd,3,'NBfunc',inform, $
                    epstop=1.0e-6
            Photo[i,j]=A[0]
            Compton[i,j]=A[1]
            Gold[i,j]=A[2]
          endfor
          print, i
        endfor
    end
  'Re': begin
         for i=0,dim[0]-1 do begin ;loop over x-axis
          for j=0,dim[1]-1 do begin ;loop over y-axis
            d=reform(rdata[i,j,*])
            x=LA_Linear_equation(Ct##C,Ct##d)
            Photo[i,j]=x[0]
            Compton[i,j]=x[1]
            Gold[i,j]=x[2]
          endfor
          print, i
        endfor
    end
  else: print,'method not defined'
endcase
```

```
  openw, 3, 'photo.'+fileneu
  writeu, 3, float(Photo)
  close,3
  openw, 3, 'compt.'+fileneu
  writeu, 3, float(Compton)
  close,3
  openw, 3, 'gold.'+fileneu
  writeu, 3, float(Gold)
  close,3

  time2 =systime(/seconds)
  print,'Kedge calculation took ',time2-time1,' seconds'

end

function MLfunc, A
;maximum likelihood approach
common variKedge
  lambda=I0*exp(-C##A)
  return,total(lambda-d*alog(lambda))
end

function NBfunc, A
;with constraints
common variKedge
  g=dblarr(4)
  g[0]=A[0]
  g[1]=A[1]
  g[2]=A[2]
  g[3]=total((C##A-d)^2)
  return,g
end
```

Least squares parameter estimation

IDL algorithm for the least squares parameter estimation used to calculate the density images of gold, liver and bone (section 3.1.4.3).

Listing 6.3: IDL Source Code: Least squares parameter estimation algorithm

```
pro LSMin, file, dim ,FOD, speichern=sp
;Least squares minimization for reconstructed spectral CT images
;Le 2010 Least squares parameter estimation methods for material
;decomposition with energy discriminating detectors

common vari, rdata, i,j ;global variables

time1 = systime(/seconds)

;read in data
rdata=fltarr(dim)
for i=1, dim[2] do begin
  if (i lt 10) then filename=file+string(i,format='(i1)')+'.img' $
```

```
  else filename=file+string(i,format='(i2)')+'.img'
  rdata[*,*,i-1]=read_binary(filename, data_type=4, $
                 data_dim=[dim[0],dim[1]])
endfor

imgneu=fltarr([dim[0],dim[1],3])
for i=0,dim[0]-1 do begin
  for j=0,dim[1]-1 do begin
    A=[1.d,1.d,1.d] ;first estimate
    Abnd=[[0,0,0],[1.0e30,1.0e30,1.0e30]]
    ;lower and upper bounds for A
    Gbnd=[[0,0,0,0],[1.0e30,1.0e30,1.0e30,0]]
    ;lower and upper bounds for constraints
    constrained_min,A,Abnd,Gbnd,3,'lsfunc',inform,epstop=1.0e-6
    imgneu[i,j,*]=A
  endfor
endfor
print, min(imgneu[*,*,0]),max(imgneu[*,*,0])

if keyword_set(sp) then begin
  openw,3,file+'LSmin.gold.img'
  writeu,3,img[*,*,0]
  close,3
  openw,3,file+'LSmin.bone.img'
  writeu,3,img[*,*,1]
  close,3
  openw,3,file+'LSmin.ST.img'
  writeu,3,img[*,*,2]
  close,3
endif

time2 =systime(/seconds)
print,'LSmin␣calculation␣took␣',time2-time1,'␣seconds'

end

function lsfunc, A  ;function for optimization

common vari

  f=fltarr([6,3])
  ;Bins [25-47-60-75-81-86-120] optimized bins
  f[*,0]=[13.070,5.9140,3.4790,2.3650,8.2920,5.5590] ;fGold
  f[*,1]=[0.6125,0.3479,0.2623,0.2232,0.2100,0.1865] ;fHardBoneMixture
  f[*,2]=[0.2698,0.2162,0.1957,0.1844,0.1800,0.1709] ;fLiver

  ;Bins [25-34-47-60-80-100-120] non-optimized bins
  ;f[*,0]=[21.100,10.740,5.2860,3.3370,7.0390,4.4810] ;fAu
  ;f[*,1]=[0.9313,0.5245,0.3256,0.2573,0.1994,0.1766] ;fHardBoneMixture
  ;f[*,2]=[0.3302,0.2526,0.2112,0.1944,0.1762,0.1664] ;fLiver

  g=dblarr(4)
  g[0]=A[0]
```

```
  g[1]=A[1]
  g[2]=A[2]
  g[3]=total((rdata[i,j,*]-A##f)^2)
  return,g

end
```

Density filter

IDL algorithm for the density filter (section 3.1.4.3).

Listing 6.4: IDL Source Code: Density filter algorithm

```
pro density,file1,file2,dim,speichern=sp
;Based on Kalender 1988 An Algorithm for noise suppression in dual
;energy CT material density images
;file - name of input file
;dim - dimension of image in file [xsize x ysize]

  liver=read_binary(file1+'liver.img',data_type=4,data_dim=dim)
  gold=read_binary(file1+'gold.img',data_type=4,data_dim=dim)
  bone=read_binary(file1+'bone.img',data_type=4,data_dim=dim)
  img=img=read_binary(file2,data_type=4,data_dim=dim)

  ;mass attenuation coefficient at 64.5keV, mean energy of used spectrum
  fliver=0.1983
  fgold=3.761
  fbone=0.2722

  liverneu=liver
  goldneu=gold
  boneneu=bone

  k=3 ;size of mask
  eta=0.05
  for i=k,dim[0]-1-k do begin
    for j=k,dim[1]-1-k do begin
      ;calculate high pass filtered version
      dliver=liver[i,j]-median(liver[i-k:i+k,j-k:j+k])
      dgold=gold[i,j]-median(gold[i-k:i+k,j-k:j+k])
      dbone=bone[i,j]-median(bone[i-k:i+k,j-k:j+k])
      dmu=img[i,j]-median(img[i-k:i+k,j-k:j+k])
      eps=min([1.,abs(dmu/eta)])
      if ((bone[i,j] LE 1.e-8) AND (dliver*dgold LT 0.)) then begin
        C=(fliver*dliver-fgold*dgold)/2.
        liverneu[i,j]=liver[i,j]-(1.-eps^2)*C/fliver
        goldneu[i,j]=gold[i,j]+(1.-eps^2)*C/fgold
      endif else begin
        if ((liver[i,j] LE 1.e-8) AND (dbone*dgold LT 0.)) then begin
          C=(fbone*dbone-fgold*dgold)/2.
          boneneu[i,j]=bone[i,j]-(1.-eps^2)*C/fbone
          goldneu[i,j]=gold[i,j]+(1.-eps^2)*C/fgold
        endif else begin
          if ((gold[i,j] LE 1.e-8) AND (dliver*dbone LT 0.)) then begin
```

```
            C=(fliver*dliver-fbone*dbone)/2.
            liverneu[i,j]=liver[i,j]-(1.-eps^2)*C/fliver
            boneneu[i,j]=bone[i,j]+(1.-eps^2)*C/fbone
          endif
        endelse
      endelse
    endfor
  endfor

  ind=where(goldneu LT 0.)
  goldneu[ind]=0.
  ind=where(liverneu LT 0.)
  liverneu[ind]=0.
  ind=where(boneneu LT 0.)
  boneneu[ind]=0.

  if keyword_set(sp) then begin
    openw,3,file1+'gold.noiseneu.img'
    writeu,3,goldneu
    close,3

    openw,3,file1+'liver.noiseneu.img'
    writeu,3,liverneu
    close,3

    openw,3,file1+'bone.noiseneu.img'
    writeu,3,boneneu
    close,3
  endif

end
```

B. Eigenvector decomposition - Basis images

The eigenvector decomposition also provides the possibility to calculate basis images $B(x) = V^T \mu(E, x)$. The first basis image contains the information due to the maximal variance, the second basis image the information due to the second highest variance and so on. The basis images are not material specific. The basis images for the optimized bin-thresholds are shown in Figure 6.1.

simple voxel phantom

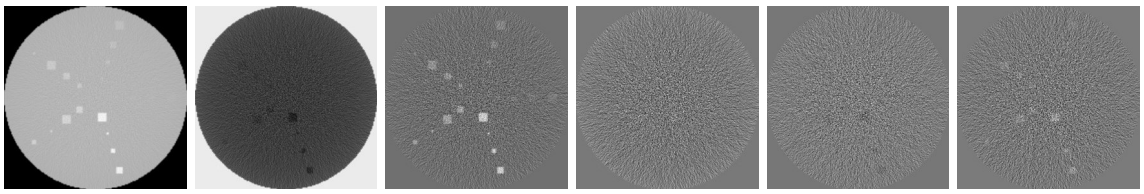

(a) #1 basis image (b) #2 basis image (c) #3 basis image (d) #4 basis image (e) #5 basis image (f) #6 basis image

human voxel phantom with 0.3w% gold

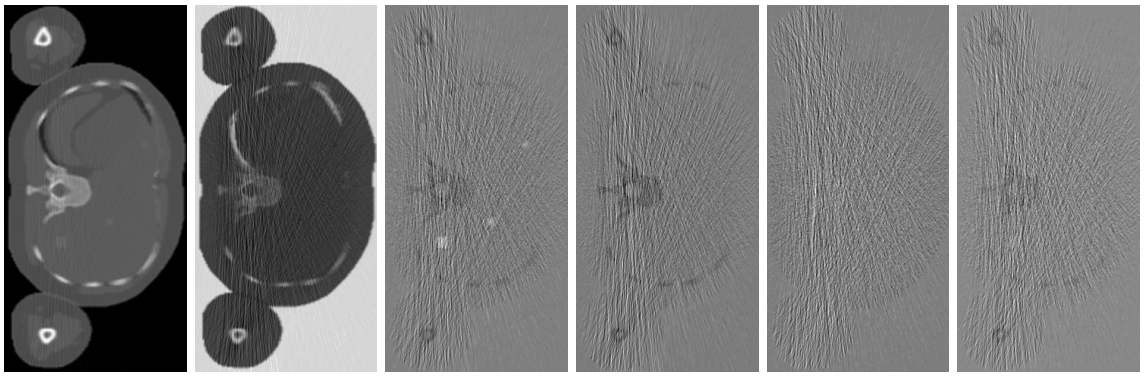

(g) #1 basis image (h) #2 basis image (i) #3 basis image (j) #4 basis image (k) #5 basis image (l) #6 basis image

human voxel phantom with 0.2w% gold

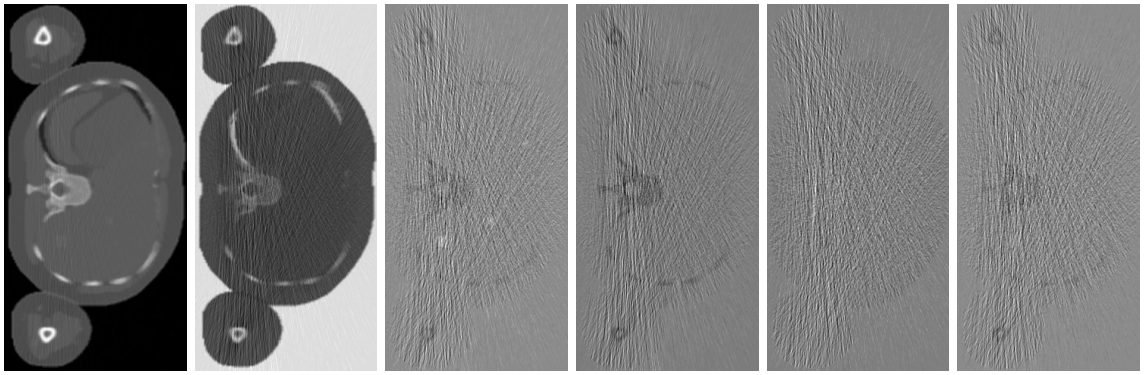

(m) #1 basis image (n) #2 basis image (o) #3 basis image (p) #4 basis image (q) #5 basis image (r) #6 basis image

Figure 6.1: Basis images of the eigenvector decomposition.

The first basis image (Figure 6.1(a), (g) and (m)) is similar to a CT image of a conventional CT detector (i.e. without energy resolution). The noise level is rather low in that image. The basis images are not material specific, however due to the approximation of the covariance matrix, the second basis images (Figure 6.1(b), (h) and (n)) provide information about bone and the third basis (Figure 6.1(c), (i) and (o)) images about gold. For the human voxel phantom the remaining last three basis images (Figure 6.1(j)-(l) and (p)-(r)) hardly provide any information and can therefore be considered as noise. In the last three basis images (Figure 6.1(d)-(f)) of the simple voxel phantom gold is still slightly visible.

C. Further considerations about the K-edge decomposition

The presented results in this section were obtained only for the optimized gold images. As described in section 3.1.4.2 a maximum likelihood approach is used to determine the unknown coefficients A_k. It is also possible to use the least squares method instead. Equation 3.25b can be reformulated as a linear equation system

$$CA = d, \qquad C \in \mathbb{R}^{K\times 3}, \qquad d \in \mathbb{R}^K \text{ and } A \in \mathbb{R}^3 \tag{6.1}$$

with $C = [1/E^3, f_{KN}(E/E_e), f_{\text{highZ}(E)}]$, $d = \ln(I_0/I(A))$ and $A = [A_{\text{photo}}, A_{\text{Compton}}, A_{\text{highZ}}]$. The error function is given by

$$CA - d = r \qquad r \in \mathbb{R}^K \tag{6.2}$$

The sum of the squares of the residuals r needs to be minimized and can be formulated as a linear equation system

$$C^T CA = C^T d \tag{6.3}$$

This linear equation system can be solved for A. For the least squares method it is assumed that errors are normally distributed. The results with the least squares method are shown in Figure 6.2 (results are only shown for the optimized bin thresholds).
As already mentioned in section 4.1.4.2 the results of the maximum likelihood approach for A_{highZ} and A_{photo} are negative for some raw data values. To prevent this equation 6.2 can be minimized under the constraint $A_k \geq 0$. The resulting decomposed images are presented in Figure 6.3.
The K-edge decomposition approach can also be applied to the reconstructed images of all bins. Each pixel in the reconstructed images contains the linear attenuation coefficient $\mu(E)$, which can be calculated according to Equation 3.21.

$$\mu(E,x) = \widetilde{C}_{\text{photo}}(x)\frac{1}{E^3} + \widetilde{C}_{\text{Compton}}(x) f_{\text{KN}}\left(\frac{E}{E_e}\right) + \widetilde{w}_{\text{highZ}}(x)\left(\frac{\mu(E)}{\rho}\right)_{\text{highZ}}$$

Transforming this equation into a linear equation system yields

$$CA = g \qquad C \in \mathbb{R}^{K\times 3}, \qquad g \in \mathbb{R}^K \text{ and } A \in \mathbb{R}^3 \tag{6.4}$$

with $C = [1/E^3, f_{KN}(E/E_e), f_{\text{highZ}(E)}]$ and $g_i = \mu_i$ $(i = 1, ..., K)$. We can now solve this problem with the least squares fitting method, leading to the linear equation system $C^T CA = C^T g$. The results are demonstrated in Figure 6.4. The maximum likelihood approach with the assumption of independent Poisson random variables cannot be applied to the images since the linear attenuation coefficients do not form a discrete distribution. The evaluation of the SNR, CNR and the contrast is summarized in Table 6.1 and 6.2. The comparison of the implemented and calculated concentration of gold is shown in Table 6.3. The highest SNR is achieved when the K-edge decomposition is applied to the reconstructed images, the SNR is significiantly higher than for the maximum-likelihood approach in section 4.1.4.2. The SNR for the K-edge decomposition with a least squares approach is comparable to the K-edge decomposition with a maximum-likelihood approach. The smallest SNR is achieved by the K-edge decomposition approach with constraints. The CNR and the contrast of all three K-edge decomposition approaches are smaller than for the K-edge decomposition with the maximum-likelihood approach, however the results are not significant.

simple voxel phantom

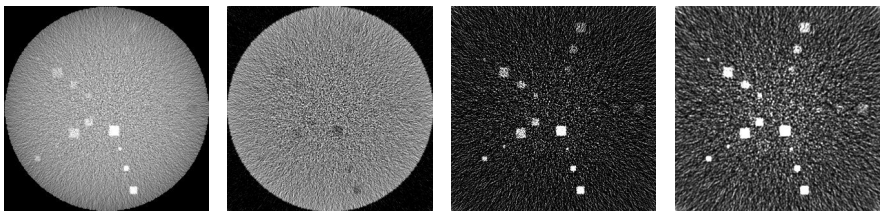

(a) Compton Effect (b) Photo Effect (c) Gold (d) Gold after bilateral filtering

human voxel phantom with 0.3w% gold

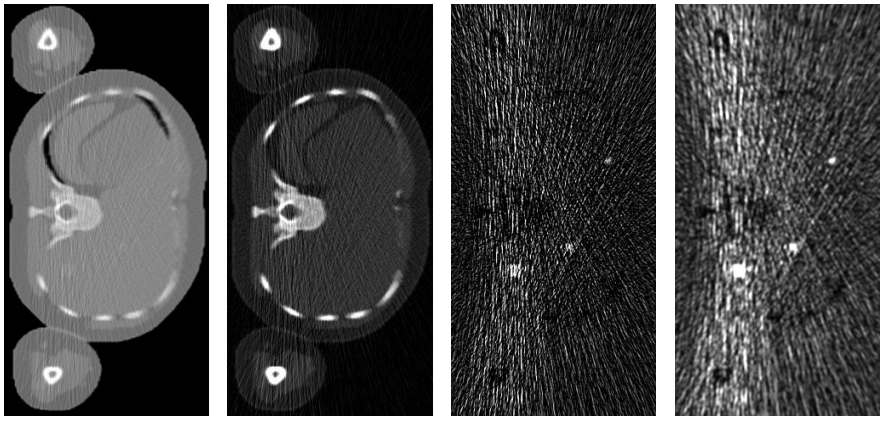

(e) Compton Effect (f) Photo Effect (g) Gold (h) Gold after bilateral filtering

human voxel phantom with 0.2w% gold

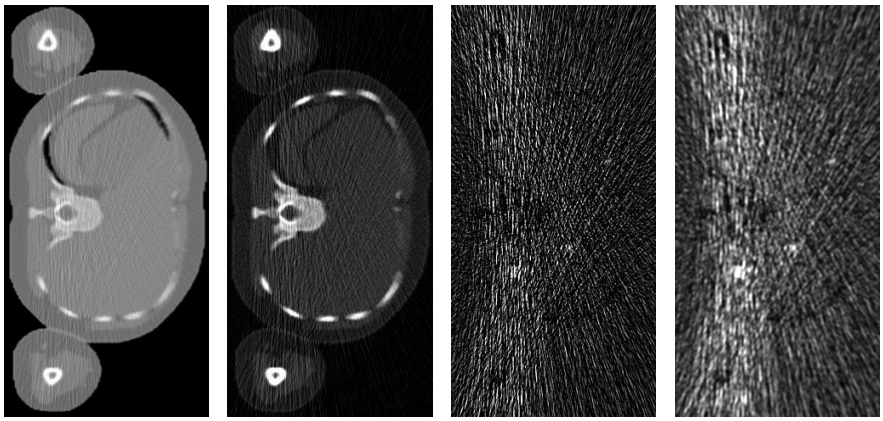

(i) Compton Effect (j) Photo Effect (k) Gold (l) Gold after bilateral filtering

Figure 6.2: Results of the K-edge decomposition algorithm with a least squares approach (corresponding images of the human voxel phantom are equally scaled and windowed).

simple voxel phantom

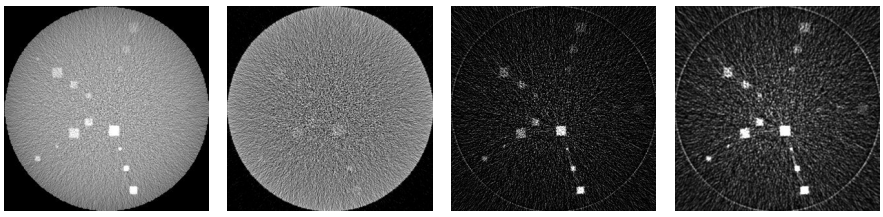

(a) Compton Effect (b) Photo Effect (c) Gold (d) Gold after bilateral filtering

human voxel phantom with 0.3w% gold

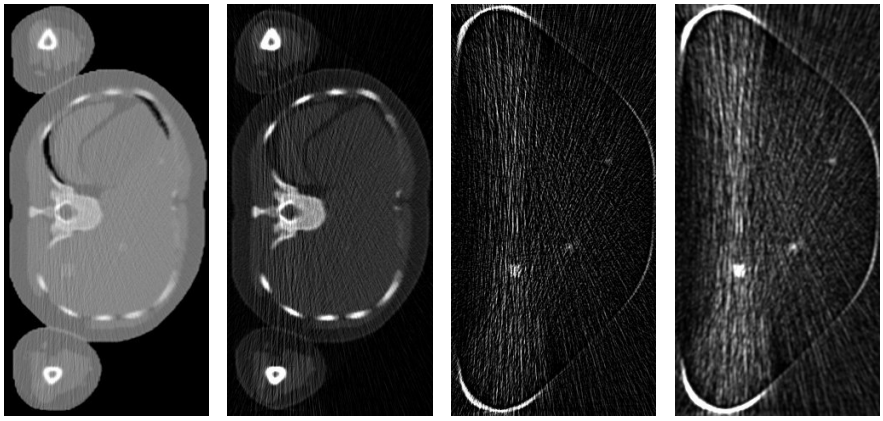

(e) Compton Effect (f) Photo Effect (g) Gold (h) Gold after bilateral filtering

human voxel phantom with 0.2w% gold

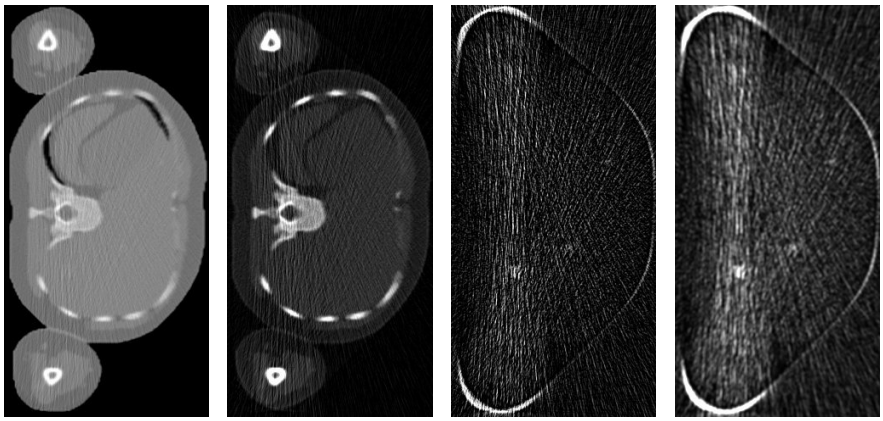

(i) Compton Effect (j) Photo Effect (k) Gold (l) Gold after bilateral filtering

Figure 6.3: Results of the K-edge decomposition algorithm with constraints (corresponding images of the human voxel phantom are equally scaled and windowed).

simple voxel phantom

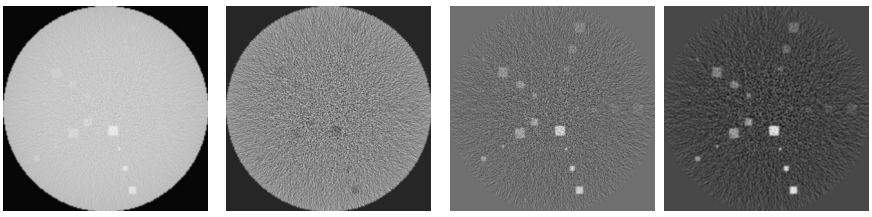

(a) Compton Effect (b) Photo Effect (c) Gold (d) Gold after bilateral filtering

human voxel phantom with 0.3w% gold

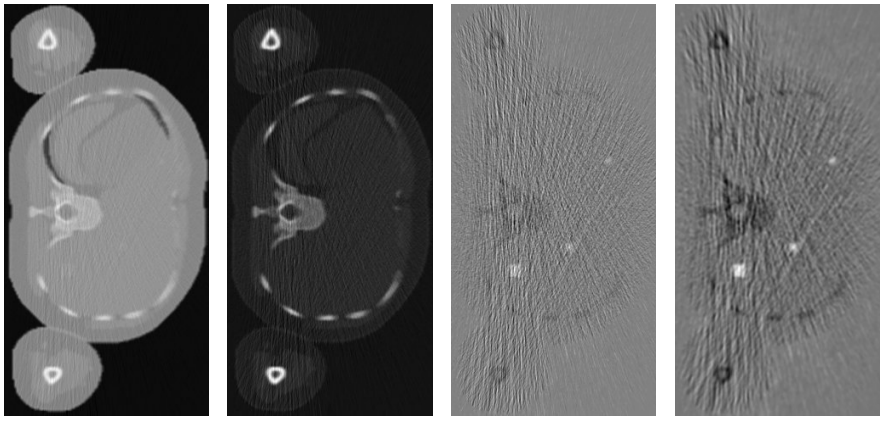

(e) Compton Effect (f) Photo Effect (g) Gold (h) Gold after bilateral filtering

human voxel phantom with 0.2w% gold

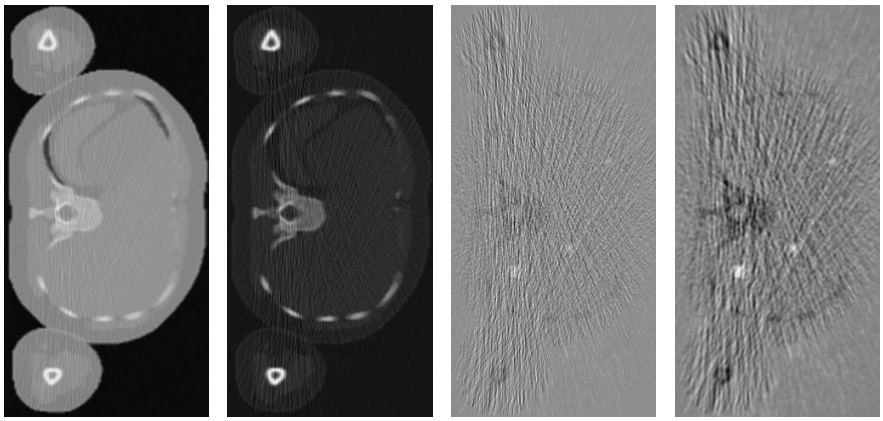

(i) Compton Effect (j) Photo Effect (k) Gold (l) Gold after bilateral filtering

Figure 6.4: Results of the K-edge decomposition algorithm applied to the reconstructed images (corresponding images of the human voxel phantom are equally scaled and windowed).

Table 6.1: Performance results of the K-edge decomposition algorithm for the different approaches for the simple voxel phantom.

		least squares approach			with constraints			applied to the reconstructed images		
		SNR	CNR	C	SNR	CNR	C	SNR	CNR	C
0.7w% gold	unfiltered	3.21±1.0	2.61±1.02	0.810±0.32	2.70±1.0	2.21±0.97	0.780±0.35	7.43±1.0	2.51±1.03	0.284±0.12
	filtered	5.26±1.0	4.47±0.99	0.810±0.18	4.53±1.0	3.85±0.98	0.782±0.20	8.29±1.0	4.44±0.97	0.466±0.10
0.4w% gold	unfiltered	2.37±1.0	1.75±0.91	0.712±0.37	2.19±1.0	1.51±0.87	0.648±0.37	7.98±1.0	1.74±0.89	0.184±0.094
	filtered	4.96±1.0	3.79±0.97	0.708±0.18	4.88±1.0	3.33±0.92	0.644±0.18	10.1±1.0	3.87±0.87	0.326±0.073
0.3w% gold	unfiltered	1.82±1.0	1.22±0.84	0.627±0.43	1.65±1.0	0.99±0.80	0.530±0.43	7.61±1.0	1.29±0.88	0.141±0.096
	filtered	3.98±1.0	2.73±0.94	0.634±0.22	3.44±1.0	2.15±0.96	0.539±0.24	9.52±1.0	2.98±0.99	0.269±0.090
0.2w% gold	unfiltered	1.53±1.0	0.884±0.80	0.521±0.47	1.36±1.0	0.775±0.80	0.491±0.51	7.97±1.0	0.978±0.81	0.0952±0.080
	filtered	3.52±1.0	1.96±0.91	0.521±0.24	3.11±1.0	1.74±0.91	0.494±0.26	10.1±1.0	2.14±0.94	0.185±0.082
0.1w% gold	unfiltered	1.16±1.0	0.390±0.68	0.283±0.49	1.19±1.0	0.376±0.64	0.265±0.45	8.06±1.0	0.478±0.64	0.0471±0.063
	filtered	2.99±1.0	0.922±0.71	0.291±0.22	3.69±1.0	1.01±0.64	0.278±0.18	10.2±1.0	1.11±0.73	0.0991±0.065

Table 6.2: Performance results of the K-edge decomposition algorithm for the different approaches for the human voxel phantom.

		least squares approach			with constraints			applied to the reconstructed images		
		SNR	CNR	C	SNR	CNR	C	SNR	CNR	C
0.3w% gold	unfiltered	1.87±1.0	1.15±0.86	0.589±0.44	1.96±1.0	1.11±0.80	0.540±0.39	7.25±1.0	1.19±0.78	0.152±0.097
	filtered	5.80±1.0	3.43±0.81	0.591±0.14	6.22±1.0	3.04±0.68	0.537±0.12	12.2±1.0	3.62±0.83	0.316±0.073
0.2w% gold	unfiltered	1.53±1.0	0.727±0.74	0.438±0.45	1.70±1.0	0.724±0.70	0.390±0.37	6.89±1.0	0.771±0.67	0.102±0.088
	filtered	4.58±1.0	2.16±0.88	0.441±0.18	5.04±1.0	2.15±0.76	0.397±0.14	9.22±1.0	2.41±0.85	0.250±0.090

Table 6.3: Implemented gold concentration and calculated weight fraction of gold multiplied by the total density for the K-edge decomposition for the different approaches. The bilateral filter is used to filter the decomposed gold images, refereed to as bifilt.

	simple voxel phantom				
implemented	0.7w%	0.4w%	0.3w%	0.2w%	0.1w%
least squares approach	0.48±0.15	0.27±0.11	0.19±0.10	0.14±0.09	0.08±0.07
least squares approach+bifilt	0.47±0.09	0.26±0.05	0.19±0.05	0.13±0.04	0.08±0.03
with constraints	0.30±0.11	0.16±0.07	0.11±0.06	0.07±0.05	0.04±0.04
with constraints+bifilt	0.29±0.06	0.15±0.03	0.10±0.03	0.07±0.02	0.04±0.01
reconstructed images	0.48±0.15	0.27±0.11	0.19±0.11	0.13±0.10	0.06±0.09
reconstructed images+bifilt	0.47±0.09	0.26±0.05	0.18±0.05	0.13±0.04	0.04±0.03

	human voxel phantom	
implemented	0.3w%	0.2w%
least squares approach	0.21±0.12	0.16±0.11
least squares approach+bifilt	0.20±0.04	0.15±0.03
with constraints	0.13±0.07	0.11±0.07
with constraints+bifilt	0.12±0.02	0.11±0.02
reconstructed images	0.20±0.13	0.14±0.13
reconstructed images+bifilt	0.19±0.04	0.12±0.04

D. Further considerations about the eigenvector decomposition and the least squares parameter estimation

As already described in section 4.1.4.1 and 4.1.4.3 the estimated gold concentration in the gold images is too low. In order to investigate the performance of the algorithms the exact linear attenuation coefficients in each energy bin (optimized bin thresholds) for hard bone mixture, liver tissue, 0.7w%, 0.4w%, 0.3w%, 0.2w% and 0.1w% gold (values in Table 3.2 multiplied by the density defined in Table 3.1) were used as input for the eigenvector decomposition and the least squares parameter estimation.
For the eigenvector decomposition the covariance matrix $\mathrm{Cov}(\rho_{\mathrm{total}}(x)w(x))$ was estimated with

$$\overbrace{\qquad\qquad}^{n_1}\overbrace{\qquad\qquad}^{n_2}\overbrace{\qquad\qquad}^{n_3} \tag{6.5}$$

$$= \mathrm{Cov}\begin{pmatrix} & 0.0032 & & & 0.0 & & & 0.0 & \\ \cdots & 0.0 & \cdots & \cdots & 1.782 & \cdots & \cdots & 0.0 & \cdots \\ & 1.0716 & & & 0.0 & & & 1.06 & \end{pmatrix} \tag{6.6}$$

$$= \begin{pmatrix} 2.31 \times 10^{-6} & -6.37 \times 10^{-4} & 3.87 \times 10^{-4} \\ -6.37 \times 10^{-4} & 0.71 & -0.42 \\ 3.87 \times 10^{-4} & -0.42 & 0.25 \end{pmatrix} = \mathrm{Cov}(\rho_{\mathrm{total}}(x)w(x)) \tag{6.7}$$

The number of pixels containing gold, bone and liver tissue are equal and $n_1 = n_2 = n_3 = 12500$.
For the first evaluation no noise was added and for the second evaluation noise was added to the input data. The setup of the input data is shown in Figure 6.5. The noise level was chosen such that the SNR in the input data is comparable to the SNR in the simulation results.

Figure 6.5: Setup of the input data for the analysis of the eigenvector decomposition and the least squares parameter estimation.

The results of the eigenvector decomposition and the least squares parameter estimation are shown in Figure 6.6.

eigenvector decomposition

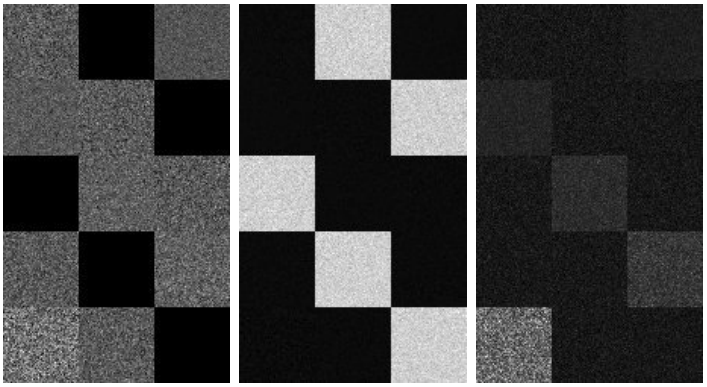

(a) Liver (b) Bone (c) Gold

least squares parameter estimation without density filter

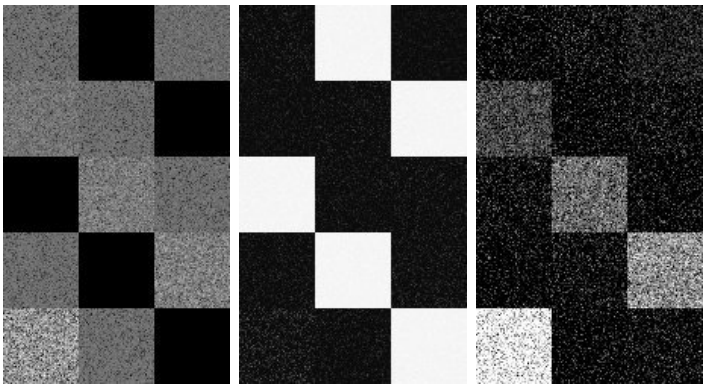

(d) Liver (e) Bone (f) Gold

least squares parameter estimation with density filter

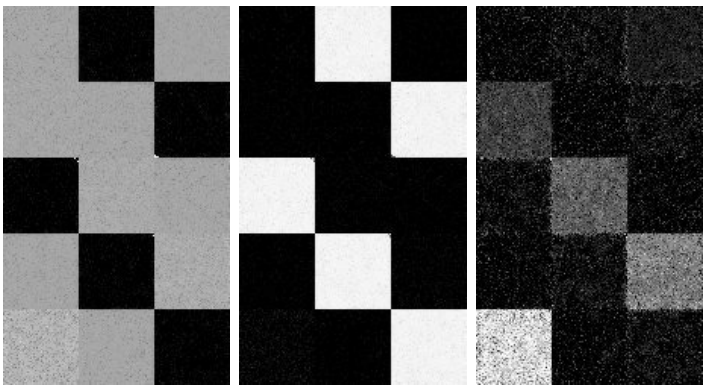

(g) Liver after density filtering (h) Bone after density filtering (i) Gold after density filtering

Figure 6.6: Results of the eigenvector decomposition and the least squares parameter estimation of the input data with noise.

The implemented and calculated gold concentrations are summarized in Table 6.4. For the input data without noise the calculated concentrations exactly match the implemented concentrations. The eigenvector decomposition estimates the gold concentration almost exactly even for the input data with noise. The least squares parameter estimation underestimates the gold concentration for the input data with noise. However the difference between the calculated and the implemented concentrations is smaller than for the simulations.

Table 6.4: Implemented and calculated concentrations of gold in w%.

implemented	0.7w%	0.4w%	0.3w%	0.2w%	0.1w%
	input data without noise				
EV	0.70±0.00	0.40±0.00	0.30±0.00	0.20±0.00	0.10±0.00
LSPE	0.70±0.00	0.40±0.00	0.30±0.00	0.20±0.00	0.10±0.00
	input data with noise				
EV	0.69±0.23	0.40±0.14	0.30±0.12	0.20±0.11	0.10±0.10
LSPE	0.62±0.23	0.35±0.15	0.26±0.13	0.17±0.10	0.08±0.08
LSPE+density	0.67±0.19	0.39±0.12	0.29±0.09	0.19±0.08	0.09±0.06

E. Materials

Substances and chemicals

- Gold Colloid: 50 nm, BBI Solutions (Cardiff, UK)
- Gold Colloid: 15 nm, BBI Solutions (Cardiff, UK)
- 4T1 cells, ATCC® Number: CRL-2539™
- monoclonal antibody cmHsp70.1 (concentration 2.4 µg/µl), Multimmune GmbH (Munich, Germany)
- EM Goat anti-Mouse IgG: 30 nm (protein concentration 11.4 µg/ml), BBI Solutions (Cardiff, UK)
- Hsp70 protein, SignalChem (Richmond, Canada)
- Hsc70 protein, Enzo Life Science (Loerrach, Germany)
- RPMI 1640 Medium, Gibco (Carlsbad, USA)
- Foetal calf serum (FCS), PAA (Pasching, Austria)
- L-Glutamine, PAN (Aidenbach, Germany)
- Penicillin/Streptomycin, Gibco (Carlsbad, USA)
- Sodium/Natrium-Pyruvate, PAN (Aidenbach, Germany)
- Phosphate buffered saline (PBS), Lonza (Cologne, Germany)
- Trypsin-EDTA 0.25%, Gibco (Carlsbad, USA)
- Albumin Fraction V, IgG and protease free (BSA), Carl Roth (Karlsruhe, Germany)
- Dimethyl sulfoxide (DMSO), Sigma Aldrich (St. Louis, USA)
- Trypan blue stain, Cambrex Bio Science (Walkerville, USA)
- May-Gruenwald's solution, Carl Roth (Karlsruhe, Germany)
- 2.5% Glutaraldehyde in 0.1M soidum cacodylate, Buffer pH 7.4, Electron Microscopy Sciences (Hatfield, USA)
- Sodium hydroxide (NaOH)
- Hydrogen chloride (HCl)
- Methanol
- Sodium chloride (NaCl)
- Millipore water

Consumables

- Cryo.s tubes, Greiner Bio-One (Frickenhausen, Germany)
- 1.5 ml micro-centrifuge tubes, Eppendorf (Hamburg, Germany)
- Cell culture flasks, BD Falcon (California, USA)
- 6 well plates, Greiner Bio-One (Frickenhausen, Germany)
- Pipetting tips, Eppendorf (Hamburg, Germany)
- Counting chamber Fast Read 102, Immune Systems Ltd.
- Serological pipettes, Greiner Bio-One (Frickenhausen, Germany)
- Tubes, BD Falcon (California, USA)
- pH-indicator strips, pH 6.5-10.0, Merck (Darmstadt, Germany)
- Filter, Minisart, 0.2 µm, Sartorius AG (Göttingen, Germany)
- Western Blot Membrane, Hybond PVDF, GE lifescience
- Syringe, B. Braun Melsungen AG (Melsungen, Germany)
- Microscope slides standard, Carl Roth (Karlsruhe, Germany)
- Petri dishes, Carl Roth (Karlsruhe, Germany)
- Beem Embedding capsules, Electron Microscopy Sciences (Hatfield, USA)
- Silica glass tubes

Instruments

- Laminar flow hood, Schulz-Lufttechnik GmbH (Sprockhövel, Germany)
- Hettich Universal 32R Centrifuge (Tuttlingen, Germany)
- Heraeus Incubator, Thermo Scientific (Waltham, USA)
- Axioplan2 imaging Microscope, Zeiss (Jena, Germany)
- Axiocam HRc, Zeiss (Jena, Germany)
- Cary 1 UV-Vis spectrometer, Varian (Palo Alto, USA)

Eidesstattliche Versicherung

Müllner, Marie Annett

Name, Vorname

Ich erkläre hiermit an Eides statt,

dass ich die vorliegende Dissertation mit dem Thema

Optimization and implementation of gold-nanoparticles for medical imaging

selbständig verfasst, mich außer der angegebenen keiner weiteren Hilfsmittel bedient und alle Erkenntnisse, die aus dem Schrifttum ganz oder annähernd übernommen sind, als solche kenntlich gemacht und nach ihrer Herkunft unter Bezeichnung der Fundstelle einzeln nachgewiesen habe.

Ich erkläre des Weiteren, dass die hier vorgelegte Dissertation nicht in gleicher oder in ähnlicher Form bei einer anderen Stelle zur Erlangung eines akademischen Grades eingereicht wurde.

Ort, Datum

Unterschrift Doktorandin/Doktorand